NANOPARTICLE INTERACTIONS WITH MUCOSAL BARRIERS

Dissertation

zur Erlangung des Grades

des Doktors der Naturwissenschaften

der Naturwissenschaftlich-Technischen Fakultät

der Universität des Saarlandes

von

Enkeleda Meziu

Saarbrücken

2025

Tag des Kolloquiums:	11.06.2025
Dekan:	Prof. Dr.-Ing. Dirk Bähre
Berichterstatter:	Prof. Dr. Marc Schneider
	PD Dr. Annette Kraegeloh
	Prof. Dr. Alexandra K. Kiemer
Vorsitz:	Prof. Dr. Andriy Luzhetskyy
Akad. Mitarbeiter:	Dr. Brigitta Loretz

Table of contents

I. Summary

Human pulmonary mucus represents a tenacious barrier for pulmonary drug administration. The design of an efficient inhalation therapy demands a detailed understanding of the mucus layer and well characterized mucus models for the investigation of the behavior of therapeutics in mucus. The developed strategies used to circumvent the mucus barrier should be evaluated in terms of efficacy and safety.

The application of various microscopy techniques provided new insights revealing a non-porous, heterogenous and composite structure of mucus. Calu-3 *in vitro* mucus was characterized regarding mucins as macromolecules, small metabolites, biophysical properties and compared to human pulmonary *ex vivo* mucus providing valuable input in terms of the interpretation of data obtained using these models. Calu-3 *in vitro* mucus was employed for the investigation of the impact of mucus modulation, as a mucus penetration enhancing strategy on the protective function of mucus. Cytotoxicity assessment of the impact of probing model particles revealed that modulation led to a reduced protective function of mucus emphasizing the importance of safety assessment of therapy protocols involving mucus modulation.

II. Kurzzusammenfassung

Der menschliche pulmonale Mukus stellt eine Barriere für die Verabreichung von Medikamenten in die Lunge dar. Die Entwicklung einer effizienten Inhalationstherapie erfordert ein detailliertes Verständnis der Mukusschicht und gut charakterisierte Mukusmodelle zur Untersuchung des Verhaltens von Therapeutika im Mukus. Die entwickelten Strategien zur Umgehung der Mukusbarriere sollten im Hinblick auf ihre Wirksamkeit und Sicherheit bewertet werden.

Die Mukus-Struktur wurde mittels verschiedener Mikroskopietechniken untersucht. Die Ergebnisse zeigten eine nicht poröse, heterogene Komposit-Struktur des Mukus. Calu-3 *in vitro* Mukus wurde in Bezug auf Muzine als Makromoleküle, kleine Metabolite und biophysikalische Eigenschaften charakterisiert und mit menschlichem pulmonalem *ex vivo* Mukus verglichen. Diese Untersuchung lieferte wertvolle Erkenntnisse für die Interpretation der mit diesen Modellen gewonnenen Daten. Calu-3 *in vitro* Mukus wurde verwendet, um den Einfluss der Mukusmodulation als Strategie zur Verbesserung der Mukuspenetration auf die Schutzfunktion des Mukus zu untersuchen. Die Zytotoxizitätsanalyse der Auswirkung von Modellpartikeln ergab, dass die Modulation zu einer verringerten Schutzfunktion des Mukus führte. Diese Ergebnisse betonen die Bedeutung von Sicherheitsuntersuchungen bei der Entwicklung der Therapieprotokolle, die eine Modulation des Mukus umfassen.

III. List of abbreviations

PTS	proline, threonine and serine
CFTR	cystic fibrosis transmembrane conductance regulator
ASL	air surface liquid
CLSM	confocal laser scanning microscopy
CF	cystic fibrosis
ETT	endotracheal tube
HBE	human bronchial epithelium
LCC	liquid-covered culture
AIC	air-interfaced culture
MSD	mean square displacement
Cryo-SEM	cryo-scanning electron microscopy
ESEM	environmental scanning electron microscopy
STED	stimulated emission depletion
CLSM	confocal laser scanning microscopy
SEM	scanning electron microscopy
WGA	wheat germ agglutinin
RT	room temperature
DABCO	(1,4-Diazabicyclo(2,2,2)octan)
APD	avalanche photo diode
PSF	point spread function
DPBS	Dulbecco`s phosphate buffered saline
PFA	paraformaldehyde
HILIC	hydrophilic interaction chromatography
PCA	principal component analysis
LDA	linear discriminant analysis
NAC	N-acetylcysteine
NH_2-PS-NPs	amine-modified polystyrene nanoparticles
COOH-PS-Ps	carboxyl-modified polystyrene particles
COOH-PS-NPs	carboxyl-modified polystyrene nanoparticles
TEER	transepithelial electrical resistance
HMDS	hexamethyldisilazane
WGA-Rhod	wheat germ agglutinin-tetramethyl Rhodamine
LDH	lactate dehydrogenase

1. Introduction

This chapter has already been published in German in the following article:

E. Meziu.; A. Kraegeloh.; M. Schneider; *Mukus und* M*ukusmodelle: eine Übersicht. Pharmakon, Volume 10, Number 1, January 2022, pp. 53-58(6)*

1.1. Physicochemical properties of pulmonary mucus barrier

Mucus consists of water (95% w/w), mucin glycoproteins (2-5% w/v), non-mucin proteins, lipids, DNA, cells, and cellular debris [1,2]. The primary structural constituent of mucus are mucins (0.5-20 MDa), that consist of a protein backbone with proline, threonine and serine (PTS) repeated domains and oligosaccharide side chains [3]. Mucin glycoprotein terminals have non-glycosylated cysteine rich domains, which have a key role in mucin polymerization, and give mucus its viscoelastic traits (Figure 1.1) [4]. Among 21 human airway mucins, MUC5B and MUC5AC are the major gel-forming mucins [5].

Mucins interact physically and chemically with each other and other mucus constituents to create a three-dimensional polymer entanglement with microscopic domains filled with low viscosity fluid [6]. It has been assumed that these low viscosity domains might serve as a transport pathway for molecules and particles [7–9]. Therefore, their characterization regarding frequency and size scale has extensively been performed. At this point scanning electron microscopy and tracking of the movement of tracer particles by video microscopy are the primarily utilized techniques [8,10–12]. Electron microscopy studies (that involve sample preparation steps like freezing and dehydration) have shown a porous architecture of mucus. However, in its hydrated state (analyzed by super-resolution stimulated emission depletion microscopy), mucus rather showed a compact structure characterized by voids filled with other mucus constituents, as well as few of non-labeled voids [13]. At the macroscale level (macrorheology), mucus shows a non-Newtonian (shear thinning viscosity) behavior, while at the nanoscale level considering the abovementioned low viscosity domains (microrheology) it can behave as a low viscosity fluid [10,14]. Mucins

confer mucus its flow (viscosity, measured by loss modulus G") and deformation (elasticity, measured by storage modulus G`) properties. At physiologically relevant shear/stress levels, mucus shows an elastic dominant behavior G`> G" (~ 2000 times more viscous than water) [6,15].

Given its high interaction potential (interaction barrier), unique architecture, viscoelastic properties (size exclusion barrier), and dynamic nature (mucociliary clearance) mucus hydrogel plays an important barrier role by restricting molecule diffusion and providing strong interaction with inhaled objects [16,17].

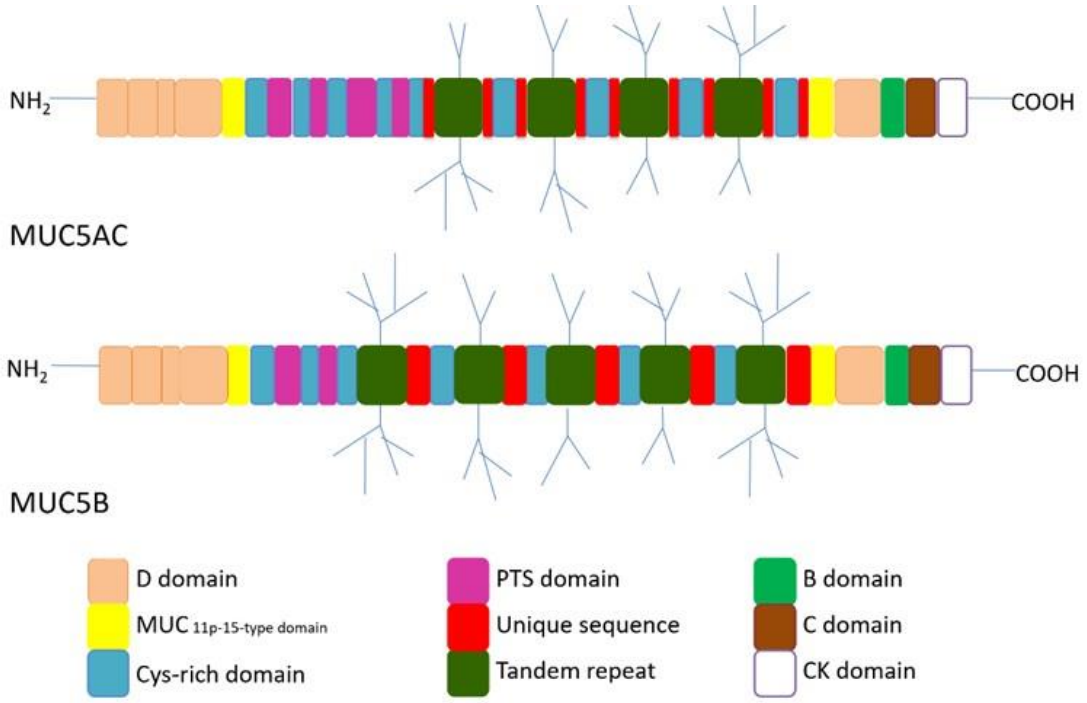

Figure 1.1: Illustration of the mucin MUC5AC and mucin MUC5B glycoproteins. PTS indicates proline/threonine/serine. The figure has been reproduced with permission from [18].

1.2. Altered physicochemical characteristics of mucus in diseases

Physicochemical properties of mucus are altered in mucin-associated diseases. For example, in cystic fibrosis (CF), defected cystic fibrosis transmembrane conductance regulator (CFTR) causes an impaired secretion of chloride ions and consequently the hyperabsorption of sodium ions. Dysregulated salt transport leads to hyperabsorption of

water, dehydration of mucus layer, and an increase of mucus viscosity (Figure 1.2).

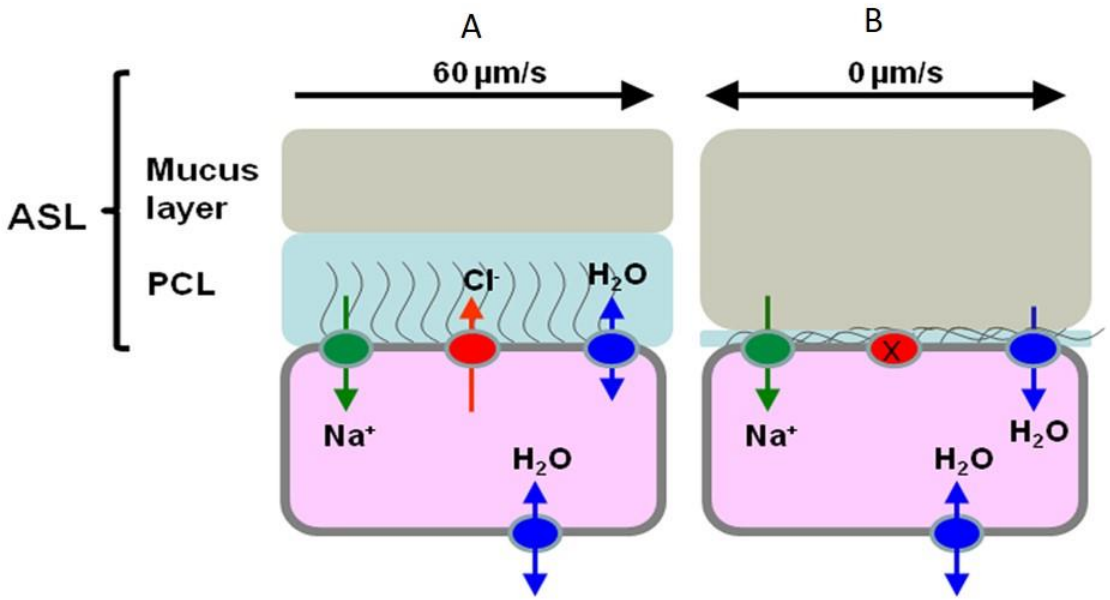

Figure 1.2: Illustration of salt and water transport and structure of air surface liquid (ASL) in A) healthy and B) cystic fibrosis airway epithelium. In healthy epithelium CFTR (red circle) ensures the adequate hydration of ASL. The ASL is made up of the mucus layer and the so-called periciliary layer. In cystic fibrosis disease, water homeostasis is disturbed because the defective CFTR no longer adequately transports the Cl^- ions. This results in an increased Na^+ uptake by ENaC (green circle). The dehydrated ASL, with a lower total volume than in the healthy state, leads to an impaired and reduced mucociliary clearance, which is reflected in the decreased clearance rates. The figure has been adapted from [19].

All these cause a thick and tenacious CF mucus, that impairs mucociliary clearance and leads to chronic bacterial infections. In contrast to healthy mucus (predominated by gel-forming mucins), in CF sputum, bacterial infections cause an inflammatory cell necrosis related predominance of the polymeric DNA and F-actin (Figure 1.3) [9,20,21].

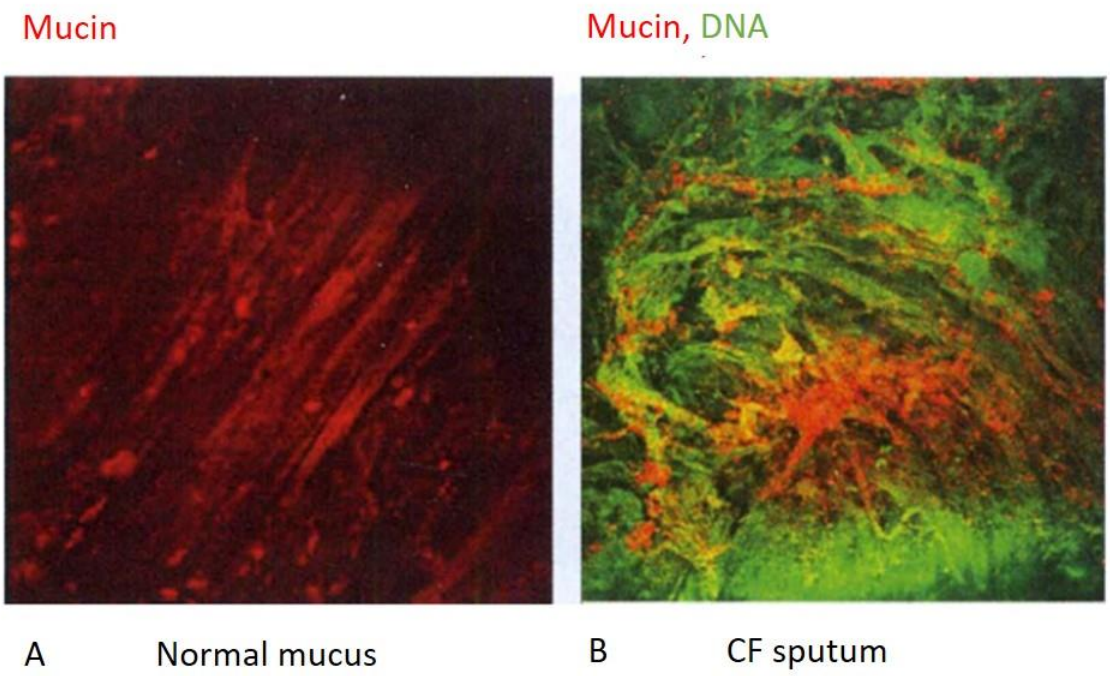

Figure 1.3: Confocal laser scanning (CLSM) images of normal mucus (A), and cystic fibrosis sputum (B). Mucin was stained with UEA lectin conjugated Texas red phalloidin (red) and DNA was stained with YOYO-I (green). In normal mucus linear mucin polymers are seen, while CF sputum reveals less mucin polymers and long linear bundles of DNA. The size of the figures is 200 x 200 µm. The figure has been adapted with permission from [22].

1.3. Mucus models to evaluate the efficacy and safety of nanotherapeutics

Healthy and diseased mucus represent a challenging hurdle for transmucosal drug carriers. Thus, the investigation of the role of mucus on drug carrier diffusion through mucus is crucial for a successful drug delivery development. Therefore, various *in vitro*, *ex vivo*, and *in vivo* models have been developed. The ultimate aim of all these models is to recapitulate human mucus [23].

Isolated *ex vivo* mucus can be collected by tissues of various sites and origins (gastric pig mucus [24], human cervical mucus [25], human and horse tracheal mucus [26,27]) by using different protocols. For example, human tracheal mucus is collected by using endotracheal tube (ETT) method [12,13,28,29]. The distal part of the endotracheal tubes of patients undergoing surgery (general anesthesia) are cut and centrifuged to obtain small amounts of tracheal mucus [29]. In contrast to highly complex *in vivo* systems, where it is difficult to distinguish between the impact of mucus and other constituents of the system, isolated

tracheal mucus allows for a more precise evaluation of the exclusive role of mucus on drug delivery. Limited accessibility, and inter-individual variability are some of the drawbacks of this model [30]. A recent study has reported that due to dehydration occurring during intubation, ETT mucus is a model more relevant for muco-obstructive lung diseases rather than for healthy mucus [26]. Due to its high microbial susceptibility, another concern regarding this model is the impact of storage conditions (typically -20 °C or -80 °C) on the physicochemical properties of mucus [28,31]. The data regarding this point are controversial. For example, while Duncan et al., (2016) showed a significant increase of nanoparticle diffusion in previously frozen samples [7], other studies have reported that freezing does not have an influence on the viscoelastic properties of mucus as well as drug diffusion [32,33].

Induced normal sputum is another isolated mucus model. For collecting these samples volunteers are exposed to hypertonic saline solution (3%, 4%, 5% until able to produce sputum) [34]. An advantage of this model is that samples are not prone to dehydration during collection. However, due to its complicated collection procedures, these samples are not easily accessible and need trained personnel and medical supervision.

Purified mucins derived from porcine stomach or bovine submaxillary gland are reconstituted to prepare artificial mucus surrogates [24,30,35]. Such mucins are typically reconstituted in mediums, which mimic mucus regarding biochemical composition [35]. Contrary to the complex undefined and highly variable composition of *in vivo* models or human originated mucus samples, simple reconstituted purified mucin solutions allow a clearer evaluation of the mucin nanoparticle interactions. However, the pitfall of this models is that these mucins do not form disulfide bonds creating the typical mucus structure with elastic dominant properties. These models lead to an overestimation of the efficacy of drug carriers for mucus penetration [36]. The addition of cross-linking agents has been used as a strategy to overcome this limitation [35,37,38]. Frisch et al., (2021) has recently reported the suitability of such a mucus surrogate for the investigation of antibiotic permeation and efficacy [39].

For an improved physiological relevance, systems like mucus producing cell culture models have also been established. It has been reported that the rheological properties of mucus differ with the proximity to the epithelium, varying from an elastic behavior near to the cell layer to a more viscous behavior at the distant mucus layers [40]. Given this, mucus

incorporating cell culture models represent a physiologically more relevant model as compared to isolated mucus models that consider mucus as an isotropic system [23]. In addition, cell culture models allow the evaluation of the impact of drugs and drug carriers on the monolayer integrity as well as mucus secretion [23]. The limitation of these models is the challenge to discriminate between the impact of mucus and other constituents of the system. Although this can be overcome by culturing the cells in different conditions that allow or not mucus secretion [30].

Various primary and immortalized cell types have been employed to investigate mucus nanoparticle interactions. Primary human bronchial epithelium (HBE) cells secrete mucus, possess cilia, and display ciliary motion, which makes this cell source a preferred model for human native mucosa [41]. An advantage of this model is that as they are harvested from humans and the disease phenotype can be incorporated by patient selection [42]. The limited accessibility, high interindividual variability, low reproducibility, and relatively higher costs of culturing are some of the difficulties of dealing with this model [30].

The Calu-3 cell line is a mixture of secretory and ciliated cells originating from submucosal adenocarcinoma [43]. Calu-3 cells show different properties dependent on whether they are cultured submersed in fluid or at an air-liquid interface (Figure 1.4).

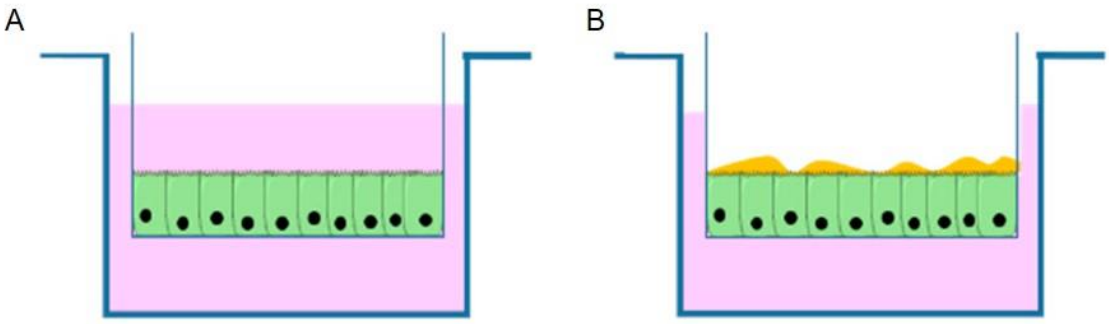

Figure 1.4: Cells cultured at the liquid-covered culture (LCC) (A) and cells cultured at the air-interfaced culture (AIC) (B). The figure has been adapted from [44].

Cultured at AIC conditions Calu-3 cells mimic at a large extent the native human mucosa. They form a tight monolayer, express tight junctions like occludin, E-cadherin, ZO-1 and secrete a confluent mucus layer, containing major gel-forming mucins like MUC5AC and MUC5B. Furthermore, Calu-3 cells express CFTR [45,46]. The above-mentioned properties

make Calu-3 cell line a quite relevant model for human pulmonary mucosa. The long culturing time required for a confluent mucus layer is a limitation of this model. 16HBE140 is another cell line model that differentiates to form a tight monolayer at air-interface conditions but does not secrete pulmonary mucins MUC5AC or MUC2 [23,47]. Co-cultures of Caco-2 cell line with mucus secreting cell line HT29-MTX, represent an *in vitro* mucus model for the gastric tract [23,48]. Easier accessibility, better reproducibility, and relative lower culturing costs are some of the advantages of those mucus producing cell lines [30]. Embryonic chicken trachea is another *in vitro* model that, allows the investigation of barrier properties of mucus considering its dynamic properties. This model enables the evaluation of the efficacy of aerosol medicines involving the dynamic properties of mucus in a system with functional mucociliary clearance [49].

The use of simpler systems like isolated and *in vitro* mucus models has largely improved the fundamental knowledge about the barrier properties of mucus. However, given the complex mucus composition, site dependent thickness, as well as its dynamic nature, the investigation of the interactions of drug and drug carriers with the mucus layer lining the real tissue offers the most realistic endpoint information regarding their diffusion efficiency [23]. For the studies using this mucus model, typically the drugs and particles are locally or systemically applied and tissues of interest are extracted [50]. This allows the investigation of the site-specific mucus penetration. The accessibility of samples of human origin is limited and often collectable during complicated procedures like surgeries etc. Therefore, mostly animal (*e.g.*, murine) originating samples are utilized. The high interindividual variability and subsequent low reproducibility is a drawback of this mucus model [23].

The models that recapitulate healthy mucus allow the understating of the basic principles of the healthy human mucus. However, for the investigation of mucus alterations in diseases like CF as well as for the evaluation of the efficacy and safety of aerosol medicines (*e.g.*, CFTR potentiator, antibiotics, etc.) is essential to use mucus models that mimic the *in vivo* pathophysiological conditions. CF sputum is an isolated CF relevant mucus model, which is collected during spontaneous expectoration of CF patients [34,51,52]. Artificial sputum medium, which shows a high similarity to CF patient sputum regarding composition has also been used as a CF model [51,53]. Upon the addition of a crosslinking polymer, the rheological properties were improved meeting the ones of healthy airway mucus [38]. The adjustment of the rheological properties of this model to human CF sputum would be of

interest for a more reliable use of this material as CF mucus model. Another CF relevant model is CFBE41o- cell line, which is homozygous for the ΔF508-CFTR mutation. However, a shortfall of this cell line is that it does not produce mucus. Murgia et al., (2017) overcame this limitation by complementing the cell line with exogenous mucus [54]. Nevertheless, the application of mucus over the cell line remains a challenging step of this technique, as it commonly results in a thicker mucus layer than the physiological situation. In addition, considering complementing of the cell line with CF sputum would further improve this model.

1.4. Methods to investigate the interaction of mucus with nanotherapeutics

The contact of mucus/ mucins with nanoparticle-based drug delivery systems can cause an alteration of physicochemical properties of nanoparticles like size and zeta potential. For example, it was shown that in mucus, positively charged nanoparticles revealed an increase of the particle size and a decrease of the zeta potential [55]. This was explained by probable adsorption of negatively charged mucins to nanoparticles. On the other hand, the retainment of charge and size of drug carriers can be interpreted as absence of mucus nanoparticle interactions [56].

Drug and particle interactions with mucus can also be investigated by evaluating the permeation of drugs through mucus. In such analysis drugs applied from a donor compartment diffuse through mucus lining a semipermeable membrane into an acceptor compartment. The rate of transport can be evaluated by measuring the amount of drug in the acceptor compartment. This concept has been utilized for the development of various systems like Ussing chamber [57–60], Side by Side [61,62], Transwell-based permeation assay [36,59,63]. The semipermeable membrane used in this system can besides mucus also play a barrier role leading to an overestimation of the barrier properties of mucus [15]. Furthermore, in such experiments the applied mucus layer is commonly thicker than the physiological situation, leading to long transport times through mucus and subsequently long experimental times.

Based on the relation between the diffusion coefficient and depth of diffusion another technique called silicone tube has been developed. Therefore, mucus is filled in silicone tubes and material of interest was applied in these tubes. Tubes were horizontally rotated in an incubator and finally sections of frozen tubes were analyzed regarding nanoparticle

diffusion [64]. The inclusion of steps like freezing is a drawback of this technique, as this might compromise the results [7].

Based on fluorescence signals, 3D time lapse is another technique that can be utilized for the investigation of the diffusion of drugs and drug carriers in mucus [56,65]. Z-stack images of stained mucus samples are recorded in defined time lapses after the application of particles. The total fluorescence signal (of diffusing practices) was detected in the reconstructed images and can be analyzed using image processing software (such as Image J). Based on this information the diffusion efficiency of drug delivery systems has been evaluated. This technique is also of interest especially for *in vitro* models, as it provides information about the directed transport of particles toward the layer of interest (epithelium).

Fluorescence recovery after photobleaching has also been employed for the investigation of the diffusion through mucus [12,66]. In this technique, the fluorescent material of interest is applied on the mucus sample. At a region of interest, images are carried out to define the baseline intensity (100%). Subsequently, this region is bleached leading to a decrease of fluorescent intensity (0%). After bleaching, time series are recorded at the same region. During this step, the fluorescent intensity increases as fresh fluorescent molecules enter the region. The fluorescence that increases from 0% to a saturation point is called fluorescence recovery. The percentage of fluorescence recovery delivers information about the percentage of mobile particles. In addition, values like diffusion coefficient can be determined based on the fluorescence recovery curve [15].

Multiple particle tracking is a widely used technique, which is employed for the investigation of the diffusion of fluorescently labeled particles (Figure 1.5) [6,11,38]. Therefore, microscopy videos are recorded and subsequently analyzed by using self-made or commercial image analysis algorithms. The X and Y displacement of each particle as a function of time is tracked and translated into individual particle trajectories. Based on these trajectories the mean square displacement of each particle and the ensemble mean square displacement (<MSD>) of multiple particles tracked simultaneously can be obtained [67]. Using the <MSD>, the diffusion coefficient (D) of particles can be calculated. MPT analysis can also be used to probe rheological properties and heterogeneity of the medium of interest.

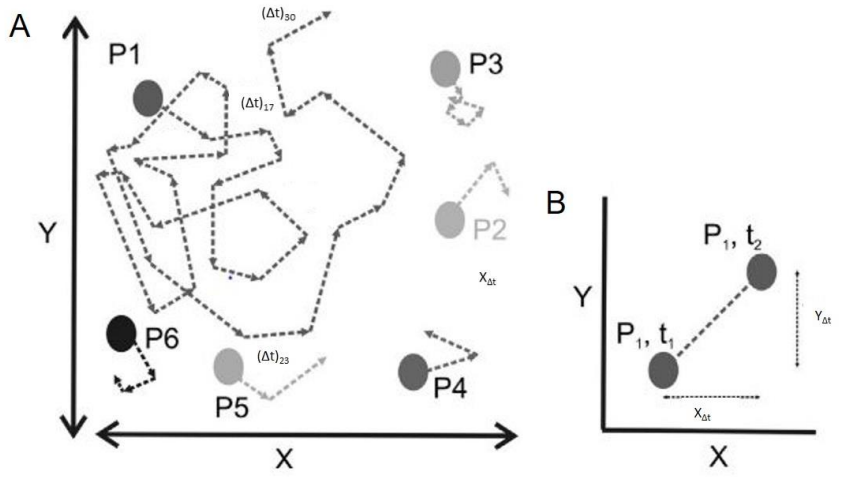

Figure 1.5: The particle movement in X-Y plane is recorded via microscopy videos and reconstructed into individual particle trajectories (A). The displacement of particles can be expressed as MSD = $[(X_{\Delta t})^2 + (Y_{\Delta t})^2]_{(\Delta t\ n\ =\ 1–30)}$ (B). The figure has been reprinted with permission from [67].

1.5. Concluding remarks

Mucus layer challenges the applied drug delivery systems by impending their transport through mucus to the underlying epithelia. In CF disease conditions, this challenge of crossing mucus and releasing cargo in the target cells is far more enhanced, due to factors like increased mucus viscosity, impaired clearance, and microbial colonization. Therefore, understanding of the principal properties of mucus, its healthy and diseased conditions as well as a realistic and non-biased evaluation of the interaction of drug carriers with relevant mucus models is essential for an efficient drug delivery development. Several mucus models and analytical techniques have been developed for a realistic evaluation of the fate of drug carriers, once applied on the mucus layer. The selection of the right technique and mucus model is essential for these studies. The ideal mucus model and analytical technique should resemble the human physiology, disease state, and drug application to the greatest extent possible. However, also other parameters like reproductivity, ease of use, as well as costs need to be considered. In this context, it should be found a compromise between advantages and disadvantages of models and techniques of interest, or it should be considered the option of extending the knowledge regarding drug carrier efficacy by employing various mucus models and techniques.

2. Aim of this work

Human pulmonary mucus efficiently protects the underlying airway epithelium from pathogens and xenobiotics. However, it also challenges the transport of beneficial therapeutics. Understanding of the mucus layer and the availability of well characterized mucus models are essential for the development and assessment of trojan horse drug delivery systems able to overcome the mucus barrier.

The overall aim of this work was to improve the understanding of pulmonary mucus as a barrier for drug delivery. Therefore, the following objectives are stated:

- To elucidate the structure of human pulmonary mucus in its native hydrated state by employing various microscopy techniques (Chapter 3). The structure of mucus has been primarily investigated via conventional electron microscopy. It has been hypothesized that vacuum operating conditions and sample preparation steps required for this technique might alternate the structure of mucus. Therefore, super-resolution microscopy has been employed in order to allow the visualization of mucus in its hydrated state.
- To characterize and evaluate the usefulness of *in vitro* mucus layer produced from Calu-3 cells and compare it to human pulmonary mucus (Chapter 4). Therefore, both mucus models were evaluated in terms of mucins, macrorheology, particle transport, and metabolomic profile.
- To assess the impact of mucus modulation as a mucus overcoming strategy on the barrier/ protective function of mucus by using Calu-3 *in vitro* mucus (Chapter 5). Modulation of mucus allows an enhanced mucus penetration. However, it is not clear if the modulation of the mucus layer might have an influence on the protective potential of mucus. Therefore, the cytotoxicity of Calu-3 cells was assessed upon exposing of the samples to aerosolized N-acetylcysteine (mucus modulator) and model polystyrene particles.

3. Visualization of the structure of native human pulmonary mucus

This chapter has already been published in the following research paper:

E. Meziu, M. Koch, J. Fleddermann, K. Schwarzkopf, M. Schneider, A. Kraegeloh.; *Visualization of the structure of native human pulmonary mucus*. *Int. J. Pharm. 597 (2021) 120238.*

Author contributions

E.M., M.S., A.K., designed the study. E.M. performed sample preparation and light microscopy imaging. M.K. carried out electron microscopy. K.S. took and provided samples of human pulmonary mucus. E.M., M.K., J.F., K.S., M.S., A.K. contributed to data analysis and E.M. together with M.K., J.F., K.S., M.S., and A.K. wrote the paper. All authors have given approval to the final version of the manuscript.

Abstract:

Human respiratory mucus lining the airway epithelium forms a challenging barrier to inhalation therapeutics. Therefore, structural elucidation of hydrated mucus is essential for an efficient drug delivery development. The structure of mucus has been primarily investigated by conventional electron microscopy techniques, which operate under vacuum conditions and require sample preparation steps that might alter the structure of mucus. In this study we investigated the impact of dehydration on mucus and analyzed the structure of mucus in its hydrated state. Cryo-scanning electron microscopy (Cryo-SEM) analysis of mucus showed, that during the process of sublimation, non-porous structure of mucus is transformed into a porous network. Similarly, images acquired by environmental scanning electron microscopy (ESEM), revealed a non-porous structure of hydrated mucus, while further observation of the structure of mucus at decreasing pressure demonstrated the strong influence of dehydration on mucus structure. We could successfully visualize the structural organization of the major gel-forming mucin MUC5B in its hydrated state by employing stimulated emission depletion (STED) microscopy, which allowed resolving the nano-scale patterns of mucin macromolecules within the essentially pore-free mucus structure. The general structural organization of mucus components was addressed by confocal laser scanning microscopy (CLSM), which revealed the heterogeneous and composite structure of mucus. These results provide a novel view on the native structure of mucus and will affect drug delivery development.

3.1. Introduction

Human respiratory mucus is a viscoelastic biological hydrogel lining the conduction zone of the respiratory tract that hydrates, lubricates, and protects the underlying epithelia [1,6,16,68]. In the healthy state, mucus consists primarily of water (~95% w/w) and incorporates several other substances like mucins (~0.2-5.0% w/v), non-mucin proteins, lipids, DNA, salts, cells, and cell debris [14]. Highly glycosylated mucin glycoproteins entangle to create the gel structure of mucus, which represents a challenging barrier for transmucosal drug delivery systems administered via the pulmonary route [14,15,69]. The mucus layer diminishes the nanoparticle penetration behavior due to its high interaction potential (interaction filtering) and steric obstruction (size filtering) [16]. Inhaled

nanoparticles that get entrapped in the pulmonary mucus gel are excreted within few hours by mucociliary clearance [10,70]. Therefore, the transport of nanoparticles through the mucus layer within the time frame determined by mucus turnover and mucociliary clearance is challenging [15].

Strategies for the development of drug delivery systems that overcome the mucus barrier have been guided by the information about the structure and chemical properties of mucus [71]. It has been shown that, adjusting the size and surface chemistry of nanoparticles to the structural and biochemical properties of mucus leads to an improvement of the nanoparticle transport through mucus [12,72]. In this context understanding of the architecture of the mucus barrier is essential for the optimization of the delivery nanoparticles through the mucus barrier and development of efficient pulmonary drug carrier systems. For example, Schuster et al., (2017) reported a long-distance diffusion of pegylated nanoparticles over a length of 10 micrometers, which was explained by the presence of interconnected porous microdomains [73]. This information regarding the structure of mucus can be used to interpret the efficiency and conclude on required doses of the applied drug delivery systems.

Tracking of the movement of dispersed nanoparticles in mucus has been employed to probe the structure of mucus. Particle tracking led to assumptions about the structure of mucus, which ultimately should be cross checked by visualization techniques. Particle tracking studies have shown an increase in the nanoparticle mobility with the decrease of the particle size and have reported a cut-off size of 500 nm for nanoparticle transport through mucus [12,74]. The structure of respiratory mucus has been also investigated by scanning electron microscopy (SEM) studies, which have described mucus as a heterogeneous porous network [11,31,32]. However, it has already been acknowledged, that imaging of mucus by applying electron microscopy might result in structural alterations of mucus structure, due to dehydration procedures and vacuum operating conditions required for this technique [11,12,15,69]. Another study that used electron microscopy to analyze respiratory mucus described that different dehydration procedures resulted in different mesh sizes of mucus network, highlighting the impact of dehydration on the visualized mucus structure [15]. Atomic force [75] and Raman confocal microscopy [31] analysis have also revealed a porous structure of air-dried and freeze-dried mucus respectively. Confocal laser scanning microscopy (CLSM) analysis of respiratory mucus from

healthy patients indicated a filamentous architecture of mucus [76]. Duncan et al., (2016) have reported a negative fluorescence staining method for mucus visualization by applying fluorescent dextran to stain the fluid phase of mucus [7]. By using this technique, they reported the strong patient to patient structural differences of mucus. In addition, cryo-scanning electron microscopy (cryo-SEM) analysis has been applied for the visualization of the structure of respiratory mucus. This technique is regarded to allow for high resolution visualization as well as preservation of the native state of the specimen due to cryo-fixation (transition of liquid water into amorphous ice, which shows the most similarity to liquid water) [8,15,70]. However, even this technique might introduce artefacts, due to inefficient cryo-fixation because of insufficient cooling rates and sample thickness, which lead to unwanted formation of ice crystals and consequently structural damage and erroneous images [77]. We hypothesize that the process of sample preparation as well as dehydration might have altered the structure of mucus, as a result deviating from its hydrated state. Therefore, in this study we investigated the impact of plunge freezing and dehydration on mucus structure visualized by microscopy. In a first step, the structure of mucus was observed *in situ* during the process of sublimation of ice. We observed that the porous structure of mucus is created as a function of freezing as well as sublimation, indicating that the native structure of mucus is altered during sample preparation and SEM imaging. To extend the picture beyond the state of the art, we aimed for structural elucidation of mucus in its hydrated state. Hence, the structure of mucus was investigated by applying environmental scanning electron microscopy (ESEM), as a technique, which allows the visualization of hydrated specimens. Beside of electron microscopy, confocal laser scanning and stimulated emission depletion (STED) microscopy, providing a resolution closing the gap between optical and electron microscopy, have been employed for visualization of gel-forming MUC5B mucin using immunostaining procedures. Finally, the structural organization of several mucus constituents in their native state has been investigated by light microscopy.

3.2. Materials and methods

3.2.1. Mucus sample collection

Samples of human respiratory mucus were collected using the endotracheal tube method

[29]. The distal part of tracheal tubes of patients, who required intubation for surgery was cut and placed in a falcon tube. Subsequently these samples were centrifuged at 10.000 g for 10 min at 4 °C. After centrifugation, mucus was collected in an Eppendorf tube using a positive displacement pipette. Collected samples were primarily fresh collected and stored at 4 °C for > 24 h and maximum 1 week until use or stored at -80 °C and thawed overnight at 4 °C before analysis. An investigation of the impact of freezing on the structure of mucus showed no strong influence of freezing on our main observations (Supplementary information, Figure S3.6). The sample containers were sealed to avoid dehydration and were stored at low temperature to reduce/avoid dehydration and the activity of proteolytic enzymes potentially changing mucus structure [7]. Mucus samples with visible blood contamination were discarded. In total 16 mucus samples from independent patients were used in this study. The mean age of the patients involved in the study was 65.22 ± 15.51 years, male: female ratio was 5:3. Patients were non-smokers and had no pulmonary disease.

3.2.2. Immunostaining

Mucus samples (30 µl) were placed in an Eppendorf tube, fixed for 30 min using 4% (v/v) paraformaldehyde (Electron microscopy science, UK) and blocked with 5% (w/v) bovine serum albumin (Carl Roth, Germany) for 30 min. Due to its high affinity for N-acetyl-β-D-glucosaminyl residues, wheat germ agglutinin was used to stain these residues within mucins and whole cells. Samples were treated with (10 µg/ml) wheat germ agglutinin (WGA) Alexa Fluor 488 (Life Technologies, USA) for 30 min at room temperature (RT). In addition, mucin MUC5B was stained applying (2 µg/ml) mouse anti-MUC5B antibody as primary antibody (Thermo Fischer Scientific, Germany) for 3 hours at RT and (2 µg/ml) goat anti-mouse antibody as secondary antibody (Atto 647N) (Sigma-Aldrich, Germany) for 12 hours at 4 °C. DNA was stained with (2 µg/ml) Hoechst 33342 (Invitrogen, Life Technologies, USA) for 1 hour at RT. After each staining step, samples were washed with 30 µl Dulbecco`s phosphate buffered saline, except before Hoechst staining (30 µl MilliQ water). Finally, samples were embedded in Mowiol/(1,4-Diazabicyclo(2,2,2)octan) (DABCO) (Sigma-Aldrich, Germany).

3.2.3. Freeze-drying of mucus

In order to investigate the influence of sample preparation on mucus structure, freeze-dried mucus was prepared. Native mucus (500 µl) was freeze-dried in an ESEM, starting at a temperature of 276 K and a pressure of 800 Pa. In order to achieve a controlled freeze-drying, both temperature and pressure were continuously decreased to 243 K and 100 Pa. The freeze-dried mucus was investigated by CLSM and SEM. Immunostaining of mucus was performed prior to freeze-drying. SEM imaging of freeze-dried mucus was performed inside an ESEM operating at low vacuum mode (100 Pa), applying an accelerating voltage of 10 keV and a Large Field Detector. To evaluate the images, a pore size analysis was performed by using Image J (National Institute of Health, Version: 1.45a; http://rsbweb.nih.gov/ij/). The data regarding pore size distribution are revealed in a histogram with a bin width of 0-2 µm.

3.2.4. Cryo-scanning electron microscopy (Cryo-SEM)

Mucus samples were placed on circular 8 mm steel-plates and cryo-fixed in liquid ethane at -165 °C using a Gatan Cryoplunge-3 to allow for formation of amorphous ice and limit the formation of crystalline ice. The frozen samples were then transferred under liquid nitrogen to a pre-cooled brass block, serving as cryo-SEM holder. The temperature of this passive cooling holder has been described to keep the temperature of the sample below -120 °C within 60 min [78]. Imaging was performed using a FEI Quanta 400 FEG ESEM in high-vacuum mode using an Everhart-Thornley detector and acceleration voltages of 3 keV. After transfer of the cryo-SEM sample holder into the SEM chamber, images were taken while sample temperature was between -196 °C and -120 °C [79].

3.2.5. Environmental scanning electron microscopy (ESEM)

ESEM has been applied in order to investigate the structure of hydrated mucus in a saturated water vapor containing atmosphere. Mucus samples were placed on an aluminum holder and transferred onto a Peltier cooling stage at 276 K inside a FEI Quanta 400 FEG ESEM. Initially, water vapor was introduced into the ESEM chamber several times in order to prevent sample dehydration. Images were taken at a water vapor pressure of 800 Pa and a temperature of 276 K at 10 keV accelerating voltage using a gaseous secondary analytical detector. According to the pressure-temperature phase diagram of

water, under these conditions water is in its liquid state close to the phase boundary between liquid and gaseous water. Thus, these temperature and pressure conditions allow visualization of mucus in its fully hydrated state [80,81]. Subsequently, mucus samples were dehydrated by decreasing the water vapor pressure continuously to 100 Pa at 276 K. Below 750 Pa, water evaporates, therefore, under these conditions, dehydration of the samples occurs.

3.2.6. Confocal laser scanning microscopy (CLSM)

Mucus samples were analyzed using the TCS-SP5 STED setup (Leica Microsystems, Germany) equipped with oil immersion objectives 63X/1.4 and 100X/1.4 (HCX PL APO, Leica, Germany). Alexa 488 labeled WGA and Atto 647N labeled anti-mouse antibody were excited by using an argon laser (488 nm) and a HeNe laser (633 nm), respectively. Hoechst 33342 was excited using a pulsed MaiTai Ti:Sa laser (Spectra-Physics, USA) at 750 nm (pulse width < 80 fs) for two-photon excitation. The fluorescence signals of Alexa 488 and Hoechst 33342 were detected using Photo Multiplier Detectors, whereas the signal of Atto 647N was detected using an Avalanche Photo Diode (APD) module. The quality of images was improved by adjusting the brightness, sharpness and contrast by using the image processing software ImageJ.

3.2.7. Stimulated emission depletion microscopy (STED)

For STED microscopy Atto 647N was excited using a pulsed diode laser (635 nm) (PicoQuant, Germany) and depleted using a pulsed Ti:Sa laser (780 nm). The signal of Atto 647N was detected using an APD (Perkin-Elmer SPCM-AQRH). As an indicator for the lateral resolution in STED mode, dark red (660/680) 0.04 µm carboxylate modified FluoSpheres™ (Invitrogen, Life Technologies, USA) were imaged. The beads were diluted in water (0.0005% solids) and dried on glass cover slips prior to embedding in Mowiol/DABCO and STED imaging. Intensity profiles of the fluorescence signals were measured using 20 signals in order to determine the full width at half maximum of the experimental point spread function (PSF) in the focal plane. The experimental PSF was determined to be 87 ± 23 nm in STED mode. The resolution of confocal microscopy was reported as 277 nm [82].

3.3. Results and discussion

3.3.1. The impact of sample preparation on the structure of mucus

Cryo-SEM analysis has been employed for the investigation of respiratory mucus in order to minimize the structural alteration of the mucus structure [8,15,27]. However, in these studies the structure of mucus is regarded as preserved after plunge-freezing of the sample, during further sample processing, and imaging under vacuum conditions. An evaluation of the quality of cryo-fixation by analysis of mucus after plunge-freezing and subsequent sublimation of ice is still missing. Therefore, in the present study we performed *in situ* sublimation to observe its impact on the visualized mucus structure (Figure 3.1 A-C).

At the beginning of the sublimation process, a non-porous but granular structure of mucus could be observed (Figure 3.1 A). During the process of sublimation, the structure of mucus was altered, and walls of the up-coming pores became clearly visible (Figure 3.1 B). Remarkably, we could observe, that the process of sublimation caused the structural alteration of compact mucus into a porous scaffold (Figure 3.1 C) similar to previous shown cryo-SEM data [8].

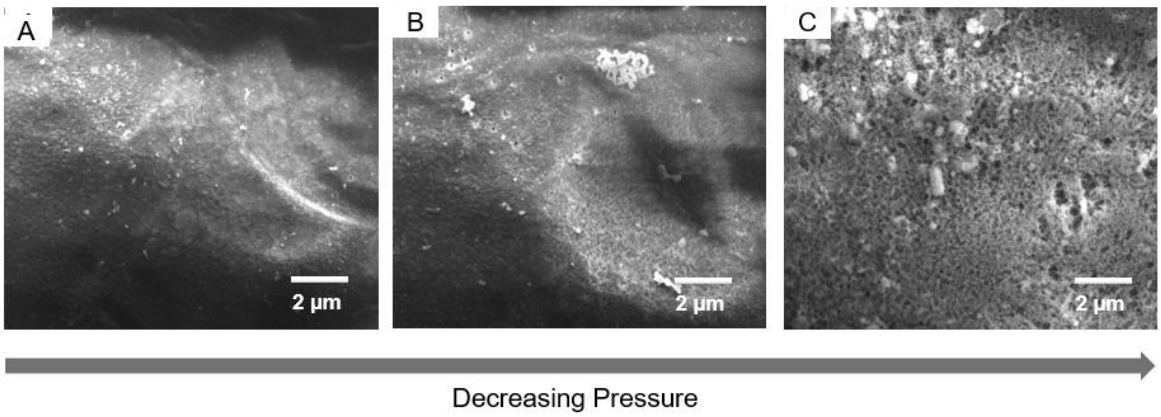

Figure 3.1: Pore formation during EM imaging of plunge-frozen mucus. A series of cryo-SEM images of the same region of plunge-frozen mucus is shown: A) sample imaged 7 min after the start of vacuum initialization, B) beginning pore formation imaged 7 1/2 min after the start of vacuum initialization, and C) porous structure of mucus formed as a result of ongoing sublimation, imaged 10 1/2 min after vacuum initialization. Images are representative of two independent patients. Mucus was freshly collected and refrigerated.

During the progression of sublimation, the pores changed in form and size, and the porosity of mucus increases (Supplementary information, Video S3.1). We assume that the network structure of mucus is obtained by formation of ice crystals during plunge freezing followed by the sublimation of ice under high vacuum conditions. The granular structure of the frozen bulk mucus indicates an insufficient freezing velocity to avoid ice crystal formation. Different cooling rates within the sample (several mm thick), might be the reason for ice crystal formation even during plunge-freezing [83]. In comparison, cryo-TEM investigations of thin mucus samples (several µm thick) showed no ice crystal formation using the same experimental setup for sample preparation (Supplementary information, Figure S3.3). The phase separation occurring within thick mucus samples then causes formation of a dry polymer phase after sublimation of the ice, remaining as a porous network. Our observation regarding the impact of freezing and sublimation on the formation of a porous network correlates fairly well with findings of Ivan'kova et al., (2016) for a single component system, who also observed the formation of a chitosan sponge during *in situ* sublimation of chitosan solution in a cryo-chamber [84].

To follow this process in more detail and avoid ice formation, we analyzed the structure of mucus by using ESEM, as a technique which allows high resolution visualization of hydrated samples. The surface of hydrated mucus visualized by ESEM was found to be smooth and continuous at the applied magnification (Figure 3.2).

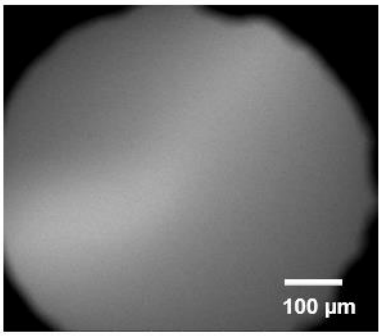

Figure 3.2: ESEM image showing the even surface structure of mucus in its hydrated state. Image is representative of two independent patients. Mucus was freshly collected and refrigerated.

This ESEM micrograph of hydrated mucus confirms our hypothesis that hydrated mucus is a biological hydrogel, without pores in the hydrated state. Together, these data indicate that the porous structure of mucus observed in cryo-SEM is an artefact of the process of

inefficient cryo-fixation followed by dehydration. This emphasizes the importance of the application of imaging techniques that are independent from handling of samples in frozen state or under vacuum.

3.3.2. The structure of mucus revealed by STED microscopy

As described above, the dehydration process was found to alter the structure of mucus. Thus, we sought to apply fluorescence microscopy to enable the imaging of mucus in its hydrated state, without vacuum and low temperature requirements. Cryo-SEM data have reported a network structure of mucus with a pore size varying from 100 nm to several micrometers [8]. Therefore, in addition to conventional CLSM, STED microscopy as a sub-diffraction resolution imaging technique (Supplementary information, Figure S3.4) was chosen to gain insight into the native structure of mucus.

To preserve the structure of mucus and avoid structural alterations that might occur during subsequent staining steps we fixed the samples with 4% paraformaldehyde (PFA) [85], which has been described to preserve the structure of mucus. An *in situ* investigation of the impact of the fixation procedure on the structure of mucus by using CLSM indicated that a strong influence of these sample preparation steps can be excluded (Supplementary information, Figure S3.1). We further observed that dilution (which occurs during the process of staining) of the fixed samples, showed no strong impact on the structure of mucus (Supplementary information, Figure S3.2).

CLSM and STED images of mucus (Figure 3.3 A and B) depict the heterogeneous structure of mucus characterized by large voids (non-labeled areas) of ~ 10-20 µm in diameter. As the samples were stained using only anti-MUC5B antibody, the non-labeled areas might be filled with non-stained mucus constituents, which are not visible in these images. We additionally co-stained for MUC5AC and qualitatively observed a partial colocalization of both mucins (Supplementary Information Figure S3.7). MUC5B primarily secreted from submucosal glands and MUC5AC secreted from the goblet cells associate with each other once secreted and move up the airway [86]. Given this it would be expectable that collected samples, which undergo a mechanical treatment during the process of collection would show a colocalization of both mucins. Esther et al., (2019) similarly reported that MUC5AC and MUC5B were found intermixed in cystic fibrosis (CF) and non-CF samples. Therefore, only MUC5B was used for further visualization.

The magnified views of the marked regions (Figure 3.3 C-D) reveal a granular and non-porous structure of mucus. This finding was supported by super-resolution STED imaging. As can be seen in the enlarged sections, (Figure 3.3 E and F) mucin agglomerates (patches) could be resolved to reveal separated MUC5B positive spots. As illustrated in Figure 3.3 G, the spotted structure of mucus might be due to binding of the anti-MUC5B antibody to the N-termini of MUC5B monomers. Mucin monomers (400-500 nm) possess cysteine-rich N- and C-termini, which are involved in formation of disulfide bridges and the polymerization of MUC5B [87]. The anti-MUC5B antibody used for staining binds to the N-termini of MUC5B creating antigen-antibody complexes. Therefore, dependent on the distance between several N-termini, either separate N-termini (monomers) or assemblies of the N-termini (multimers) of the entangled MUC5B could be responsible for the spotted pattern of mucus image. As described in Figure 3.3 G, STED imaging reveals substructures (monomers or multimers) of mucin macromolecules (agglomerates), which could not be resolved in the CLSM image.

To our knowledge, this is the first time that hydrated human pulmonary mucus was investigated using super-resolution microscopy revealing substructures of the macromolecule MUC5B. It is noteworthy, that by using conventional confocal imaging as well as STED imaging using hydrated mucus samples, a porous structure of hydrated mucus as seen in cryo-SEM (Figure 3.3 B, D, F) could not be observed. These data are also in accordance with ESEM images of hydrated mucus. Therefore, it can be concluded that in order to study the structure of mucus, a biological hydrogel, it is necessary to keep the samples in a hydrated state. In addition, due to the dimension of the macromolecular building blocks, super-resolution imaging is essential to study mucus structure in detail.

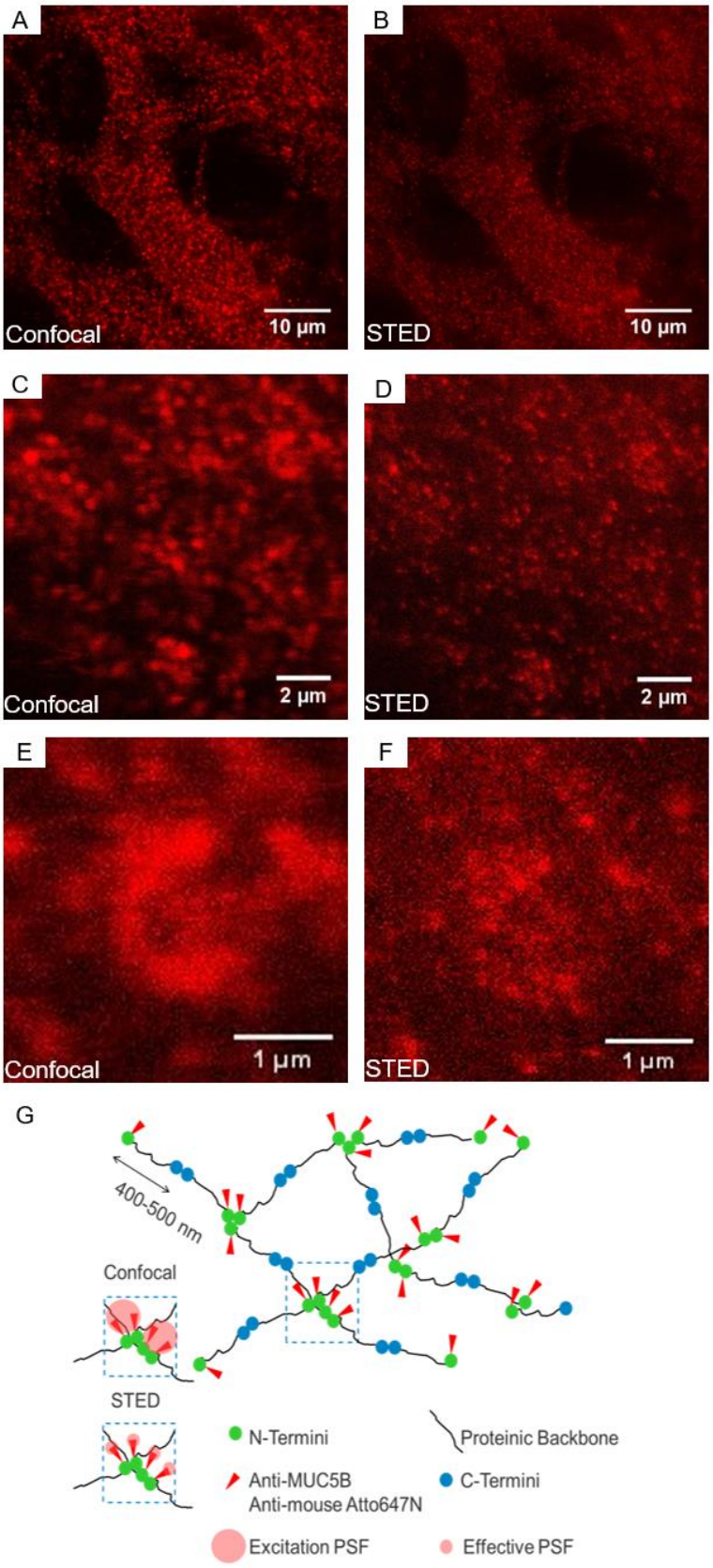
A
Confocal
10 µm
B
STED
10 µm
C
Confocal
2 µm
D
STED
2 µm
E
Confocal
1 µm
F
STED
1 µm
G
400-500 nm
Confocal
STED
N-Termini
Proteinic Backbone
Anti-MUC5B
Anti-mouse Atto647N
C-Termini
Excitation PSF
Effective PSF

Figure 3.3: Hydrated mucus exhibits a mainly compact and granular structure. A) and B) are overview CLSM and STED images of the same region of mucus, respectively. Closer views of the marked regions C) and D) show the compact and granular structure of mucus. Further enlargements show mucin agglomerates E) that are resolved into distinct spots (mucin multimers) by STED microscopy F). G) is an illustration of mucus STED microscopy, which allows resolving of MUC5B multimers. This illustration is realized based on a current model of the polymeric structure of MUC5B [87], possible structure of antigen antibody complexes and results of CLSM and STED imaging. Antibody complexes (red triangles) bind to the N-termini (green circles) of entangled MUC5B (polymeric structure of MUC5B is adopted from Janssen et al., (2016) [87]). We assume that the spotted pattern of mucus images stands for the N-termini assemblies of MUC5B multimers. Large and small red circles indicate excitation PSF and effective PSF respectively and illustrate the improved resolution realized by STED microscopy. Images are representative of four patients. Mucus was freshly collected and refrigerated.

3.3.3. Freeze-drying induces pore formation in mucus

In contrast to cryo-electron microscopy after sublimation of ice, fluorescence microscopy revealed a compact structure of hydrated mucus. This was assumed to be due to different sample preparation methods required for these techniques. To substantiate the discrepancies between electron and fluorescence microscopy, we compared CLSM images of native hydrated mucus with CLSM and SEM images of freeze-dried mucus.

The CLSM images of hydrated mucus (Figure 3.4 A and D) reveal a non-porous granular structure of mucus characterized by some non-labeled areas of 10-20 µm in size. In contrast, CLSM and SEM images of previously freeze-dried mucus show a clearly porous structure of mucus (Figure 3.4 B, E, and C, F). These data indicate that sample preparation methods and imaging techniques including freezing and dehydration have a substantial impact on the structure of mucus. *In situ* freeze-drying of mucus similarly showed formation of pores during the process of freeze-drying (Supplementary information, Video S3.2).

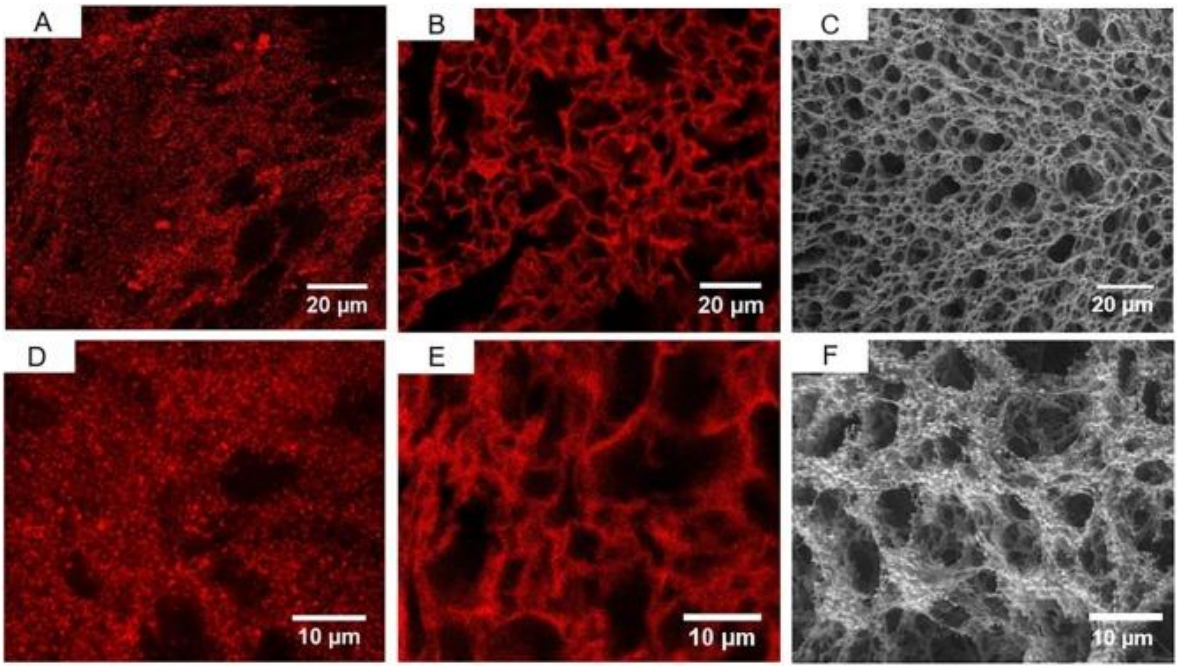

Figure 3.4: The impact of freeze-drying on mucus structure. A) and D) CLSM images of hydrated mucus. B) and E) CLSM images of freeze-dried mucus. C) and F) SEM images of freeze-dried mucus. Mucus was stained with primary anti-MUC5B antibody and secondary anti-mouse Atto 647N antibody. For CLSM imaging of freeze-dried mucus, staining was performed prior to freeze-drying. The images shown are from freshly collected and refrigerated mucus. These are representative images of 3 individual patients for native mucus and 3 individual patients for freeze-dried mucus. For a better comparability, identical patients have been used for CLSM and ESEM imaging of freeze-dried mucus. Therefore, in this figure images A, D, are of 1 patient, while images B, E and C, F are of another patient.

This impact was further confirmed by a quantitative analysis of the number and size of pores in mucus using SEM micrographs and confocal images (Figure 3.5). Native mucus evaluated by CLSM exhibited only a small number of pores as indicated by the pore size distribution histogram. In comparison, CLSM and SEM images of freeze-dried mucus showed a much higher number of pores. In addition, SEM images of freeze-dried mucus showed a larger number of pores as compared to CLSM images of freeze-dried mucus. This might be due to differences in resolution, contrast, and background noise.

For the evaluation of mucus porosity from the micrographs, the pore area fraction (percentage of the area covered by the pores out of the total analyzed area) was considered

to correspond to the pore volume fraction (porosity). The porosity of hydrated mucus imaged by CLSM was smaller (4.0 ± 1.6%) than the porosity of freeze-dried mucus imaged by CLSM and SEM (23.1 ± 4.3% and 33.0 ± 2.4%) respectively.

The CLSM images of hydrated mucus showed a mean pore size of 2.9 µm. The CLSM and SEM images of freeze-dried mucus revealed a mean pore size of 3.6 µm and 0.5 µm respectively. We found larger values of the average mesh spacing with respect to previously reported electron microscopy data (100 and 200 nm for cervicovaginal mucus [66,88] and intestinal mucus [89] respectively). A possible explanation for this discrepancy might be the application of different sample preparation methods. Murgia et al., (2018) reported the impact of the dehydration method on the mesh spacing of mucus, where freeze-dried mucus showed a larger mesh size as compared to cryo- and glutaraldehyde fixed mucus [15]. Hence, the larger mean pore size of mucus in this study might be due to the application of freeze-drying for sample dehydration. Nevertheless, pore size distribution is a more adequate parameter rather than the average mesh spacing for evaluation of mucus structure [15].

These data show that the discrepancies between electron and fluorescence microscopy are mostly due to sample preparation differences and the porous structure of mucus might be a result from the preparation process of freezing/ freeze-drying.

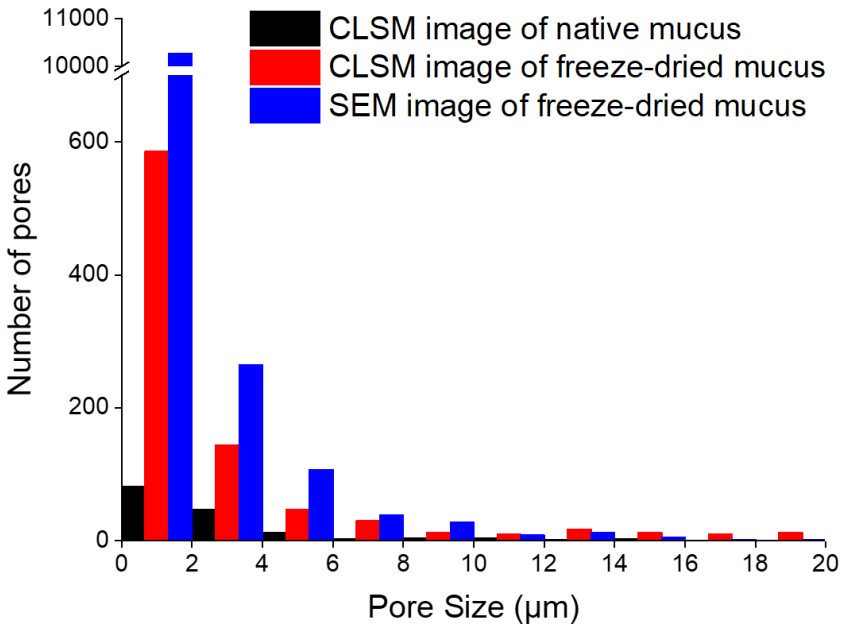

Figure 3.5: Histogram of the pore size distribution in native and freeze-dried mucus. Mucus samples were analyzed by CLSM and SEM. Histogram is prepared by analysis of three images for each technique (obtained by one representative native and one representative freeze-dried mucus sample). The few values larger than 20 µm are not presented in the histogram. Mucus was freshly collected and refrigerated.

3.3.4. A model of mucus based on fluorescence microscopy analysis

Mucus is a complex material, composed of multiple components [1,90], whereas the information gathered from CLSM images is based only on the labeled substances. In this context, labeling and imaging of a large fraction of the present material is essential for a realistic and comprehensive view of a complex and heterogeneous material like mucus, as non-labeled areas might falsely be interpreted as pores. Therefore, in this study the structural organization of human pulmonary mucus stained for multiple constituents was investigated by CLSM.

One of the two major gel-forming mucins MUC5B [91] was labeled with anti-MUC5B-Atto647N antibody; other mucin constituents and cell membranes were labeled with WGA-Alexa Fluor 488 as reported [51] and DNA was labeled with Hoechst 33342.

The overview image of mucus (Figure 3.6 A) illustrates its heterogeneous structure. At higher magnification (Figure 3.6 B) mucin strand is revealed, characterized by wispy

filamentary (WGA channel) and network-like regions (anti-MUC5B channel). It can be observed that WGA and anti-MUC5B antibody staining were colocated in some regions. This is due to binding of WGA to the MUC5B molecules. Ostedgaard et al., (2017) have also reported a colocalization between WGA and anti-MUC5B [86]. This might be due to the affinity of WGA-Alexa Fluor 488 to N-acetylneuraminic acid (sialic acid; SA) and N-acetylglucosamine (GlcNAc) residues of mucin glycoproteins [18]. However, in most of the analyzed regions, anti-MUC5B antibodies and WGA exhibited different staining patterns (Figure 3.6 B-D). Additionally, Figure 3.6 C reveals the presence of cells within mucus. Cell membrane and cell nucleus can be identified from WGA-Alexa Fluor 488 and Hoechst 33342 channels respectively. Interestingly, nuclei of different sizes could be observed in this image, which could be due to different types of cellular material present in mucus. Figure 3.6 D illustrates that in some cases non-labeled areas of WGA -Alexa Fluor 488 were filled with MUC5B. Additionally, irregular fragmented DNA can be observed in the Hoechst 33342 channel of this image. This implies the presence of degrading cells and cellular debris in mucus. Previous studies have also reported the presence of DNA [92] and floating cells [40] in *ex vivo* mucus, which might be related to cell shed or are of bacterial origin [92]. Overall, mucus appears as rather compact material not exhibiting a regular pattern of pores. In addition, its structure resembles a composite made up of various regions that are preferentially stained by different marker molecules (Figure 3.6).

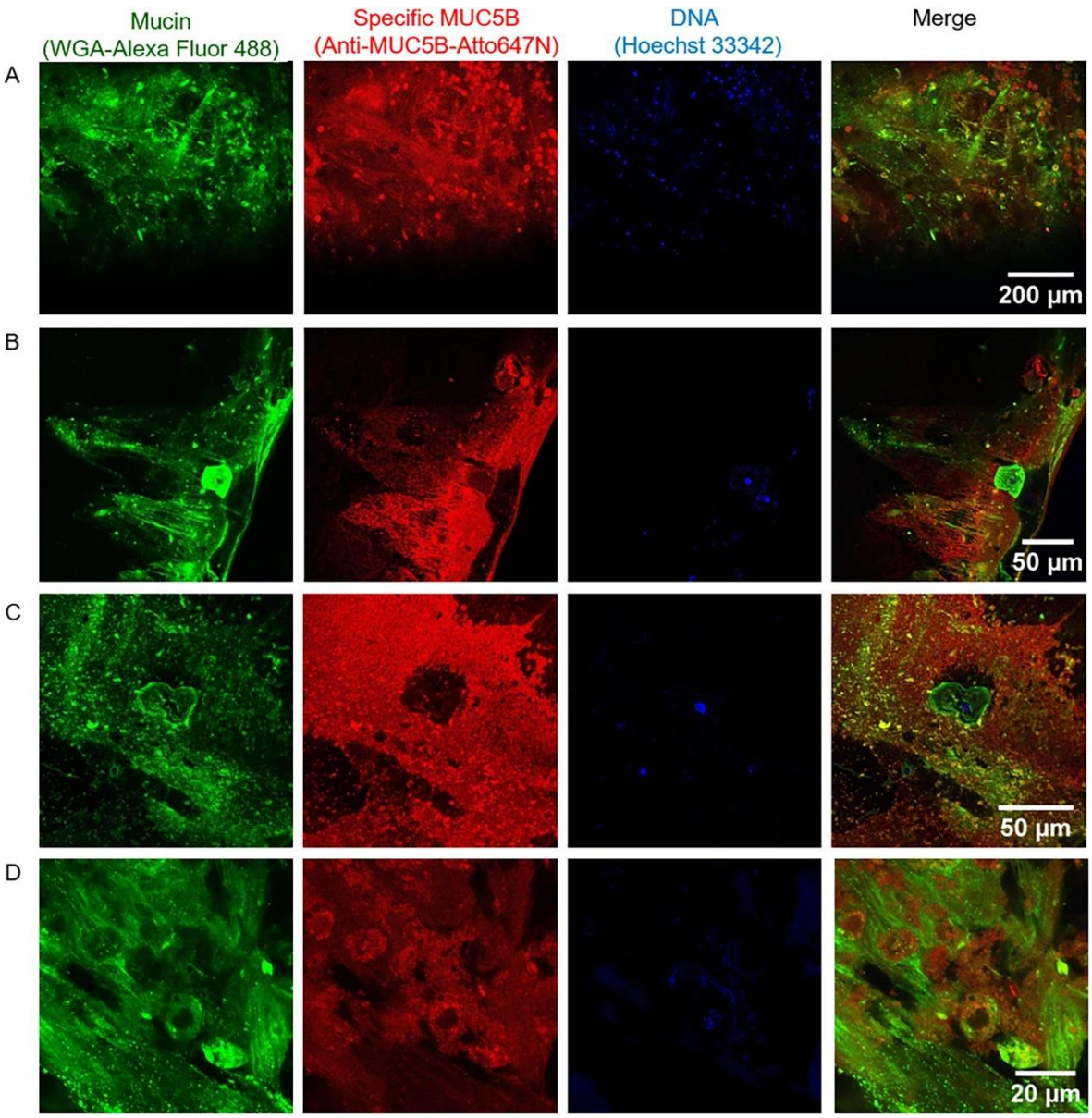

Figure 3.6: Multiple labeling and CLSM analysis reveal the composite structure of mucus. Repetitive structural features of mucus were observed by CLSM: A) overview image of mucus depicting differential arrangement of different mucus constituents, B) mucus region revealing the filamentary structure of mucus, C) cells of different sizes within mucus, and D) degraded cell nuclei and cell debris within mucus. Mucus was stained with anti-MUC5B-Atto 647N antibody (red), WGA-Alexa Fluor 488 (green) and Hoechst 33342 (blue). These are representative images of 3 individual patients. The images shown are from freshly collected and refrigerated mucus.

It must be noted, that despite the high heterogeneity of mucus samples from different patients but also within one sample, some representative structural motifs could be

observed. Based on CLSM images and z-stack analysis of mucus (Supplementary information, Figure S3.5) a schematic illustration of mucus composite is depicted in Figure 3.7.

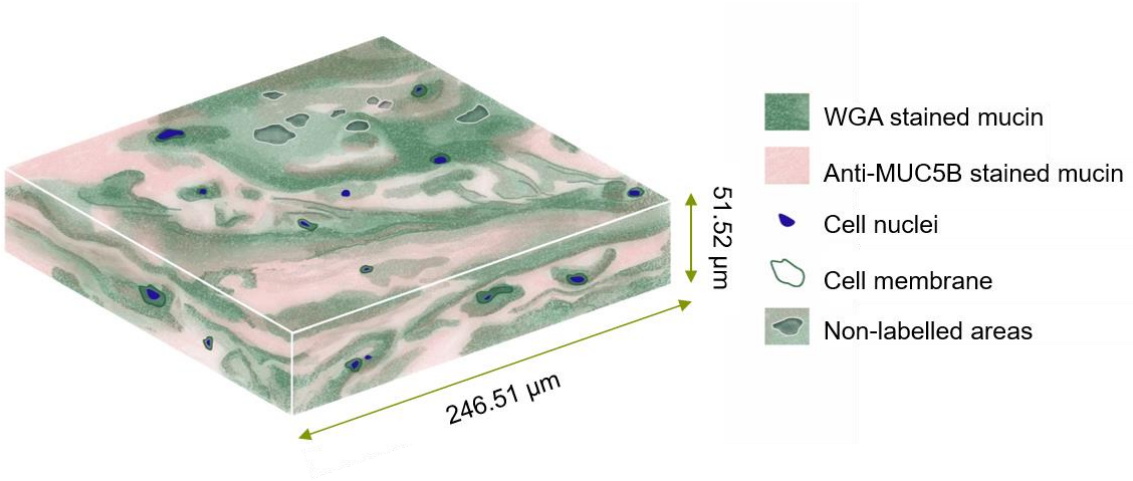

Figure 3.7: Schematic illustration of mucus depicting repetitive structural motifs observed using CLSM imaging. The illustration has been prepared by using Illustrator Photoshop.

Based on these data the structure of mucus can be described as a heterogeneous and compact material characterized by voids filled with other materials like cells, fluid, other non-mucin proteins as well as few of non-labeled voids.

We assume that mucin polymers/strands entangle with each other dynamically due to several interaction mechanisms creating some spaces between them [93]. However, we conclude that these spaces are not as regularly arranged and are not in the size-range as has been shown before [8,11,32]. This is supported by the confocal and STED images, indicating the presence of highly interacting polymer molecules visible as granules instead of regular water-filled pore regions. We assume that mucus is a dynamic hydrogel with a heterogenous structure with filamentary regions as well as network like regions. We observe pore like structures which in some cases were filled with other material, but also some less non-labeled areas/ pores. However, our observations regarding the structure of mucus in its hydrated state are far away from the previous electron microscopy network images. This discrepancy could be explained with the dynamic structure of mucus [11] that remains preserved in its hydrated state.

Previous studies have reported a size-dependent transport of particles and reported that particles < 200 nm could penetrate mucus [11,12,94]. This was related to the porous

structure of mucus and mesh size of mucus network. However, our findings are not consistent with this network model of mucus, as in this study we observed that in its hydrated state mucus does not possess a visualizable porous structure. On the other hand, Lai et al., (2007) reported a rapid transport of 500 nm muco-inert PEGylated nanoparticles, which does not correlate with the mesh size described in the electron microscopy studies 10-200 nm [72]. This study describes that such particles would diffuse through low viscosity channels of mucus. A similar finding was reported by Schuster et al., (2017), who showed a long-distance diffusion (ten or more micrometers) for nanoparticles < 200 nm, which was explained by interconnected domains [73]. In our CLSM images we similarly observe a composite-like structure of mucus characterized by voids filled with other materials as well as non-labeled voids, which might be filled with fluid, non-mucin constituents or other mucus constituents, and could serve as shortcut pathways promoting particles transport.

3.4. Conclusion

In the present study we demonstrate the influence of freezing, drying and freeze-drying on the structure of mucus and reveal the structural organization of hydrated mucus.

We found that despite cryo-fixation, the process of sublimation applied during Cryo-SEM analysis altered the structure of mucus and led to the formation of a porous structure. Whereas, in its hydrated state, mucus analyzed by ESEM showed a compact structure. STED microscopy allowed super-resolution visualization of MUC5B multimers, while CLSM analysis revealed the composite structure of mucus. Remarkably, in contrast to the conventional electron microscopy data, which described mucus as a porous network, visualization techniques, that do not require any dehydration step revealed rather a compact structure of mucus.

This study improves the understanding of the structure of hydrated mucus and introduces STED microscopy as a novel technique for investigation of mucus as well as mucus nanoparticle interactions.

3.5. Supplementary information

Supplementary Movie 3.1. Image sequence showing the impact of sublimation on the structure of native mucus. These images reveal the structural alteration of compact mucus into a porous network as a function of sublimation. A structural alteration of the formed pores and increase of porosity during the progression of the process of sublimation can be observed.

https://ars.els-cdn.com/content/image/1-s2.0-S0378517321000429-mmc2.mp4

Supplementary Movie 3.2. Image sequence showing the impact of freeze-drying on the structure of native mucus. These images reveal the structural alteration of compact mucus into a porous network as a function of solidification, precipitation, and sublimation of ice during time dependent temperature and pressure decrease. The formation of pores after precipitation and sublimation of ice under high vacuum conditions can be observed. https://ars.els-cdn.com/content/image/1-s2.0-S0378517321000429-mmc3.mp4

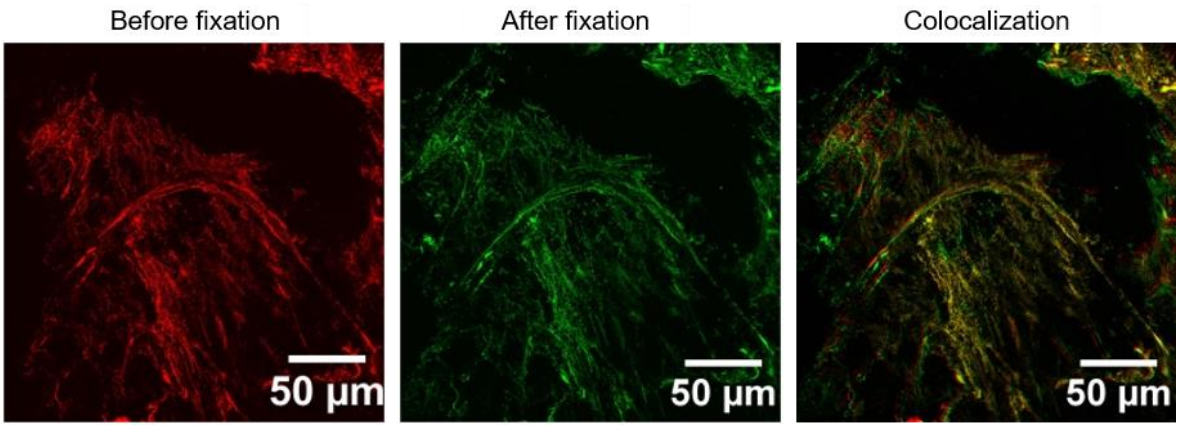

Supplementary Figure S3.1: Impact of the staining protocol on the structure of mucus regarding fixation. CLSM images of fresh mucus stained by WGA-Atto 647N before (red) and after (green) fixation by addition of 30 µl 4% PFA (same image section).

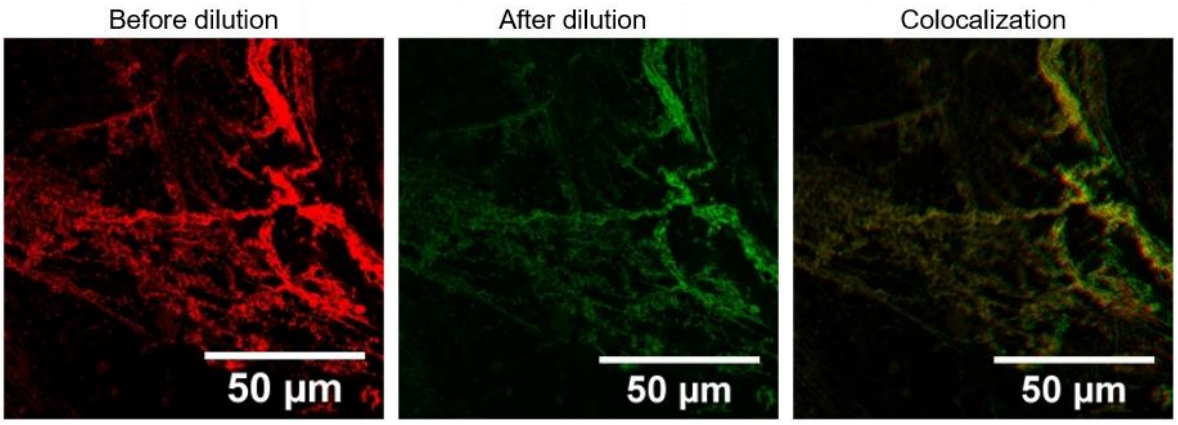

Supplementary Figure S3.2: Impact of the staining protocol on the structure of mucus regarding dilution. CLSM images of fresh mucus stained by WGA-Atto 647N before (red) and after (green) dilution by addition of 200 µl PBS (same image section).

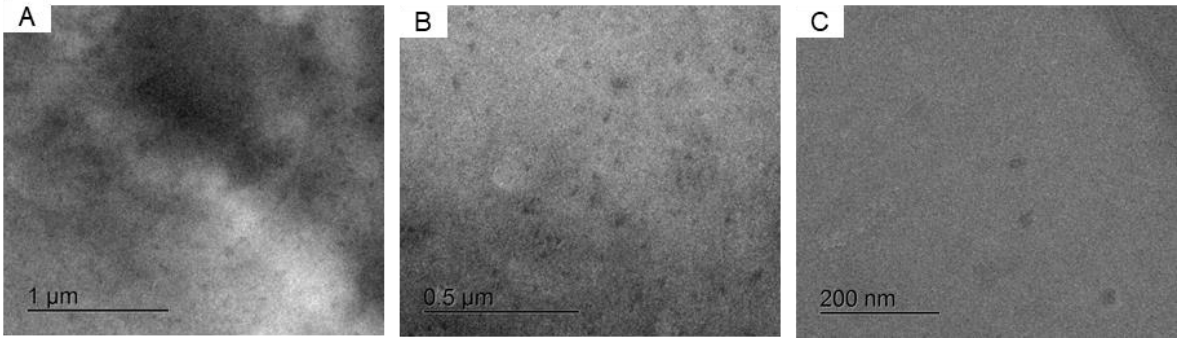

Supplementary Figure S3.3: Cryo-TEM micrographs of a thin layer of human pulmonary mucus. Samples were placed on a TEM grid and plunged into liquid ethane with a Gatan CP3 cryo-plunger (Gatan Inc., Pleasanton, CA, USA). Subsequently specimens were transferred to a Gatan 914 cryo-TEM holder (Gatan Inc., Pleasanton, CA, USA) and imaged. These micrographs show that preparation of thin mucus samples (several µm thick) allows imaging of mucus without ice crystals formation and confirm furthermore the non-porous structure of mucus.

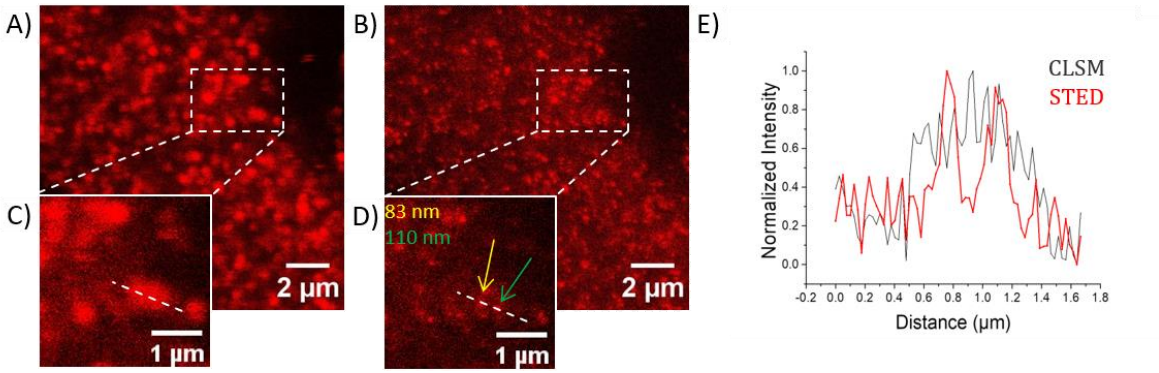

Supplementary Figure S3.4: STED microscopy reveals structural details (< 100 nm) of fresh pulmonary mucus. Samples were stained with primary anti-MUC5B antibody and secondary anti-mouse Atto 647N antibody. A) and B) show CLSM and STED images of the same region of mucus sample respectively. C) and D) represent enlargements of the marked regions in A and B respectively. E) Normalized intensity profiles along the dotted lines in C and D.

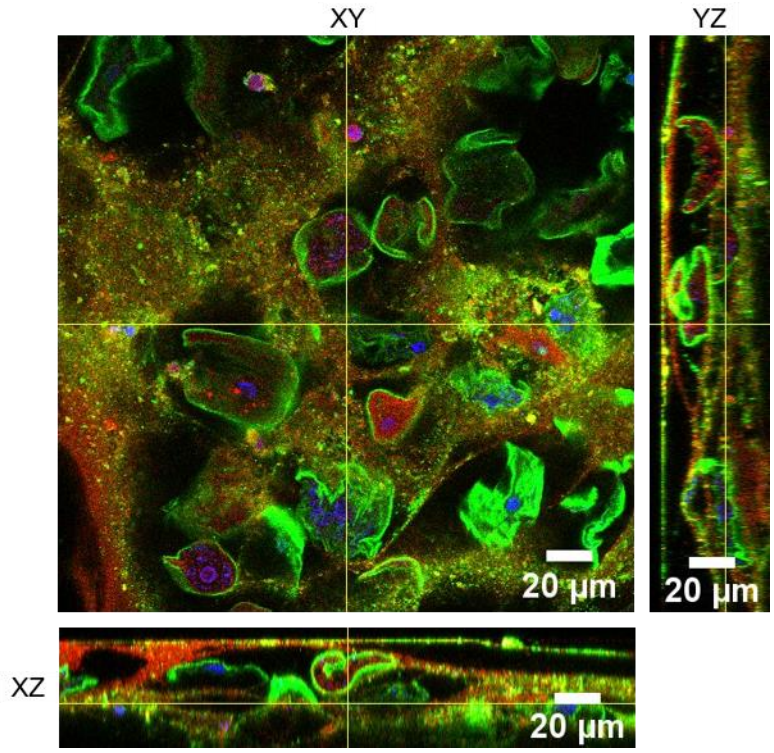

Supplementary Figure S3.5: Z-stack image of the composite structure of mucus. Samples were stained with anti-MUC5B-Atto 647N antibody (red), WGA-Alexa Fluor 488 (green) and Hoechst 33342 (blue).

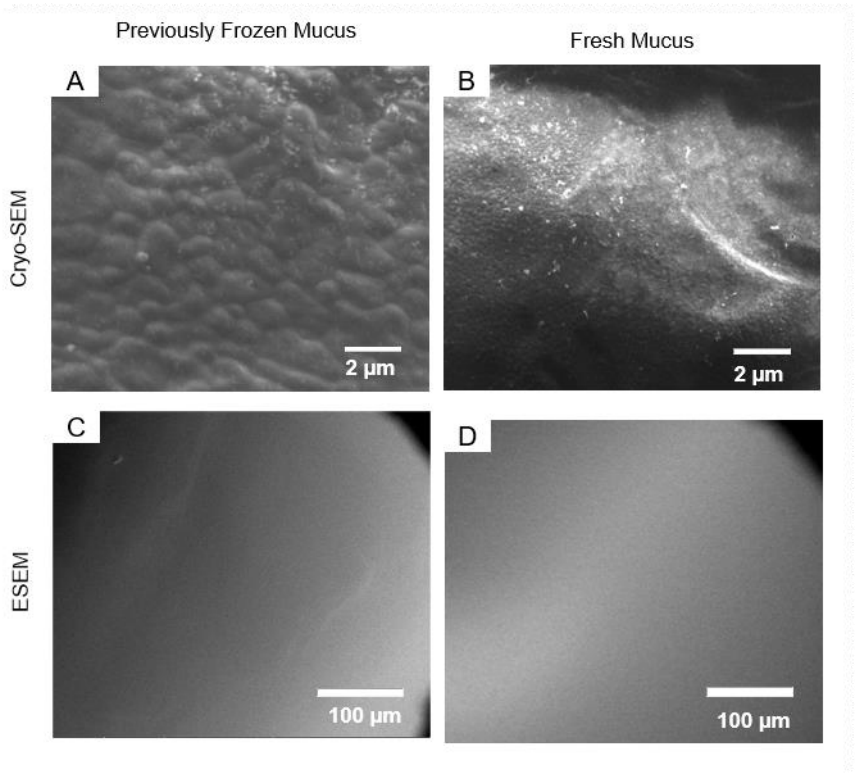

Supplementary Figure S3.6: Freezing showed no strong influence on the visualization of mucus performed by cryo-SEM and ESEM. A), B) non-porous structure of previously frozen (-80 °C) and freshly collected and refrigerated (4 °C) mucus visualized prior to sublimation by cryo-SEM. C), D) compact structure of previously frozen (-80 °C) and freshly collected and refrigerated (4 °C) mucus of an identical clinical sample analyzed in its hydrated state by ESEM.

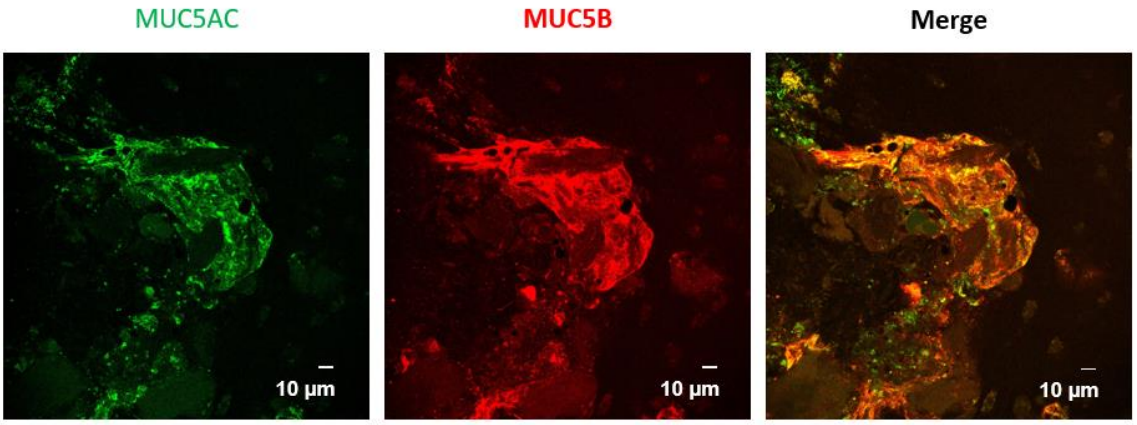

Supplementary Figure S3.7: CLSM images of mucus stained with anti-MUC5B-Atto 647N antibody (red), anti-MUC5AC-Fluor 488 (green).

4. Properties of Calu-3 *in vitro* mucus compared to *ex vivo* mucus

E. Meziu, S. K. Manier, S. Hemmer, A. Kraegeloh, M. Schneider planned this work. E.M. performed cell culture, mucus collection, light microscopy imaging, quantification of mucins, macrorheology, and 3D time lapse experiments. S.K.M., and S.H. carried out metabolomic analysis. E.M., S.K.M., A.K, M.S., contributed to data analysis.

4.1. Introduction

Human pulmonary mucus is a biological hydrogel, that hydrates, lubricates, and protects the underlying airway epithelium with a thickness varying from 2-5 to 10-30 µm at the bronchial and tracheal level respectively [95]. Mucus is produced from the submucosal glands and secretory goblet cells [1]. It is composed of water (95% w/v), mucin glycoproteins (2-5% w/v), non-mucin proteins, lipids, DNA, and salts [1,6]. Due to their unique molecular structure, mucins show intra- and intermolecular interactions granting mucus its viscoelastic and barrier properties [96]. Given its barrier properties, the mucus layer challenges the transport of drug carriers. For the investigation of mucus properties as well as for the development of efficient mucus penetrating drug delivery systems physiologically relevant mucus models are essential [23].

Ex vivo mucus gained by using the endotracheal tube (ETT) method from patients undergoing surgery under general anesthesia has been widely used in the development of drug delivery systems [29]. Some factors like interindividual variability, limited access, dehydration during intubation, as well as storage of samples in a frozen state due to high microbial susceptibility are the drawbacks of this mucus model [26,28,30,31]. The process of the collection of mucus involves several steps (*e.g.*, scratching of the endotracheal tube through trachea, centrifugation, and pipetting) that might compromise the properties of mucus. While this isolated type of mucus model allows the evaluation of the exclusive interaction of mucus with foreign entities, the cellular response is missing in this system. Furthermore, mucus producing Calu-3 cells cultured at air-interface conditions (AIC) represent an alternative model to close this gap. Calu-3 cells are widely used in various research fields and have been extensively investigated in terms of properties like tight junction formation, ion channel mechanism, and protein expression [97]. However, there is little information regarding the properties of mucus produced from these cells.

In this study, we investigated mucus produced by Calu-3 cell line as an *in vitro* mucus model, which allowed the evaluation of the mucus and cell layer interactions with applied materials. *In vitro* mucus produced from Calu-3 cells has been investigated in terms of mucins, macrorheology properties, mobility of carboxylated polystyrene particles (COOH-PS-Ps) through mucus, and metabolomic characteristics which were then compared to ETT *ex vivo* mucus. Such head-to-head comparison data should allow a better understanding regarding the applicability of Calu-3 *in vitro* mucus as a mucus model.

4.2. Materials and methods

4.2.1. Cell culture

Calu-3 (HTB-55^{TM}) epithelial cells were obtained from American Type Culture Collection (Rockville, MD, USA) and were used up to a passage number of 15. They were cultivated using minimum essential medium (Gibco Invitrogen, USA) supplemented with 10% fetal bovine serum (PAN-Biotech GmbH, Germany), 1% amino acids (Life Technologies, USA), and 1% sodium pyruvate (Life Technologies, USA). Calu-3 cells were incubated at 5% CO_2, 37 °C. Sub-cultivation was performed at a confluence of 80-90%. After reaching confluency, growth medium was removed, and cells were washed with pre-warmed Dulbecco`s phosphate buffered saline (DPBS) (Sigma-Aldrich, Germany). Subsequently, cells were trypsinized by adding pre-warmed 0.05% trypsin (containing 0.02% EDTA) (PAN Biotech, Germany) and were incubated for 20 min. Cells were seeded in a 12-well Transwell® plate (Greiner Bio-One GmbH, Germany) with a pore size of 0.4 µm and an insert diameter of 1.12 cm^2 at a density of 10^5 cells/cm^2. For the first 24 h, cells were grown in liquid-covered culture (LCC) containing 1 ml medium in the basolateral compartment and 500 µl medium in the apical compartment. After 24 h, cells were differentiated at AIC conditions for 21 days.

4.2.2. Mucus sample collection

In vitro mucus: Calu-3 cells were grown for 21 days under AIC conditions. The mucus formed in the apical compartment was loosened to enable pipetting and collected by addition of 50 µl of DPBS in the apical compartment of the transwell filters. Added DPBS was withdrawn after 30 min incubation at 37 °C. Mucus samples were then harvested using a

positive displacement pipette.

Ex vivo mucus: Samples of human respiratory mucus were collected using the ETT method as previously reported [29]. Briefly, the distal part of the tracheal tubes of patients undergoing intubation during a surgery was cut and centrifugated in a falcon tube. Subsequently, mucus was collected with a positive displacement pipette.

4.2.3. Visualization of mucins

Preparation of the cell samples: Samples were fixed for 30 min using 4% (v/v) paraformaldehyde (Electron microscopy science, Hatfield, UK) and permeabilized with 0.2% Triton-X 100 solution (Carl Roth, Karlsruhe, Germany) for 30 min. Afterwards, samples were blocked with 5% (w/v) bovine serum albumin (Carl Roth, Karlsruhe, Germany) for 30 min.

Fluorescence staining of the samples: Staining of the samples was performed as previously reported [13,98]. For MUC5B staining, samples were incubated with 2 µg/ml mouse anti-MUC5B primary antibody (Thermo Fisher Scientific, Rockford, USA) for 1 h at room temperature (RT) and 10 µg/ml Atto 647N conjugated anti-mouse secondary antibody (Sigma Aldrich, Siegen, Germany) for 1 h at RT. For MUC5AC staining, samples were stained using 2 µg/ml rabbit anti-MUC5AC primary antibody (antibodies-online GmbH, Aachen, Germany) for 1 h at RT and 10 µg/ml Alexa Fluor 488 conjugated anti-rabbit secondary antibody (Sigma Aldrich, Steinheim Germany) for 1 h at 4 °C. Between each step, the samples were washed three times with DPBS.

Imaging of the samples: Samples were visualized using a TCS-SP5 STED setup (Leica Microsystems, Mannheim, Germany). The fluorescent dyes Alexa 488 and Atto 647N were excited using an argon laser (λ = 488 nm) and a HeNe laser (λ = 633 nm) respectively.

4.2.4. Quantification of mucins

Quantification of the mucin content of the samples is performed as described by M. Kilcoyne et al., (2011) using the Periodic Acid-Schiff (PAS) assay [99]. 25 µl of collected mucus was mixed with 120 µl of freshly prepared solution of 0.06% periodic acid (Carl Roth, Karlsruhe, Germany) in 7% acetic acid (Carl Roth, Karlsruhe, Germany) and incubated at 37 °C for 1.5 h in a plastic sealed microplate. The prepared mixture was cooled down to RT. Subsequently, 100 µl of Schiff's reagent (Carl Roth, Karlsruhe, Germany) was added. The

prepared mixture was shaken for 5 min and incubated for 40 min at RT. The absorbance was read at 550 nm using a Spectramax microplate reader (Molecular Devices, CA, USA).

4.2.5. Macrorheology measurements

Macrorheology measurements were performed using a DHRIII Rheometer (TA Instruments, New Castle, DE, USA) with parallel plate geometry (diameter 12 mm). A volume of 30 µl mucus was used for the measurements. Silicon oil was applied to the edges to avoid sample dehydration. Measurements were carried out at 25 °C in triplicates. Loss modulus (G") and storage modulus (G') were measured, using frequency sweep measurements at an angular frequency of (ω) 1−5 rad/s and a shear strain of (γ) = 1%.

4.2.6. Particle penetration analysis

Staining of the samples: Mucus samples were stained with wheat germ agglutinin-tetramethyl Rhodamine (WGA-Rhod) (Vector Laboratories Inc., Newark, CA, USA). Calu-3 *in vitro* mucus samples were stained with 100 µg/ml WGA-Rhod for 2 h at 37 °C as previously described [98]. Samples were stained from the basolateral compartment. *Ex vivo* mucus samples were stained with 100 µg/ml WGA-Rhod for 1 h at RT.

Exposure of samples to particles: Samples were exposed to particles as previously reported [98]. Diameter and zeta potential of particles were measured using Zetasizer NanoZSP instrument (Malvern Instruments, Worcestershire, UK) (Table 4.1). 200 µl of 100 nm (10 µg/ml), 200 nm (50 µg/ml), and 500 nm (1 mg/ml) dragon green-labeled COOH-PS-Ps (Bangs Laboratories, Fisher Scientific, USA) were applied to the samples using the Vitrocell® Cloud 6 system (VITROCELL Systems GmbH, Waldkirch, Germany). Subsequently, samples were incubated for 3 h at 37 °C.

Table 4.1: Physicochemical properties of particles used in this study.

PS-NPs	Labeling	Hydrodynamic diameter [nm]	Zeta potential [mV]
100 nm COOH-PS-NPs	dragon green	96 ± 19 nm	-49
200 nm COOH-PS-NPs	dragon green	183 ± 44 nm	-51
500 nm COOH-PS-Ps	dragon green	452 ± 99 nm	-57

Confocal laser scanning microscopy: The same microscopy setup as described in 4.2.3 was used. The fluorescent dyes Dragon Green and Rhodamine were excited using an argon laser (λ = 488 nm) and a DPSS laser (λ = 561 nm), respectively. For the analysis of particle penetration, z-stacks (step size 1 µm) of the samples were acquired.

Image processing: Due to their low concentration, for the evaluation of the penetration of 100 and 200 nm carboxyl-modified polystyrene nanoparticles (COOH-PS-NPs) the number or particles (N) in the obtained z-stacks could be estimated as described by Labouta et al. 2011 [100]. The sum of the pixels (Σ Pixel) of the detected particles was determined for each z-stack. Using the area of one pixel (A pixel) and the single diffraction-limited area of the particles (A particle), the number of particles was calculated according to the equation below:

$$N = \frac{\Sigma\, Pixel + \mathrm{A\ pixel}}{A\ particle}$$

For the evaluation of the penetration of 500 nm COOH-PS-Ps, the raw fluorescence intensity of the particle signals in the acquired z-stacks was quantified using Image J software, version 1.53e, as previously reported [98].

4.2.7. Metabolite analysis

Sample preparation: To reduce the viscosity and enable an easier handling in terms of pipetting, mucus samples (16 *in vitro* and 37 *ex vivo*) were mixed with 10% NAC (1:1 dilution). Samples were then prepared as described by Hemmer et al., (2021) [101]. In brief, 200 µl of a methanol ethanol mixture (1:1, v/v) was added to 50 µl mucus. Samples were then vortexed and centrifuged. 150 µl of the supernatant was dried and then reconstituted in 50 µl of a mixture of acetonitrile and methanol (70:30, v/v).

LC-HRMS/MS apparatus: Analysis was performed as previously described by Manier et al., (2020) [102]. Briefly, a Dionex UltiMate 3000 RS pump coupled to a TF Q-Exactive Plus system (Thermo Fisher Scientific, Dreieich, Germany) was used. Reversed-phase chromatography was performed on a TF Accucore Phenyl-Hexyl column (100 mm × 2.1 mm, 2.6 µm) (Thermo Fisher Scientific, Dreieich, Germany). Normal phase chromatography was performed on a Nucleodur hydrophilic interaction liquid chromatography (HILIC) column (125 × 3 mm, 3 µm) (Macherey–Nagel, Düren, Germany). The scan range was *m/z* 50–750; polarity, negative or positive; spectrum data type,

centroid. TF X calibur software version 3.0.63 was used.

Data processing: Processing of the data was performed as previously described by Manier et al., (2020) [102]. For the statistical analysis of the data obtained from *in vitro* and *ex vivo* mucus samples, a Welch *t*-test in combination with a fold change evaluation was applied. The differences between the models were visualized by using the volcano plots, which reveal the results of the *t*-test (*p*-values) and fold change for the metabolites of both models. The assumed significance level α was corrected using the Bonferroni correction to minimize the false positive results that might occur by multiple *t*-tests (α of 0.001 divided by the number of features recorded in total). Each point in the volcano plot represents a metabolite and is characterized by its *m/z* and retention time. For example, "M452T472" means: Recorded at *m/z* = 452 and retention time 472 s. Principal component analysis (PCA) was used to reduce the data set from 53 (samples) x 3000 (features) to 53 x 1 by using PC1 (linear combination of original variables representing the most variation in the data) and PC2 (linear combination of original variables representing the second most variation in the data). Linear discriminant analysis (LDA) was used for the categorization of the data in groups. The accuracy of the distribution of the data in clusters was calculated using the Cohen's κ value, which is a statistical measure of interrater reliability and accuracy. Differently from simple percent agreement calculations, Cohen's κ takes into consideration also the possibility of the agreement occurring by chance. Cohen's *κ* value was evaluated as reported by Landis and Koch [103].

4.3. Results

4.3.1. Visualization of mucins of *in vitro* and *ex vivo* mucus

Mucus is composed of water, mucin glycoproteins, non-mucin proteins, lipids, DNA, salts, cells, and cell debris [1]. Mucin glycoproteins, particularly MUC5AC and MUC5B (major gel-forming mucins in airways) are responsible for the essential properties of mucus like rheology, protection, and clearance [18,21,41]. Therefore, in this study we investigated the presence of MUC5AC and MUC5B in *vitro* and *ex vivo* mucus models.

CLSM images show the presence of MUC5B and MUC5AC in *in vitro* mucus (extracellular mucus layer of Calu-3 cells) and *ex vivo* mucus (Figure 4.1 A-F), which is in accordance with previous reports [13,98]. E*x vivo* mucus shows a high degree of colocalization of MUC5B

and MUC5AC (Figure 4.1 A-C), whereas in *in vitro* mucus, MUC5B and MUC5AC were predominant in different regions and showed less signal colocalization (Figure 4.1 D-F).

The tracheal segments of pigs, which allowed the visualization of mucus lining the epithelium without involving any mucus collection procedure revealed a distinct mucin distribution for MUC5B and MUC5AC [86]. The high degree of colocalization of MUC5B and MUC5AC in *ex vivo* mucus might be explained by the applied mucus collection procedure, which involves steps like pulling out of the endotracheal tube during patient extubation, and centrifugation of the cut endotracheal tube at 10.000 g for 10 min. In contrast to *ex vivo* mucus, Calu-3 *in vitro* mucus is an undisturbed system. This might be the reason for the distinct MUC5B and MUC5AC patterns observed in Calu-3 samples.

Both mucus models reveal the presence of the major gel-forming mucins of human pulmonary mucus MUC5AC and MUC5B, which are responsible for essential properties of mucus. The CLSM images might indicate a disturbed morphology of *ex vivo* mucus samples. These data suggest that mucin morphology of human airway mucus is a property which needs to be further investigated. Bronchoscopy samples might represent an alternative mucus model for a more realistic elucidation of the mucin morphology of human airways.

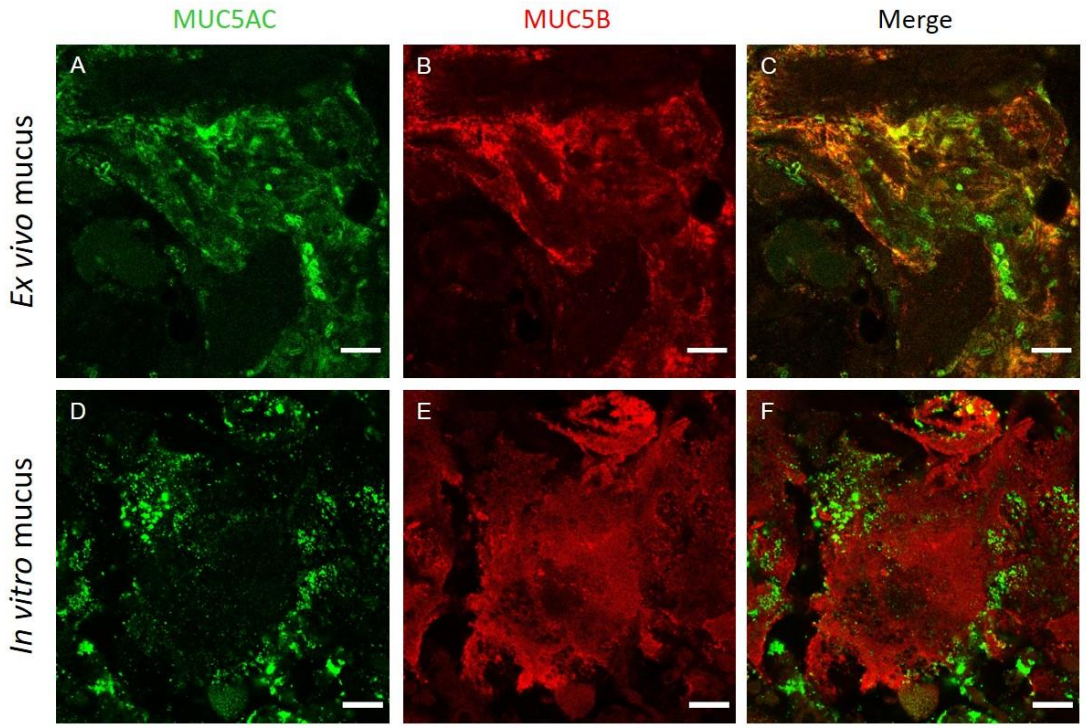

Figure 4.1: MUC5AC and MUC5B in *in vitro* and *ex vivo* mucus. A-B) CLSM images reveal the presence of both major gel-forming mucins MUC5AC and MUC5B in *ex vivo* mucus samples. C) Both mucins show a large mass of colocalization in the merged image of *ex vivo* mucus. D-E) Calu-3 cells cultured under AIC conditions secrete both MUC5AC and MUC5B. F) Differently from *ex vivo* mucus, *in vitro* mucus samples show less colocalization of MUC5AC and MUC5B. Scale bar 10 µm.

4.3.2. Quantification of mucins of *in vitro* and *ex vivo* mucus

Mucin glycoproteins confer mucus its mucociliary clearance and barrier functions [18]. Therefore, the information about the mucin concentration is noteworthy in terms of the use of these mucus models.

Mucin concentration in *in vitro* mucus was lower (4.58%) than that of *ex vivo* mucus (6.75%) (Figure 4.2). Previous studies have reported a mucin concentration of 2-5% of human airway mucus [6]. The mucin concentration observed in the *ex vivo* mucus is slightly out of the physiological range of healthy mucus. This might be explained by evaporative water loss that can occur during the process of patient intubation [26]. The process of mucus harvesting, which includes DPBS addition to the apical compartment of Calu-3 transwells, might also influence the mucin concentration of *in vitro* mucus.

Mucin concentration is a pertinent parameter regarding the barrier properties of mucus [18]. Therefore, further barrier relevant parameters like rheological behavior for both mucus models were investigated.

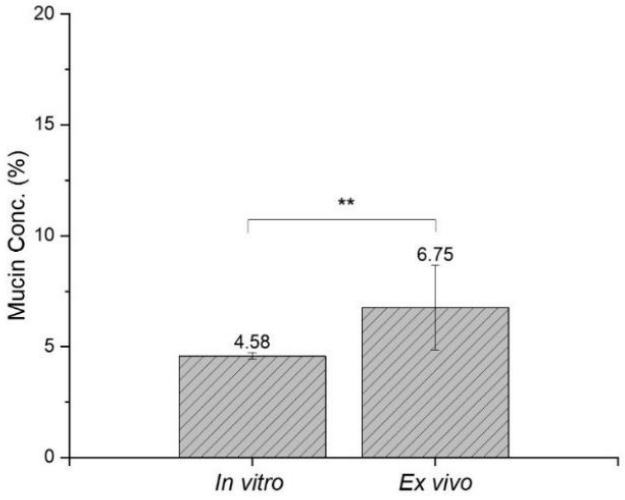

Figure 4.2: Mucin concentration in *in vitro* and *ex vivo* mucus quantified via PAS assay. Data shown are mean values ± SE for $n = 9$ technical replicates from 3 samples. Statistical significance was calculated with One Way ANOVA followed by the Bonferroni test and indicated by asterisks: **, $p < 0.01$.

4.3.3. Macrorheology of *in vitro* and *ex vivo* mucus

Rheological behavior of mucus is essential for the barrier function of mucus and thus for mucus nanoparticle interaction studies [68,104]. Therefore, rheological measurements were performed to determine whether *in vitro* and *ex vivo* mucus exhibit similar rheological behavior.

Both mucus models showed an elastic dominant behavior with storage modulus G' in excess over loss modulus G" (Figure 4.3), which is a typical rheological property for crosslinked polymers [105,106]. The rheology profiles indicate a viscoelastic hydrogel behavior for both *in vitro* and *ex vivo* mucus models, which is in accordance with previous rheological characterizations of *ex vivo* mucus [38]. The macrorheological properties of Calu-3 mucus have, as far as we know, previously not been reported. The loss and storage modulus values of *in vitro* mucus were lower than those of *ex vivo* mucus. Considering the impact of mucin concentration on the rheology properties of mucus, this difference

correlates well with the mucin concentration values reported above. It should be noted, that similar to mucin concentration, the macrorheology of mucus might also be influenced by the dehydration of *ex vivo* mucus during the process of patient intubation [26] or by the possible dilution of *in vitro* mucus during the process of harvesting. Furthermore, mucus is a highly heterogenous material which has been described to exhibit viscoelastic gel properties at the macroscale level and low viscosity fluid properties at the microscale level [6]. Therefore, the investigation of the transport of particles through *in vitro* and *ex vivo* mucus is important in order to assess the impact of the observed differences (mucin concentration and loss and storage moduli values) on the barrier properties of mucus.

To this end, these data provide evidence that *in vitro* mucus harvested from Calu-3 cells exhibits viscoelastic hydrogel properties but overall with lower loss and storage moduli values than the *ex vivo* mucus model.

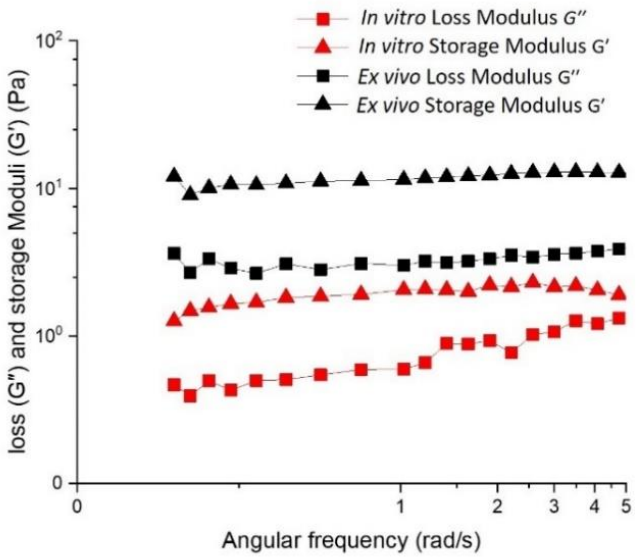

Figure 4.3: Rheological properties of *in vitro* and *ex vivo* mucus. Loss (G'') and storage moduli (G') for *in vitro* and *ex vivo* mucus, 25 °C. The results show the mean for $n = 9$ technical replicates from 3 samples.

4.3.4. Particle penetration through *in vitro* and *ex vivo* mucus

Understanding the rate and extent of particle transport through mucus is of fundamental interest for the validity and selection of the mucus model, as well as for the data interpretation for mucus studies in the field of drug delivery. Therefore, the penetration of

100, 200, and 500 nm COOH-PS-Ps through *in vitro* and *ex vivo* mucus was investigated.

The diffusion of particles in *in vitro* and *ex vivo* mucus was analyzed using CLSM imaging. After 3h incubation time, z -stacks (step size 1 µm) were acquired starting from the top of the mucus layer down to deeper layers (25 µm). The presence of particles in different depths (individual optical layers) of mucus was quantified by estimating the number of particles for the 100 and 200 nm COOH-PS-NPs and by measuring the fluorescence intensity of the particle signals for the 500 nm COOH-PS-Ps. For this analysis, it was crucial to ensure that the measurements were performed within the mucus layer. WGA-Rhod staining allowed a morphological differentiation between the cell and mucus layer [98]. In order to avoid mucus dilution, staining was performed from the basolateral compartment.

100 and 200 nm COOH-PS-NPs showed a similar penetration for both mucus models with a decreasing number of particles starting from the top layer to the down layers of mucus (Figure 4.4 A, B). Fluorescence intensity of the 500 nm COOH-PS-Ps signals was highest at the uppermost layer of the sample and decreased with the increasing distance from the top of the sample (Figure 4.5). Particles were detected at 5 µm and 10 µm, while to the depth of 15 µm only a negligible particle penetration was observed (Supplementary information Figure S4.1). Both *in vitro* and *ex vivo* mucus showed a strong exclusion of 500 nm COOH-PS-Ps, which is in complement with previous reports [12,38,98]. A similar transport profile of 500 nm COOH-PS-Ps through mucus layers was observed for *in vitro* and *ex vivo* mucus.

These data accentuate the barrier capacity of *in vitro* mucus which reveals barrier properties similar to that of *ex vivo* mucus. In contrast to mucin concentration and rheology data which exhibited differences between both mucus models, particle penetration analysis showed a similar particle transport profile for *in vitro* and *ex vivo* mucus. This might indicate that this scale of rheological differences does not influence the barrier properties of *in vitro* and *ex vivo* mucus. Another point which might also explain this discrepancy is that for mucin concentration and rheology experiments *in vitro* mucus was harvested from Calu-3 cells, while particle penetration analysis was performed on undisturbed mucus lining Calu-3 cells. These data demonstrate the barrier properties of *in vitro* mucus, indicating the suitability of this model for mucus penetration studies.

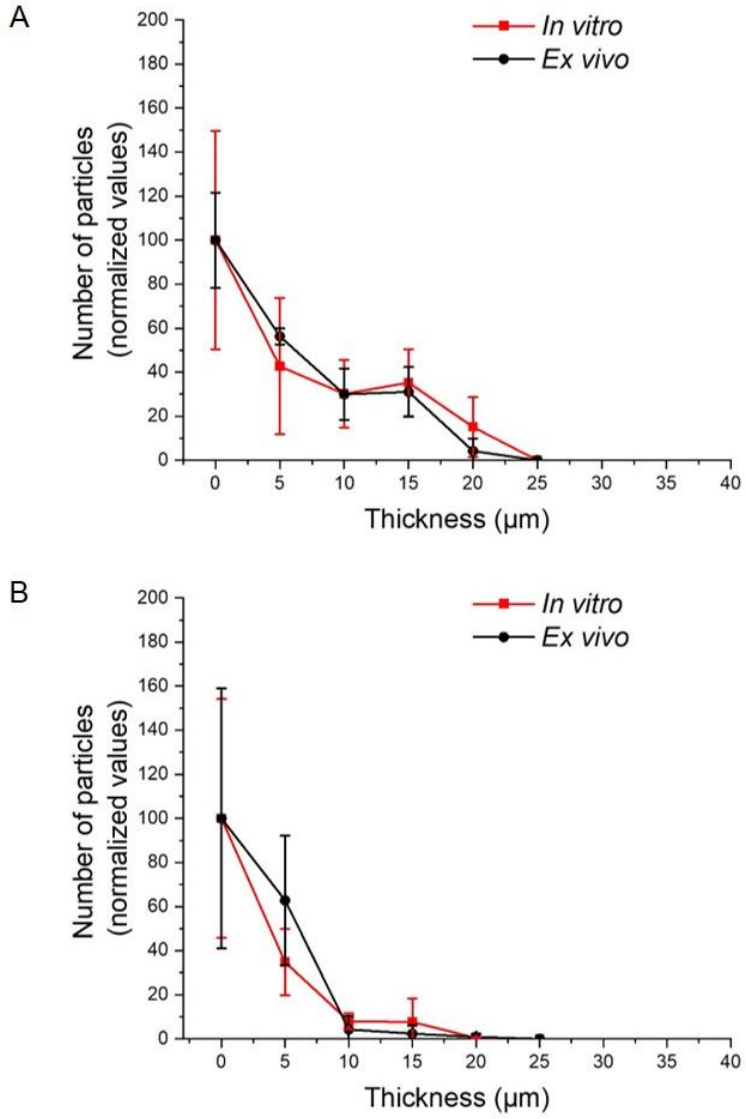

Figure 4.4: Quantitative analysis of the penetration of A) 100 nm and B) 200 nm COOH-PS-NPs through *in vitro* and *ex vivo* mucus. Data shown are mean values ± SE for n = 3 sample areas from 3 samples.

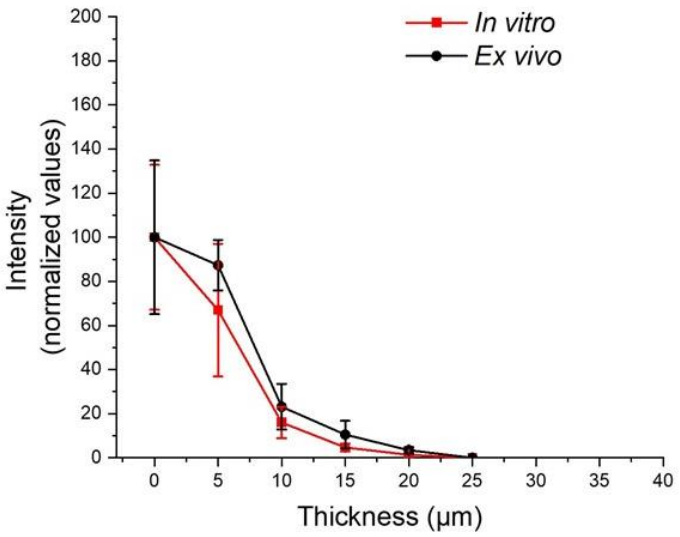

Figure 4.5: Quantitative analysis of the penetration of 500 nm COOH-PS-Ps through *in vitro* and *ex vivo* mucus. Data shown are mean values ± SE for n = 3 sample areas from 3 samples.

4.3.5. Metabolomic analysis of *in vitro* and *ex vivo* mucus

Metabolomics involves profiling of metabolites (cell metabolism products) within a biological matrix. Metabolomic studies are classified as untargeted (measurement of all metabolites) and targeted (measurement of previously characterized metabolites) [107].

Human pulmonary mucus might contain metabolites of various origin, *e.g.*, metabolites secreted or excreted by the underlying epithelia, molecules derived from mucin degradation due to the presence of proteolytic enzymes, or from bacteria present in mucus [33,108–110]. It might also contain other small molecules originating from sample preparation steps (*e.g.*, mucin fragmentation due to centrifugation steps).

Mucus has been characterized mostly in terms of composition, structural organization, rheology, and barrier properties. However, few studies have investigated metabolic patterns of mucus. Metabolome analyses provide information about the metabolic pathways, the etiopathology, and thus the casual therapy of diseases (*e.g.*, chronic obstructive pulmonary disease and cystic fibrosis) [108,109]. In addition, metabolome analyses provide indirect information about the composition of mucus. In this context investigation of metabolites in mucus as a biological matrix is essential in terms of sample characterization and comparison. Therefore, in this study we applied untargeted metabolomic analysis to explore the differences in the metabolomic profiles of Calu-3

in vitro and ETT *ex vivo* mucus.

This study focuses on the detection of small molecules in mucus using a narrow scan range of *m/z* of 50-750. Considering this fact, this study provides information about small molecule metabolites and indirect information about the composition of mucus. The normal- and reversed-phase HPLC has been employed for the detection of the polar and non-polar compounds respectively. Depending on physicochemical properties, compounds have been detected using positive and negative ionization modes [111].

The analytical differences between the two models were visualized using Volcano plot (Figure 4.6). Volcano plot of samples measured using a Phenyl-Hexyl column - positive mode (Figure 4.6) shows that the amount of the significant features (red points) was large. At the same time, it can be seen from the fold change (x-axis) that most of the features showed a lower signal in the *in vitro* group. Similar results could be observed for the measurements using HILIC - positive mode, Phenyl-Hexyl column - negative mode and HILIC - negative mode (Supplementary information Figure S4.2).

The obtained data were evaluated using PCA followed by LDA (Figure 4.7). The score plot of samples measured using Phenyl-Hexyl column - positive mode shows clearly separated clusters indicating that the *in vitro* mucus group is separated from the *ex vivo* mucus group (Figure 4.7). *In vitro* samples clustered at the right part and *ex vivo* samples clustered at the left part of the graph. These data present the differences between *in vitro* and *ex vivo* mucus in terms of their metabolomic profile. The quality control samples (a mixture of all the 16 *in vitro* and 37 *ex vivo* extracts) are classified in the *ex vivo* samples. This was expectable as the *ex vivo* samples were dominant in the mixture of quality control samples as compared to the *in vitro* ones. According to the calculated Cohen's κ value the distribution on the cluster was 90% correct, which is almost perfect according to Landis and Koch (1977) [103]. Similar results could be observed also for the measurements using HILIC - positive mode, Phenyl-Hexyl column - negative mode and HILIC - negative mode (Supplementary information Figure S4.3).

The graph of the loadings of PC-LDA (Figure 4.8) reveals which features were responsible for the split of the clusters in the Figure 4.7. The most important 8 features are annotated. The graphs of the loadings of the measurements using HILIC - positive mode, Phenyl-Hexyl column negative mode and HILIC - negative mode are presented in the Supplementary information Figure S4.4.

From the features, which were selected as responsible for the split of the clusters only 9 could be identified (Table 4.2). This rather poor rate of identification represents the drawback of the untargeted metabolomics, as reference spectra do not exist for all endogenous substances. Peptide fragments were found to be highly significant in terms of the difference between *in vitro* and *ex vivo* mucus models. The detected peptide sequences (Pro-Pro-Pro and Pro-Leu) are part of the major gel-forming mucins MUC5AC and MUC5B. These peptide fragments might be created during the processing of the samples (especially during vortexing). The higher amount of peptide sequences in *ex vivo* mucus might be due to a more intensive sample preparation procedure (including a centrifugation step at 10.000 *g* for 10 min) during the collection of *ex vivo* mucus in comparison to that of *in vitro* mucus and/or due to a higher mucin content in *ex vivo* mucus. Furthermore, it can clearly be seen that there is a pronounced difference in the composition of the lipids with a higher amount of lipids in the *ex vivo* samples. Mucus lipids include cholesterol, fatty acids, phospholipids [68]. From the features that could be identified, a strong difference was observed for fatty acids, N-acyl ethanolamines (fatty amides), phosphaditylethanolamines (phospholipids). This dissimilarity could be due to the lower metabolic activity of Calu-3 cells. Another reason for this difference might be the presence of surfactant with a lipid content of 90% in *ex vivo* mucus, which is lacking in Calu-3 cells [112,113].

Collectively, the data presented in this study show the existence of significant differences between the metabolomic profiles of Calu-3 *in vitro* mucus and *ex vivo* mucus. These data also point to the differences in the composition (in terms of lipid and mucin content) of both mucus models (Table 4.2), which is of relevance regarding the use of the models. To the best of our knowledge, this is the first time that the metabolomic profiles of Calu-3 *in vitro* mucus and ETT *ex vivo* mucus have been analyzed and compared.

Figure 4.6: Volcano plot showing the statistical untargeted metabolomics comparison between *in vitro* and *ex vivo* mucus. The y-axis corresponds to the -log 10 of *t*-test statistical *p*-value and x-axis corresponds to the log2 fold change (*ex vivo* mucus/ *in vitro* mucus). Each point in the figure is characterized by its *m/z* and retention time. The values with a fold change < 0.1 and > 10 and a Bonferroni corrected *p*-value < 0.001 were classified as significant and highlighted in red. Data shown are obtained from *n* tot = 53 samples; *n ex vivo* mucus = 37, *n in vitro* mucus = 16. Phenyl-Hexyl column and positive mode was used.

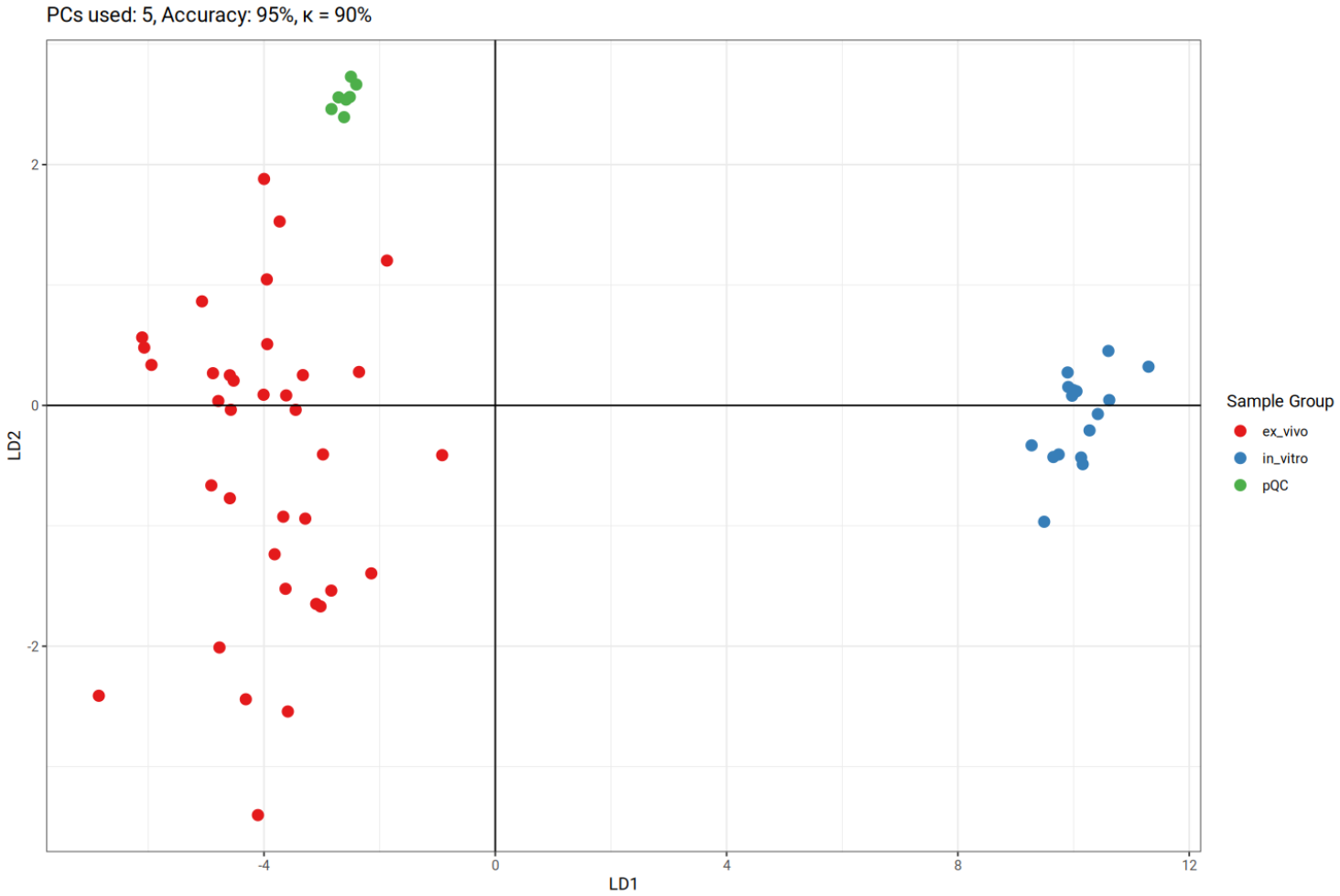

Figure 4.7: Scores of principal component linear discriminant analysis (PC-LDA) for *in vitro* and *ex vivo* mucus. The number of principal components used, the prediction accuracy, and Cohen's κ is given. Phenyl-Hexyl column and positive mode was used.

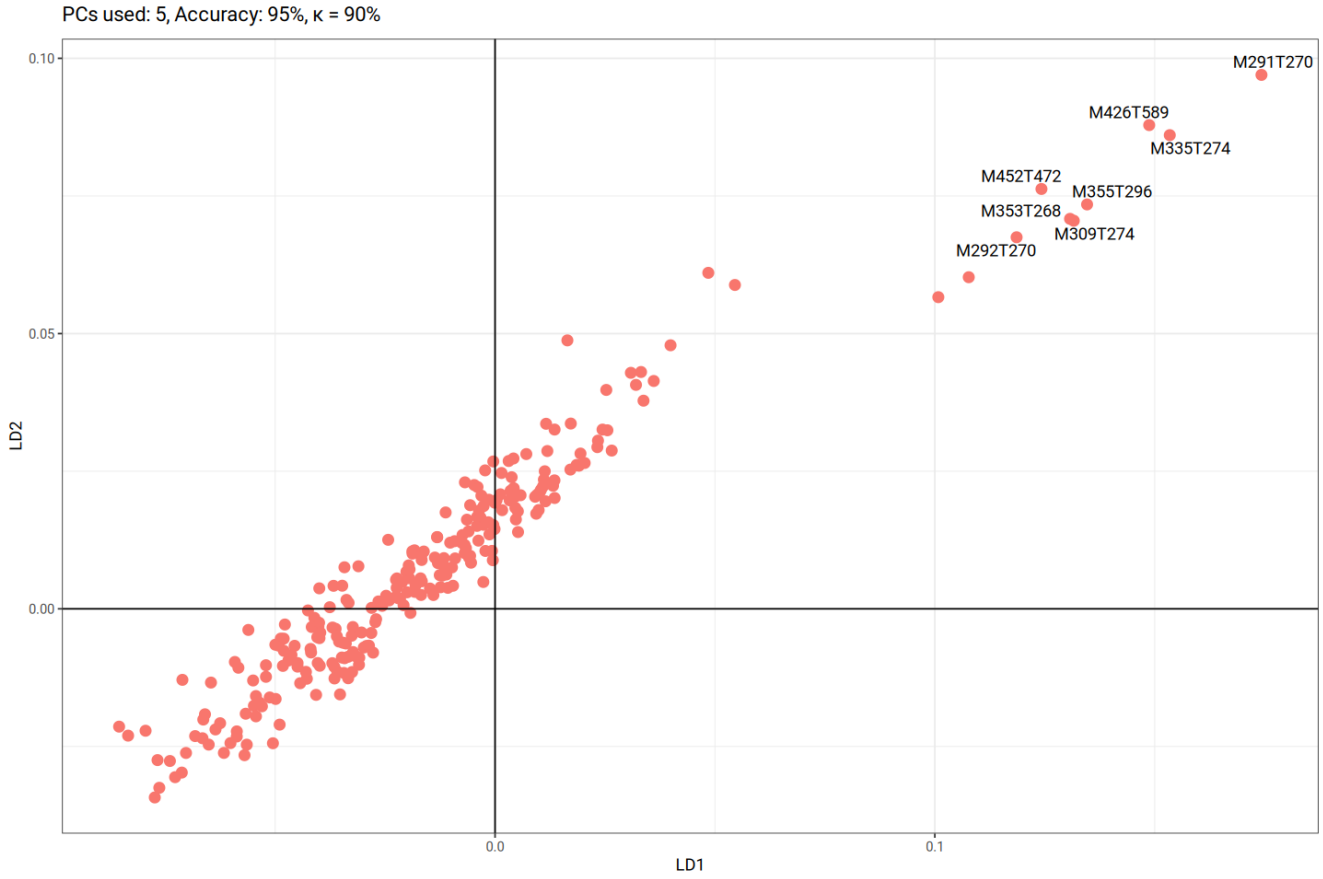

Figure 4.8: Loadings of principal component - linear discriminant analysis (PC-LDA) for *in vitro* and *ex vivo* mucus. The most important features are annotated. The number of principal components used, the prediction accuracy, and Cohen's κ is given. Phenyl-Hexyl column and positive mode was used.

Table 4.2: Classification and fold change of the features that could be identified with parallel reaction monitoring.

Compound	Class	Fold Change (ex vivo / in vitro)
9-Oxo-10E,12Z-octadecadienoic acid	Fatty Acid	3.714
13-Keto-9Z,11E-octadecadienoic acid	Fatty Acid	16.741
5,8,12-Trihydroxy-9-octadecenoic acid	Fatty Acid	8.869
LPA O-19:5	Lipid	60
PE(0:0/16:1(9Z))	Phosphaditylethanolamine	368
NAE 26:7	*N*-acyl ethanolamines	7.290
PE(P-16:0/16:1(9Z))	Phosphaditylethanolamine	441
Pro-Pro-Pro-X	Peptide	20.986
Pro-Leu-X	Peptide	5.708

4.4. Conclusion

The selection of the ideal mucus model often comprises a thorough assessment of advantages and disadvantages of the mucus models in question. Therefore, the availability of characterization data of mucus models is essential. Calu-3 cells have been widely used in mucus research. However little information is available regarding the properties of the mucus layer produced by Calu-3 cells. We investigated Calu-3 *in vitro* mucus and compared it to the human pulmonary ETT *ex vivo* mucus, a well-known standard mucus model, despite various drawbacks.

In vitro mucus showed a morphologically less disturbed model. Mucin concentration was lower for *in vitro* mucus. Similar to *ex vivo* mucus *in vitro* mucus showed a viscoelastic hydrogel behavior, with however lower loss and storage moduli values. Despite the differences regarding the mucin concentration and storage and loss values, the barrier properties of *in vitro* mucus were similar to that of *ex vivo* mucus. In terms of the metabolomic profile, *in vitro* mucus differed significantly from *ex vivo* mucus. The non-targeted metabolomic data demonstrated that most of the features showed a lower signal for *in vitro* mucus. Considering the features that could be identified, it could be observed that the difference between both models was in particular pronounced for the mucin and lipid content. These differences might be related to higher mucin concentration, intensive sample preparation resulting in the mucin fragmentation, and the presence of surfactant in *ex vivo* mucus.

The data provided in this study indicate that, Calu-3 *in vitro* mucus represents a valuable mucus model in particular for studies taking into consideration the evaluation of endpoints like mucus morphology or mucus particle penetration. Considering the lower metabolite values and the absence of surfactant, Calu-3 mucus might be a simpler mucus model with a lower metabolic activity. The findings provided here provide valuable information for the use of the Calu-3 cell line as a platform to perform preliminary metabolomic studies.

This study improves the knowledge about Calu-3 *in vitro* mucus and suggests that the properties of Calu-3 *in vitro* mucus need to be taken into consideration for the right interpretation of the data obtained using this model.

4.5. Supplementary information

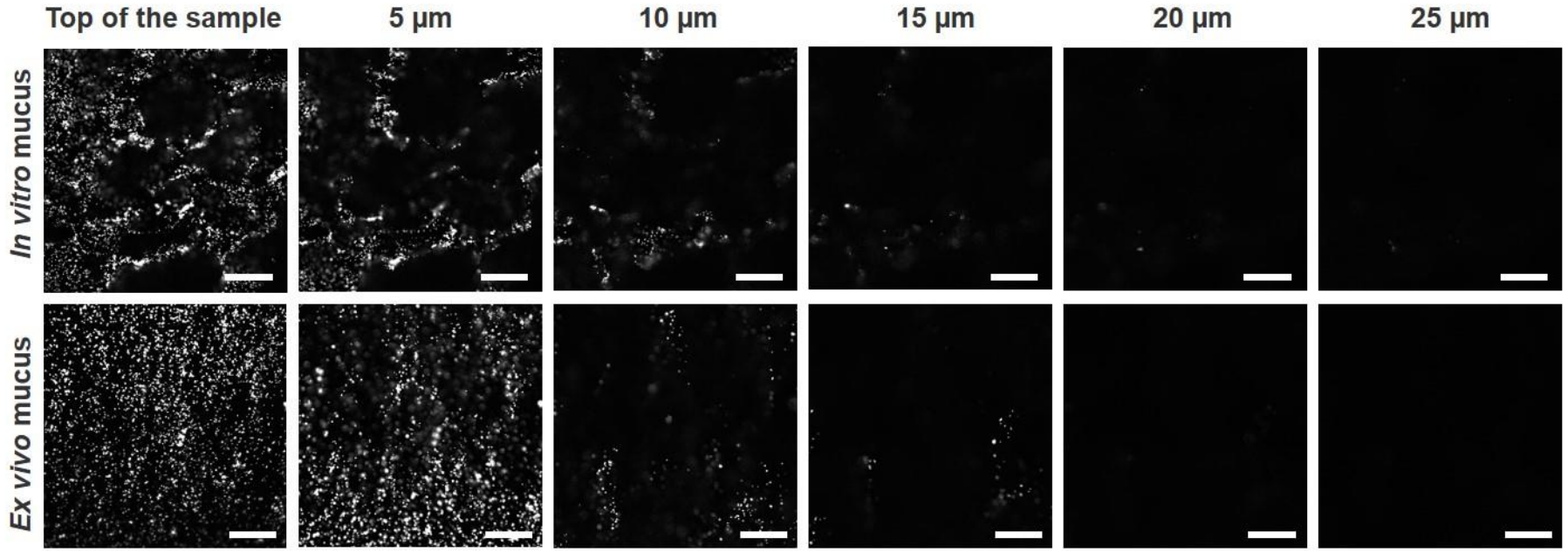

Supplementary Figure S4.1: CLSM images of 500 nm COOH-PS-Ps at different levels of *in vitro* and *ex vivo* mucus, starting from the top to the 25 µm depth of the sample. Scale bar 50 µm.

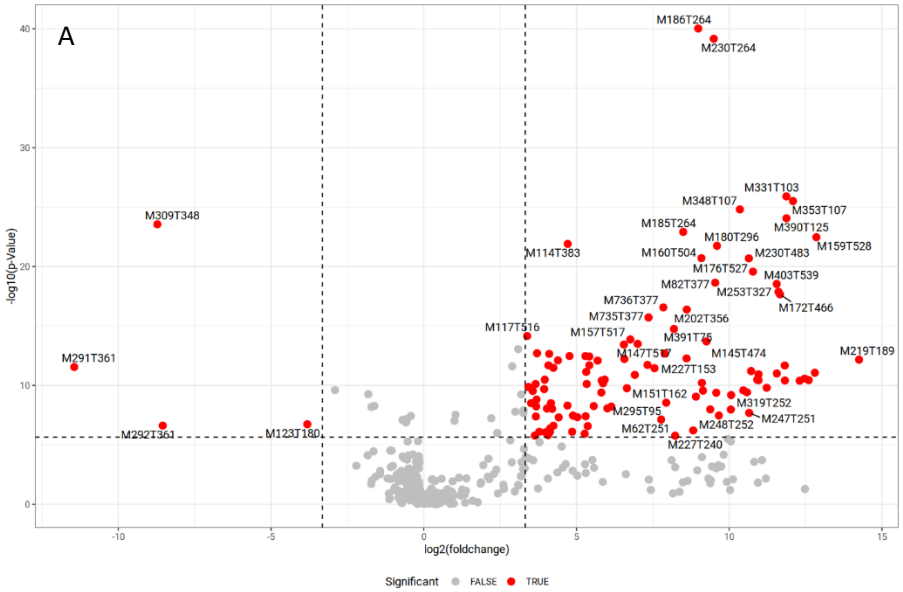
A
M186T264
M230T264
M309T348
M331T103
M348T107
M353T107
M185T264
M390T125
M180T296
M159T528
M114T383
M160T504
M230T483
M176T527
M403T539
M82T377
M253T327
M736T377
M172T466
M735T377
M202T356
M117T516
M157T517
M391T75
M291T361
M147T517
M145T474
M219T189
M227T153
M151T162
M319T252
M295T95
M247T251
M292T361
M123T180
M62T251
M248T252
M227T240
-log10(p-Value)
log2(foldchange)
Significant FALSE TRUE

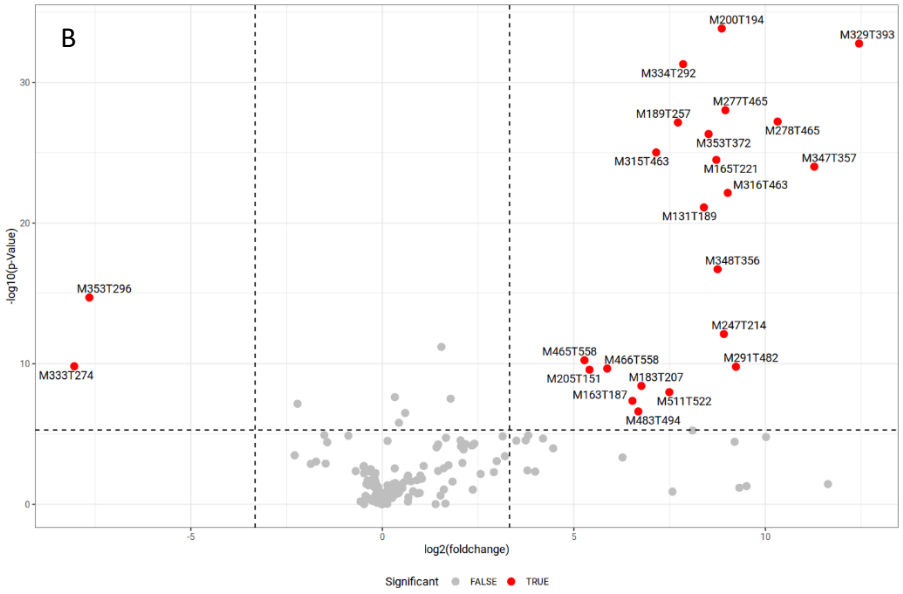
B
M200T194
M329T393
M334T292
M277T465
M189T257
M278T465
M353T372
M315T463
M347T357
M165T221
M316T463
M131T189
M348T356
M353T296
M247T214
M465T558
M466T558
M291T482
M333T274
M205T151
M183T207
M163T187
M511T522
M483T494
-log10(p-Value)
log2(foldchange)
Significant FALSE TRUE


C
M165T481
M257T175
M330T104
M303T175
M343T124
M345T107
M200T84
M410T177
M316T98
M290T207
M347T178
M187T342
M209T306
M392T106
M275T84
M265T84
M230T84
M221T341
M288T84
M203T152
M369T359
M212T147
M251T329
M287T340
M299T344
M320T173
M341T208
M227T207
M251T340
M158T85
M273T207
M287T189
M189T183
M378T98
M278T107
M286T84
M290T84
M194T483
M157T182
M274T207
M273T81
M157T301
M217T82
M151T102
M355T189
M289T85
M267T266
M147T544
M164T455
M306T346
M242T528
M241T189
M293T342
M145T526
M111T164
M197T354
M307T217
M344T352
M329T104
M213T526
M179T158
M315T98
M182T244
M410T318
M129T304
M127T73
M236T350
M232T478
M166T380
M336T219
M183T219
M288T189
M291T107
M151T271
M187T356
M259T122
M163T311
M483T366
-log10(p-Value)
log2(foldchange)
Significant FALSE TRUE

Supplementary Figure S4.2: Volcano plot showing the statistical untargeted metabolomics comparison between *in vitro* and *ex vivo* mucus. The y-axis corresponds to the -log 10 of t-test statistical *p*-value and x-axis corresponds to the log2 fold change (*ex vivo* mucus/ *in vitro* mucus). Each point in the figure is characterized by its *m/z* and retention time. The values with a fold change < 0.1 and > 10 and a Bonferroni corrected *p*-value < 0.001 were classified as significant and highlighted in red. Data shown are obtained from *n* tot = 53 samples; *n ex vivo* mucus = 37, *n in vitro* mucus = 16. A) HILIC column and positive mode B) Phenyl-Hexyl column and negative mode C) HILIC column and negative mode.

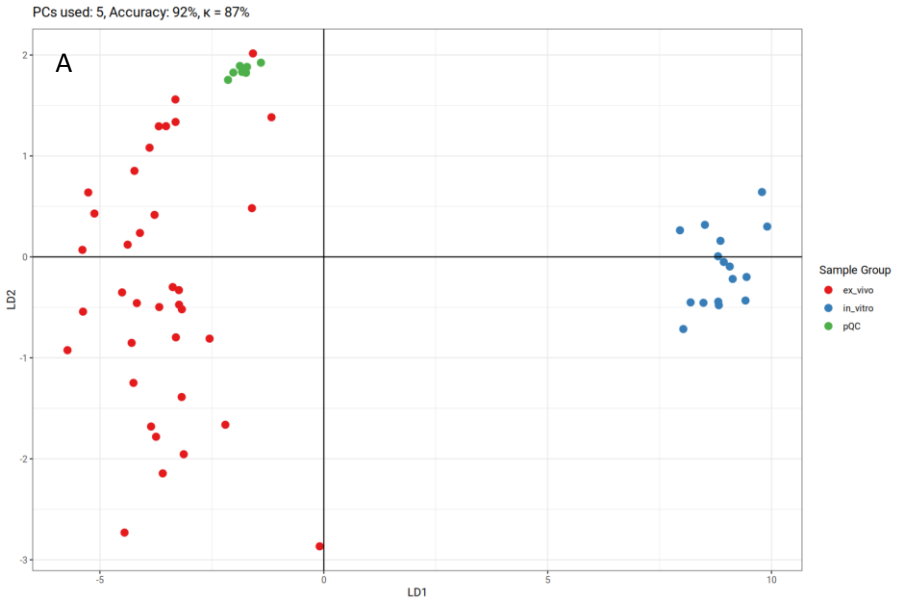
PCs used: 5, Accuracy: 92%, κ = 87%
A
LD2
LD1
Sample Group
ex_vivo
in_vitro
pQC

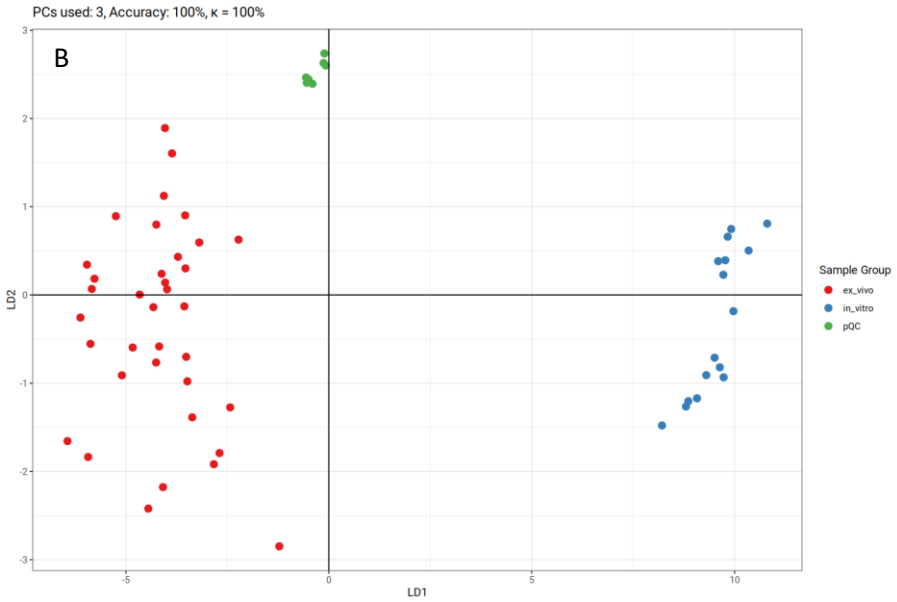
PCs used: 3, Accuracy: 100%, κ = 100%
B
LD2
LD1
Sample Group
ex_vivo
in_vitro
pQC

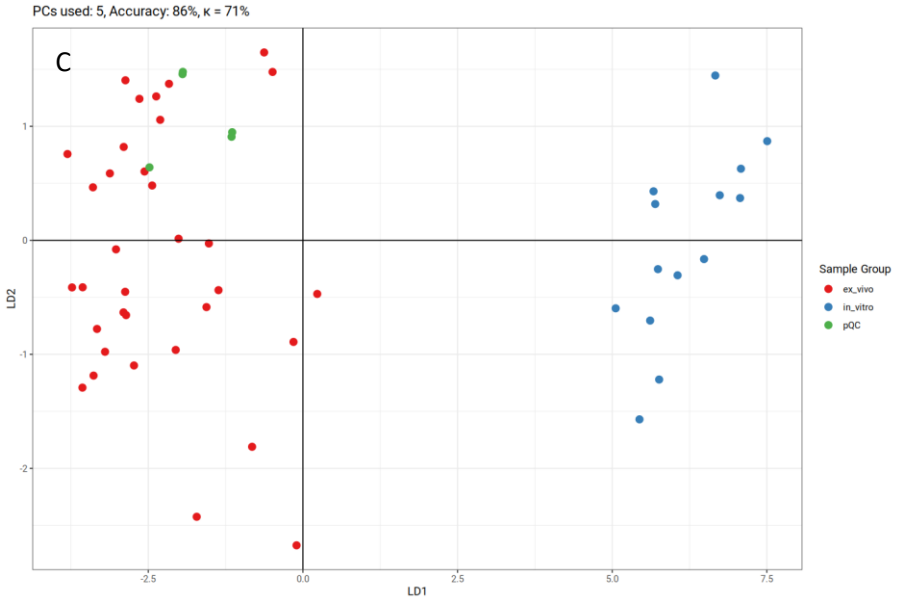
PCs used: 5, Accuracy: 86%, κ = 71%
C
LD2
LD1
Sample Group
ex_vivo
in_vitro
pQC

Supplementary Figure S4.3: Scores of principal component - linear discriminant analysis (PC-LDA) for *in vitro* and *ex vivo* mucus. The number of principal components used, the prediction accuracy, and Cohen's κ is given for each graph. A) HILIC column and positive mode B) Phenyl-Hexyl column and negative mode C) HILIC column and negative mode.

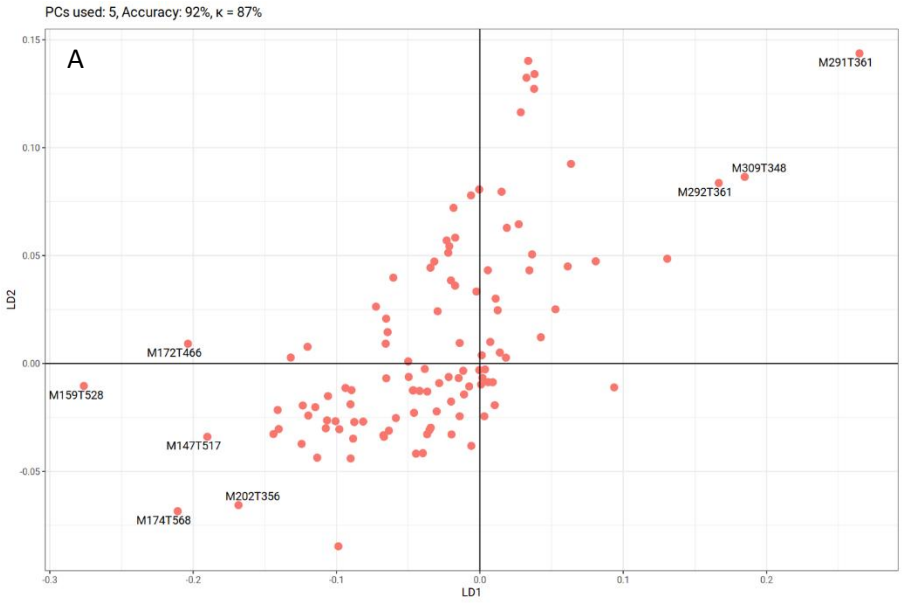
PCs used: 5, Accuracy: 92%, κ = 87%
A
M291T361
M309T348
M292T361
M172T466
M159T528
M147T517
M202T356
M174T568
LD1
LD2

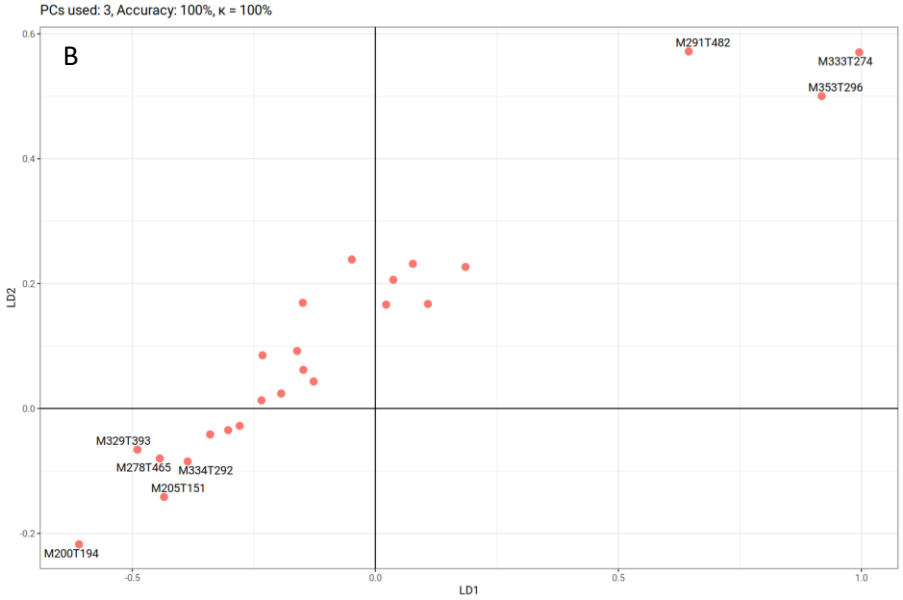
PCs used: 3, Accuracy: 100%, κ = 100%
B
M291T482
M333T274
M353T296
M329T393
M278T465
M334T292
M205T151
M200T194
LD1
LD2

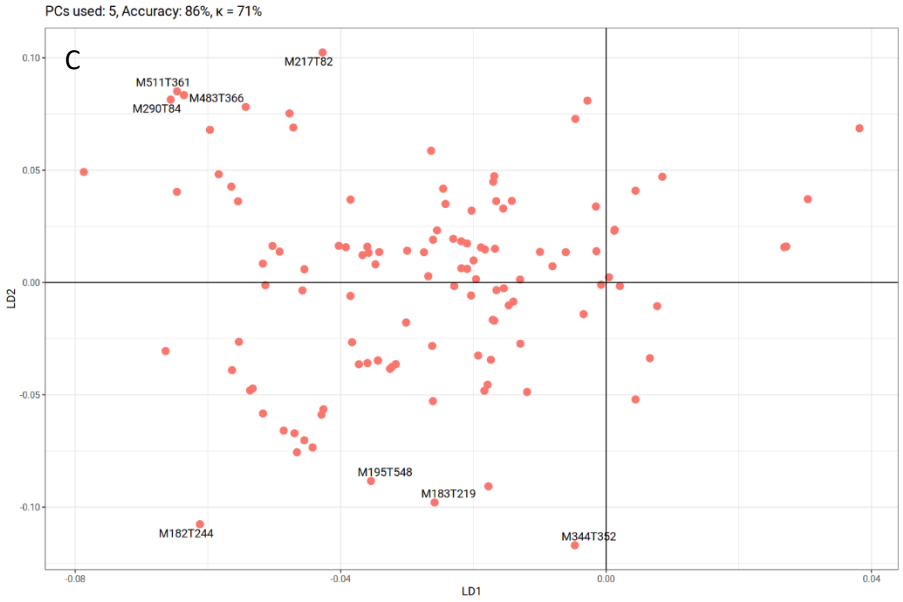
PCs used: 5, Accuracy: 86%, κ = 71%
C
M217T82
M511T361
M483T366
M290T84
M195T548
M183T219
M182T244
M344T352
LD1
LD2

Supplementary Figure S4.4: Loadings of principal component - linear discriminant analysis (PC-LDA) for *in vitro* and *ex vivo* mucus. The most important features are annotated. The number of principal components used, the prediction accuracy, and Cohen's κ is given for each graph. A) HILIC column and positive mode B) Phenyl-Hexyl column and negative mode C) HILIC column and negative mode.

5. Impact of mucus modulation by N-acetylcysteine on nanoparticle toxicity

This chapter has already been published in the following research paper:

E. Meziu, K. Shehu, M. Koch, M. Schneider, A. Kraegeloh.; *Impact of mucus modulation by N-acetylcysteine on nanoparticle toxicity*. *Int. J. Pharm: X 6 (2023) 100212.*

Author Contributions

E.M. and K.S. contributed equally to this work. E.M., M.S., A.K., designed the study. E.M. performed the characterization of microvilli formation and mucin secretion of cells. K.S. performed tight junction characterization, nanoparticle penetration and cytotoxicity experiments. E.M. and K.S. performed mucus thickness analysis. M.K. carried out electron microscopy. E.M., K.S., M.K., M.S., A.K., contributed to data analysis. E.M., K.S., M.S., and A.K. wrote the paper. All authors have given approval to the final version of the manuscript.

Abstract:

Human respiratory mucus is a biological hydrogel that forms a protective barrier for the underlying epithelium. Modulation of the mucus layer has been employed as a strategy to enhance transmucosal drug carrier transport. However, a drawback of this strategy is a potential reduction of the mucus barrier properties, in particular in situations with an increased exposure to particles. In this study, we investigated the impact of mucus modulation on its protective role. *In vitro* mucus was produced by Calu-3 cells, cultivated at the air-liquid interface for 21 days and used for further testing as formed on top of the cells. Analysis of confocal 3D imaging data revealed that after 21 days Calu-3 cells secrete a mucus layer with a thickness of 24 ± 6 µm. Mucus appeared to restrict penetration of 500 nm carboxyl-modified polystyrene particles to the upper 5 – 10 µm of the layer. Furthermore, a mucus modulation protocol using aerosolized N-acetylcysteine (NAC) was developed. This treatment enhanced the penetration of 500 nm particles through the mucus down to deeper layers by means of the mucolytic action of NAC. These findings were supported by cytotoxicity data, indicating that intact mucus protects the underlying epithelium from particle-induced effects on membrane integrity. The impact of NAC treatment on the protective properties of mucus was probed by using 50 and 100 nm amine-modified and 50 nm carboxyl-modified polystyrene nanoparticles, respectively. Cytotoxicity was only induced by the amine-modified particles in combination with NAC treatment, implying a reduced protective function of modulated mucus. Overall, our data emphasize the importance of integrating an assessment of the protective function of mucus into the development of therapy approaches involving mucus modulation.

5.1. Introduction

Human pulmonary mucus is a viscoelastic hydrogel with a complex composition and molecular structure that humidifies, lubricates, and protects the underlying airway epithelium [68]. The primary structural building blocks of mucus are mucin glycoproteins that consist of a protein backbone and oligosaccharide side chains. Mucin terminals contain non-glycosylated cysteine rich domains, which are responsible for disulfide bond formation, and allow the formation of a three-dimensional covalently linked hydrogel. The various regions of mucin molecules show unique properties and interact through

hydrophobic, hydrophilic, and electrostatic or specific interactions [96]. Given these structural and chemical properties, mucus traps and removes harmful entities like microbes, pollutants and xenobiotics by adhesive and steric filtering followed by mucociliary clearance [41]. Besides its protective function, mucus represents a selective barrier for transmucosal drug carriers, which need to overcome the mucus layer in order to yield a therapeutic effect. Strategies employed to enhance mucus penetration of drug carriers can broadly be summarized as drug carrier modifications, mucus modulation (by pretreating mucus with a mucus modulating agent), and synergistic combination of both approaches [114].

The strategy of mucus modulation is especially relevant in diseases related to hyperconcentrated mucus (*e.g.,* cystic fibrosis, chronic obstructive pulmonary disease). Modulation of mucus can be achieved by various approaches. Main strategies aim at either increasing mucus hydration, breaking covalent interactions between mucins or other mucus macromolecules, and reducing non-covalent interactions between mucus components [115]. Mucolytic agents, of which NAC is a well-known example, also serve as penetration enhancer for transmucosal drug carriers. Such treatment involves pre- or co-treatment of mucus with the mucolytic agent applied via inhalation prior- or simultaneously to the application of the relevant drug carrier [28,116]. The ease of use is one advantage of this technique compared to the challenging large-scale production of surface-modified drug carriers [114]. While mucus modulation facilitates penetration of drug carriers, it simultaneously compromises its protective function against other inhalable, potentially hazardous materials, including biological particulate matter and abiotic particles, such as cigarette smoke, environmental and anthropogenic fine dust, engineered nanomaterials, advanced materials, and microplastics [117–120]. Loss of the protective function of mucus and increased vulnerability of the underlying epithelium towards inhalable, potentially hazardous materials is one major concern regarding this strategy [15]. Although mucus is considered an efficient barrier against such foreign entities, there is evidence suggesting that for example engineered nanomaterials possess mucus penetrating properties [121]. Once the mucus barrier is overcome, these nanoparticles might reach and damage the underlying epithelium [122]. This risk potentially increases after modulation of mucus, emphasizing the importance to evaluate whether, after modulation, mucus retains its protective function against abiotic particles.

The impact of mucus modulation on unintended penetration and subsequent effects of abiotic particles remains poorly investigated.

In this study, the barrier capacity of modulated mucus was probed using model polystyrene nanoparticles. *In vitro* mucus was obtained by cultivating Calu-3 cells at the air-liquid interface [51,123]. In the first part, the basic properties of the employed Calu-3 mucus model were monitored regarding integrity of the cellular barrier, cell morphology, mucin production, and mucus layer formation. Secondly, an efficient mucus modulation protocol, comprising pre-treatment of mucus with nebulized N-acetylcysteine, was developed. Finally, the protective role of mucus upon modulation was evaluated by microscopy analysis of particle penetration into the mucus and by determining cytotoxicity, induced by polystyrene model nanoparticles.

5.2. Materials and Methods

5.2.1. Particles and particle characterization

Amine-modified polystyrene nanoparticles (NH_2-PS-NPs) (50 and 100 nm diameter), carboxyl-modified polystyrene nanoparticles (COOH-PS-NPs) (50 nm diameter) obtained from Sigma Aldrich (Steinheim, Germany) and 500 nm (diameter) dragon green-conjugated carboxyl-modified polystyrene particles (COOH-PS-Ps) (Bangs Laboratories, Fisher Scientific, USA) were used for probing the barrier and protective properties of mucus. The average hydrodynamic diameter of the particles was evaluated at 25 °C by dynamic light scattering using a Zetasizer NanoZSP instrument (Malvern Instruments, Worcestershire, UK) (Table 5.1). Samples were diluted 1:1000 in Dulbecco`s phosphate buffered saline (DPBS). A HeNe laser (λ = 633 nm) was used to irradiate samples and the fluctuating intensity of the scattered light was detected at a backscattering angle of 173°. Measurements were performed in triplicates. The zeta potential of the particles was determined using a Zetasizer NanoZSP instrument (Malvern Instruments, Worcestershire, UK). Samples were diluted 1:9 in 10 mM KCl. Three independent measurements were performed (Table 5.1).

Table 5.1: Physicochemical properties of particles used in this study.

PS-NPs	Labeling	Hydrodynamic diameter [nm]	Zeta potential [mV]	Experiments
500 nm COOH-PS-Ps	dragon green	452 +/- 99 nm	-57	CLSM Experiments
50 nm NH_2-PS-NPs	fluorescent blue	42 +/- 9 nm	47	LDH assay
100 nm NH_2-PS-NPs	fluorescent orange	70 +/- 16 nm	45	LDH assay
50 nm COOH-PS-NPs	-----	45 +/- 10 nm	-48	LDH assay

5.2.2. Cell culture

Calu-3 (HTB-55^{TM}) epithelial cells [124] were obtained from the American Type Culture Collection (ATCC; Rockville, MD, USA) and used as mucus-producing cell model. Cells were maintained in a humidified incubator (37 °C, 5% CO_2, and pH 7.4). Minimal essential medium (Gibco Invitrogen, Grand Island, USA) was supplemented with 10% fetal bovine serum (PAN-Biotech GmbH, Aidenbach, Germany), 1% sodium pyruvate (Life Technologies, Grand Island, USA), 1% non-essential amino acids (Life Technologies, Grand Island, USA), and 50 U/ml Penicillin and 50 µg/ml Streptomycin (Gibco Invitrogen, Grand Island, USA). Calu-3 cells were sub-cultivated when they attained a confluence of around 70% by firstly washing them with a pre-warmed DPBS (Sigma-Aldrich, Steinheim, Germany) solution. Afterwards, they were trypsinized for 20 min with a 0.05% trypsin solution containing 0.02% EDTA (PAN Biotech, Aidenbach, Germany).

For mucus production, cells at passage numbers up to 15 were seeded at a density of 10^5 cells/ml in transwell plates with membrane inserts (1.12 cm^2 surface area and 0.4 µm pore size) (Greiner Bio-One GmbH, Frickenhausen, Germany). The plates initially contained 1500 µl medium in the basolateral compartment and 500 µl medium in the apical compartment. Cells were allowed to adhere to the apical transwell membrane covered with medium for 24 h. After removal of the apical medium, the cells were cultivated at air-interfaced culture (AIC) conditions for up to 21 days in order to promote cell differentiation [125]. The basolateral medium was replaced every other day.

5.2.3. Transepithelial electrical resistance (TEER)

The formation of a confluent and tight monolayer was monitored by evaluation of TEER values by using STX-2 electrodes connected to an EVOM™ Epithelial Voltohmmeter (WPI, Sarasota, USA). During assessment of TEER values, 500 µl pre-warmed medium was added to the apical compartment. TEER values were calculated by subtracting the blank values of

empty transwell inserts from the measured values of the samples. TEER values of ≥ 300 Ω cm^2 were considered to indicate the formation of tight cell barriers [51,126].

5.2.4. Scanning electron microscopy (SEM)

For visualization of the Calu-3 cell surface, mucus was removed by washing the apical compartment with phosphate-buffered saline (PBS). Samples were then fixed with a 2% glutaraldehyde solution for 30 min and dehydrated by incubation in a graded ethanol series (30% – 96%, 10 min at each concentration). Subsequently, samples were immersed twice in absolute ethanol for 30 min, in hexamethyldisilazane (HMDS) (Carl Roth, Karlsruhe, Germany) / ethanol (1/1, v/v) for 15 min and pure HMDS (twice) for 15 min. Cells were air-dried overnight to allow for evaporation of the organosilicon compound. The filter supporting the Calu-3 cells was separated from the transwell insert. Samples were then placed on aluminum stubs using double-sided carbon tape. Imaging was carried out using FEI (Hillsboro, Oregon, United States) Quanta 400 FEG in low vacuum mode (100 Pa) using a large field detector and acceleration voltages of 5 kV and 10 kV at a working distance of 7.5-13.0 mm.

5.2.5. Sample preparation for confocal microscopy

Staining of the cellular mucus model: Cell samples were fixed using freshly prepared 4% (v/v) paraformaldehyde (Electron microscopy science, Hatfield, UK) and permeabilized with 0.2% Triton-X 100 solution (Carl Roth, Karlsruhe, Germany). Paraformaldehyde as a crosslinking fixative has been used, as it has been described before to successfully preserve mucus structure [13,76,85]. Subsequently, samples were blocked with 5% (w/v) bovine serum albumin (Carl Roth, Karlsruhe, Germany). Fluorescence staining for cell junctions, actin, and mucins was performed as follows:

For staining of occludin, after addition of 10 µg/ml mouse anti-occludin primary antibody (Santa Cruz Biotechnology Inc., CA. USA), samples were incubated overnight at 4 °C. 10 µg/ml Atto 647N conjugated anti-mouse secondary antibody (Sigma Aldrich, Steinheim, Germany) was added and incubated for 90 min at room temperature (RT).

Zonula occludens-1 (ZO-1) was stained with 0.625 ng/ml rabbit anti-ZO-1 primary antibody (Life Technologies, Rockville MD, USA) overnight at 4 °C and subsequently with 5 µg/ml Alexa Fluor 488 conjugated anti-rabbit secondary antibody (Sigma Aldrich, Steinheim

Germany) overnight at 4 °C.

For staining of E-cadherin, samples were incubated with 10 µg/ml mouse anti-E-cadherin primary antibody (Santa Cruz Biotechnology Inc., CA, USA) overnight at 4 °C and 10 µg/ml Atto 647N conjugated anti-mouse secondary antibody for 90 min at RT.

For actin staining, samples were incubated with 100 nM phalloidin Atto 647N (Atto-Tec, Siegen, Germany) for 1 h at RT.

For MUC5B staining, samples were incubated with 2 µg/ml mouse anti-MUC5B primary antibody (Thermo Fisher Scientific, Rockford, USA) for 1 h at RT and 10 µg/ml Atto 647N conjugated anti-mouse secondary antibody (Sigma Aldrich, Siegen, Germany) for 1 h at RT. MUC5AC was stained using 2 µg/ml rabbit anti-MUC5AC primary antibody (antibodies-online GmbH, Aachen, Germany) for 1 h at RT and 10 µg/ml Alexa Fluor 488 conjugated anti-rabbit secondary antibody (Sigma Aldrich, Steinheim Germany) for 1 h at 4 °C as described before [13]. Subsequently, stained samples were embedded in Mowiol 488 (Carl Roth, Karlsruhe, Germany).

Staining of glycoproteins using wheat germ agglutinin: Staining of *in vitro* mucus was performed prior to the evaluation of mucus thickness and for the investigation of particle transport through Calu-3 mucus. The staining agent was applied at the basolateral compartment to avoid mucus dilution. Calu-3 cells were stained with 100 µg/ml wheat germ agglutinin-tetramethyl Rhodamine (WGA-Rhod) (Vector Laboratories Inc., CA, USA) for 2 h at 37 °C. The treatment also results in staining of intracellular and membrane bound glycoproteins. Nevertheless, the staining allowed for a morphological discrimination between mucus and cell layer (Supplementary information, Figure S5.1). Prior to imaging, the membranes including the attached Calu-3 cells were separated from the transwell insert and placed on an Ibidi® imaging dish with a coverslip bottom.

5.2.6. Confocal laser scanning microscopy (CLSM)

Samples were examined with a TCS-SP5 STED setup (Leica Microsystems, Mannheim, Germany), in confocal mode, using the oil immersion objectives 63X/1.4 and 100X/1.4 (HCX PL APO). The fluorescent dyes Alexa 488 and Dragon Green were excited using the 488 nm laser line of an argon laser (λ = 488 nm). Atto 647N and rhodamine were excited using a HeNe laser (λ = 633 nm), and a DPSS laser (λ = 561 nm) respectively. The fluorescence signals were detected using a photomultiplier. For analysis of mucus thickness

and particle penetration, z-stacks (step size 1 µm) of the samples were recorded. To allow for quantitation of the intensities between different images, the settings for image acquisition were kept constant.

5.2.7. Image processing

For the quantification of particle transport across mucus, the raw fluorescence intensity of the particle signals in the obtained z-stacks was quantitatively analyzed using *Image J* software, version 1.53e. For analysis of mucus thickness, the recorded z-stacks were reconstructed using *Image J* software and analyzed to determine the distance between the outermost mucus layer and cell layer (mucus thickness).

5.2.8. Exposure of Calu-3 cells to aerosols using Vitrocell® Cloud 6

Calu-3 cells grown under AIC were exposed to NAC and/or polystyrene particles using the Vitrocell® Cloud 6 system (VITROCELL Systems GmbH, Waldkirch, Germany). NAC, particles, and NaCl were nebulized using an Aerogen Pro vibrating mesh nebulizer (Aerogen Ltd. Galway, Ireland) (nominal average droplet size range 4 µm). The nebulized doses were monitored with the integrated quartz crystal microbalance [127].

To analyze particle penetration, cell samples were stained with WGA-Rhod as described in section 5.2.5., prior to particle treatment. Subsequently, samples were exposed to 200 µl of 500 nm dragon green-labeled COOH-PS-Ps at a particle concentration (solid content) of 10 mg/ml. Samples were incubated for 3 h at 37 °C prior to microscopy analysis.

For treatment of cell samples with NAC, a solution of 20% NAC (Pharmazell GmbH, Barsbüttel, Germany) in 0.9% NaCl (Carl Roth GmbH, Karlsruhe, Germany) at pH 7.5 was prepared [52]. The dose of NAC to be deposited during the experiments, was estimated by considering the clinical dose (3–5 ml of 20% (w/v) NAC solution given 3–4 times/day), the tracheobronchial surface area (2471 cm^2) [121], and the deposition factor (percentage of the applied dose that reaches the respiratory tract) (10%) [128,129]. Based on this approach, 120 µg/cm^2 NAC was calculated to be deposited onto the tracheobronchial surface per day during clinical use. In this study, the impact of NAC on particle penetration was investigated using two doses: 20 µg/cm^2 NAC, approximating the lowest amount of NAC delivered by a single administration and 120 µg/cm^2 NAC, approximating the maximum cumulative daily dose of NAC during pulmonary administration. NAC treated

samples were incubated for 30 min at 37 °C as suggested by Suk et al., (2011) [52] prior to application of polystyrene particles. 0.9% NaCl was used as vehicle control and applied at corresponding volumes.

For evaluation of particle induced cytotoxicity, Calu-3 cells were exposed to 25 µg/cm^2, 50 µg/cm^2, and 100 µg/cm^2 of NH_2-PS-NPs with a diameter of 50 nm and 100 nm and COOH-PS-NPs with a diameter of 50 nm, respectively. Cells were then incubated for 24 h at 37 °C prior to performing the cytotoxicity assay.

5.2.9. Membrane integrity assay

After exposure of Calu-3 cells to NPs as described in section 5.2.8, membrane integrity was determined based on the activity of lactate dehydrogenase (LDH) in the cell culture medium. The CytoTox-ONE Homogeneous Membrane Integrity Assay (Promega GmbH, Walldorf, Germany) was used according to the manufacturer's instructions. In brief, 100 µl basolateral medium was removed, mixed with an equal volume of the assay reagent and incubated for 10 min at RT in the dark. After adding 50 µl of stop solution, fluorescence was recorded with a Tecan microplate reader (Tecan Trading AG, Männedorf, Switzerland) at an excitation wavelength of 560 nm and an emission wavelength of 590 nm. Background fluorescence of cell-free medium was subtracted from the recorded values. Membrane integrity was determined relative to a positive control (cells treated with 9% Triton X100).

5.3. Results and discussion

5.3.1 Calu-3 cells at the air-interface represent an adequate *in vitro* model for conducting mucus research

Calu-3 cells, cultivated at the air-interface, are a highly useful cellular mucus model for the investigation of delivery systems intended for pulmonary use [123]. Commercial availability and tight junction formation are the advantages of the Calu-3 cell line as an *in vitro* model [130]. In particular, mucus production when cultured at air-interface conditions, is an important benefit of the use of Calu-3 cell line, compared to other commonly used airway epithelium cells lines [44].

However, the mucin expression profile is another important mucus property. MUC5AC and MUC5B are the main mucins of airway mucus [123]. MUC5B has been described as

predominant mucin [131] in the healthy and the diseased state. In comparison, Calu-3 cells secrete MUC5AC over MUC5B [132]. However, this cell line has been used for particle penetration studies independent of a specific disease [51,123].

In vitro mucus, when used as formed on top of the cells, is beneficial as it cannot only be used for penetration studies, but also allows for monitoring cellular responses.

However, the characterization of such models in terms of mucus and mucin concentration is challenging, first of all due to formation of very low amounts of mucus especially after short cultivation times. Furthermore, mucus volume and concentration might be altered during mucus collection, especially, when washing steps are involved. Mucus concentration is defined as dry to wet weight content (% solids content), while mucin concentration describes the absolute mucin concentration [133–135]. Relating *in vitro* mucus properties to any specific physiological or pathological situation is limited by availability of quantitative information regarding mucus concentration under these conditions.

In the frame of this study, *in vitro* mucus was produced by Calu-3 cells cultured at air-interface conditions. Therefore, the properties of Calu-3 cells as an *in vitro* airway epithelial model for conducting mucus research were assessed in terms of barrier properties, morphology, and mucin production. The barrier properties of Calu-3 cells were evaluated by measurement of the TEER values combined with microscopy detection of protein structures characteristic for tight junctions. After 10 days, cells cultivated at air-interface conditions exhibited TEER values ≥ 300 Ω cm^2 (Figure 5.1 A), confirming the formation of an intact barrier [136]. Previous studies report inconsistent data regarding the required culture conditions (submerse vs. AIC) and duration (varying between 5 up to 16 days) to achieve TEER values, which are regarded as representative [125,137,138]. This emphasizes the importance of TEER value assessment. Barrier integrity of Calu-3 cells was further assessed by staining and visualizing cellular junctions. CLSM images confirmed the presence of occludin, ZO-1 and E-cadherin (Figure 5.1 B-D). These data are consistent with previous studies, reporting on tight junction formation in Calu-3 cells [45,139].

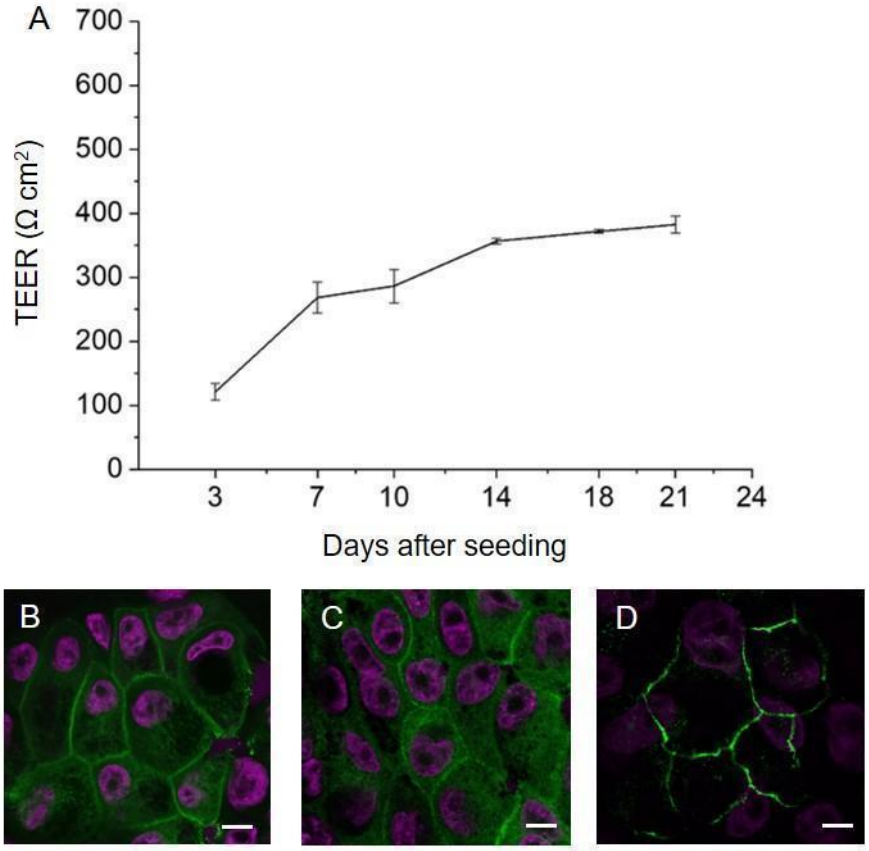

Figure 5.1: Development of barrier properties during cultivation of Calu-3 cells at the air-liquid interface for up to 21 days. A) TEER values indicate the formation of a tight monolayer (≥ 300 Ω cm2) starting from day 14. Data shown are mean values ± SE for n = 27 from 3 independent experiments. B-D) Expression of occludin (green) E-cadherin (green) and ZO-1 (green). Scale bar 10 µm.

SEM images of Calu-3 cells maintained at AIC revealed a heterogeneous population of apically located cellular protrusions (Figure 5.2 A-B). Such protrusions have been previously described as cilia (motility structures, containing microtubules) or microvilli (supported by actin) [45,140–142]. In this study, imaging of phalloidin labeled samples confirmed that the protrusions are actin-associated and therefore can be regarded as microvilli (Figure 5.2 C-D).

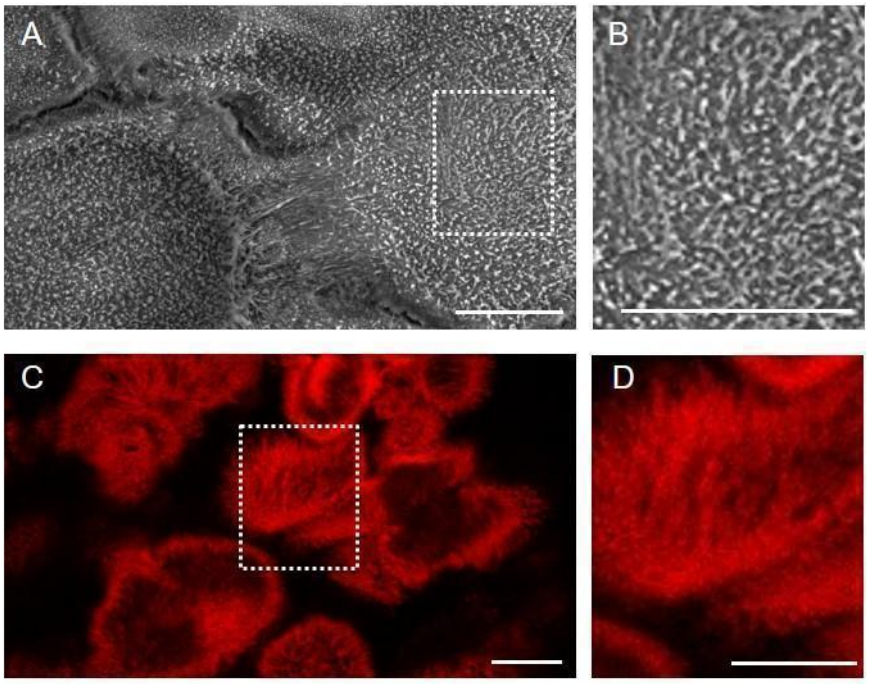

Figure 5.2: Protrusions at the apical surface of Calu-3 cells exposed to AIC conditions. A) SEM images show short protrusions in the middle of the cells and longer protrusions at the cell edges. B) Enlarged image of the area denoted with the dashed box in A. C) CLSM images of Calu-3 cells stained for actin with phalloidin Atto 647. D) Enlarged image of the area denoted with the dashed box in C. Scale bar 10 µm.

Furthermore, we investigated the mucin secreting activity of Calu-3 cells focusing on the two major gel-forming mucins of conducting airways, MUC5AC and MUC5B. CLSM sections recorded in the extracellular mucus layer covering Calu-3 cells revealed the presence of both MUC5B and MUC5AC (Figure 5.3 A and B). The overlay (Figure 5.3 C) revealed that in this layer, the mucins are not homogeneously distributed. Rather, regions predominantly containing MUC5AC or MUC5B or regions containing a mixture of both mucins could be differentiated.

CLSM sections through the cells revealed that the mucins MUC5AC and MUC5B are intracellularly located within round shaped structures, indicating their presence inside of membrane-bound vesicles (Figure 5.3 D and E) also called granules [18]. Again, the mucins appear to be unevenly distributed within the vesicles (Figure 5.3 F).

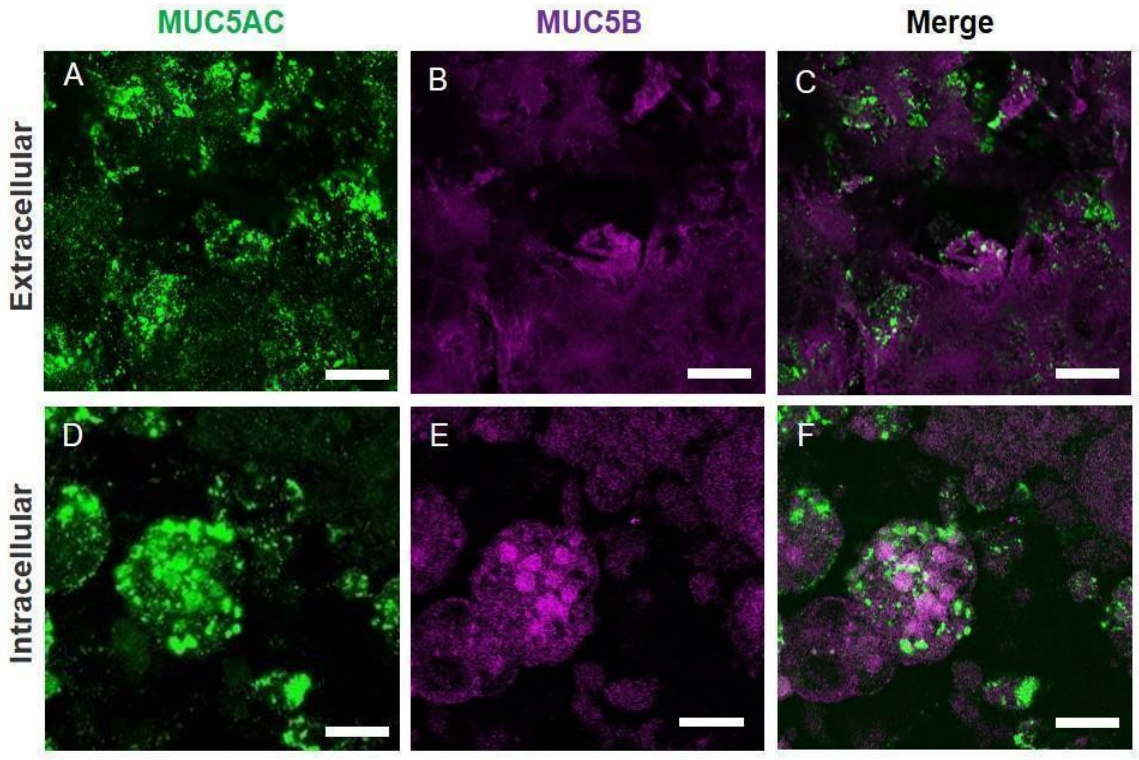

Figure 5.3: Calu-3 cells cultured under AIC conditions secrete the major gel-forming mucins MUC5AC and MUC5B. A-C) 2D sections taken above the cells demonstrate the secretion of both MUC5AC and MUC5B. D-E) 2D sections through the cells show the presence of MUC5AC and MUC5B filled granules. Samples were stained with anti-MUC5AC-Alexa Fluor 488 (green) and anti-MUC5B-Atto 647N (magenta). Scale bar 10 µm.

Several gene expression studies have reported the expression of both MUC5AC and MUC5B in Calu-3 cells [143,144]. Sonntag et al., (2022) assessed mucus production in Calu-3 cells by evaluating the level of MUC5AC formation [123]. Analyses based on immunofluorescence staining also confirmed the formation of MUC5AC and MUC5B by Calu-3 cells [145]. However, the ultrastructure of intracellular MUC5B and MUC5AC filled-granules and the resulting morphology of the mucus layer secreted by Calu-3 cells have previously been poorly addressed. Previous immunohistochemical studies found MUC5AC filled intracellular secretory granules residing at the apical side of Calu-3 cells, grown at the air-interface [146,147]. In general, goblet cells are polarized. The nucleus and organelles are reported to reside at the base of the cell, whereas the mucin-secreting vesicles accumulate at the apical side [148].

Tight junction formation resulting in generation of physiological TEER values together with

the secretion of the major gel-forming mucins confirmed the quality and adequacy of the employed Calu-3 model for conducting this study.

5.3.2. N-acetylcysteine improves particle penetration

NAC has mucolytic, antioxidant (ROS scavenging), and anti-inflammatory properties [149]. Given these properties, nebulized NAC has been clinically used in acute and chronic bronchopulmonary diseases that are associated with impaired mucus formation and transport [150]. However, its use as a mucus modulator with the scope of improving the diffusion of particulate based therapeutics [72] is yet a subject of ongoing research [114].

As a proof of concept, we investigated how pretreatment of mucus with nebulized NAC influenced the penetration behavior of 500 nm model COOH-PS-Ps through *in vitro* mucus. Particles larger than 200 nm have been described not to penetrate mucus [12]. Therefore, the 500 nm particles were chosen here as a control, allowing to show the mucus penetration enhancing effect of NAC. Pharmaceutical aspects such as high drug encapsulation efficiency and modifiable drug release kinetics are other considerations that in general foster the use of sub-micrometer to micrometer-sized particles in the field of formulation development [72].

For bearing resemblance to the treatment situation, the exposure of Calu-3 cells to NAC and PS-NPs was performed using the Vitrocell ® Cloud system. NAC solution was nebulized and administered at doses of 20 µg/cm^2 ± 10% and 120 µg/cm^2 ± 10%. 3 h after particle application, 2D images were recorded at different optical z-sections starting from the top of the mucus layer of the samples (Figure 5.4) as illustrated in (Supplementary information Figure S5.2). The presence of particles was quantified (Figure 5.5) based on fluorescence intensity and using *Image J* software.

In untreated samples, the 500 nm particles were only detected in the upper mucus layers. Signal intensity was highest at the top layer (0 µm) and decreased with increasing distance from the top. At distances of 15 µm and more, particles were only detected occasionally, even after 3 h of incubation (Figure 5.4). The impact of 0.9% NaCl, used as vehicle control for NAC, on the penetration of particles appeared to be negligible. Samples pretreated with NaCl did not exhibit particle penetration to more distant layers as compared to untreated samples (Supplementary information, Figure S5.3). These results are in line with previous studies that reported a strong obstruction of 500 nm COOH-PS-Ps to diffuse through mucus

[12,38]. These data reveal that in its untreated state Calu-3 mucus shows considerable barrier properties and represents a promising mucus model for the investigation of mucus drug carrier interactions.

After pretreatment of the samples with 20 µg/cm^2 NAC, according to the quantitative analysis (Figure 5.5), no significant increase in particle penetration as compared to the untreated controls was detected. Under these conditions only a few more particle signals were detected at distances of 10 µm and 15 µm (Figure 5.4). In contrast, pretreatment of mucus with 120 µg/cm^2 NAC notably improved particle diffusion across mucus (Figure 5.5). Here, particles were detected up to a depth of 20 µm (Figure 5.4). In addition, the chain-like pattern of particles observed after pretreatment with 120 µg/cm^2 NAC (Figure 5.4) might indicate the presence of connections between the interstitial fluid-filled regions, accessible to the particles, as already observed before [51]. The enhanced nanoparticle diffusivity mediated by NAC can be attributed to an increase of these accessible fluid-filled areas, most likely mediated by the mucolytic properties of NAC. The latter have been described to be based on depolymerization of the mucin matrix by lysis of interconnecting disulfide bonds [151]. Ehre et al. (2019) reported that NAC leads to decrease of the molecular weight of mucins, however with a lower efficiency as compared to other novel mucolytics [152].

An increase of the mucus "mesh size" has also been suggested as an explanation for the improvement of nanoparticle transport after NAC treatment, based on SEM imaging [52]. However, care should be taken with the interpretation of such observations, as dehydration of samples for SEM imaging has been shown to cause structural alterations of mucus, resulting in the formation of µm-sized pores absent from the hydrated state [8,13,24].

Measurement of the osmolality of 20% NAC solution revealed that it is a hypertonic solution with an osmolality equivalent to 4.5% NaCl (Supplementary information Table S5.1). Application of 20% NAC solution therefore might also act as osmolyte, causing water influx into the mucus layer and thereby facilitating nanoparticle transport. To differentiate between the mucolytic and osmotic effect of NAC, Calu-3 cells, cultured for 21 days, were pretreated with 4.5% NaCl and 20% NAC. Subsequently, the transport of 500 nm COOH-PS-Ps in untreated, 4.5% NaCl treated, and 20% NAC treated samples was evaluated. Treatment with 4.5% hypertonic NaCl solution did not lead to a significant increase of nanoparticle transport compared to untreated controls (Supplementary information Figure S5.4). This indicates that the mucolytic effect of 20% NAC is dominating over the osmotic

or dilution effect. Given the established strong inverse proportionality of mucus viscoelasticity and particle diffusivity, the decrease of complex mucus viscoelasticity [31] via reduction of disulfide bonds by NAC, is most likely the key factor in the enhancement of particle diffusivity [153,154].

The quantitative image analysis confirmed that pretreatment of mucus with a 120 µg/cm^2 dose of NAC significantly increased the penetration of 500 nm COOH-PS-Ps. This behavior was observable from a visualization depth of ≥ 5 µm compared to untreated samples and samples pretreated with only 20 µg/cm^2 NAC (Figure 5.5). NAC treatment did also increase the penetration of 50 nm and 100 nm nanoparticles, as further described in section 5.3.5. Different to our findings, Suk et al., (2011) reported that the treatment of cystic fibrosis sputum with NAC at a concentration of 20 mM provided almost no improvement for 500 nm COOH-PS-Ps compared to untreated samples [52]. The reasons for this difference may be the even higher viscoelasticity of cystic fibrosis mucus and the pathology-related increased mucin concentration [155] of the used samples, as the NAC induced nanoparticle transport improvement is reported to be inversely correlated to mucin concentration [116]. Taken together, these data provide evidence that the NAC treatment protocol, proposed in this study, can substantially enhance the permeability of mucus and improve nanoparticle transport, indicating a reduced protective effect during such a treatment phase.

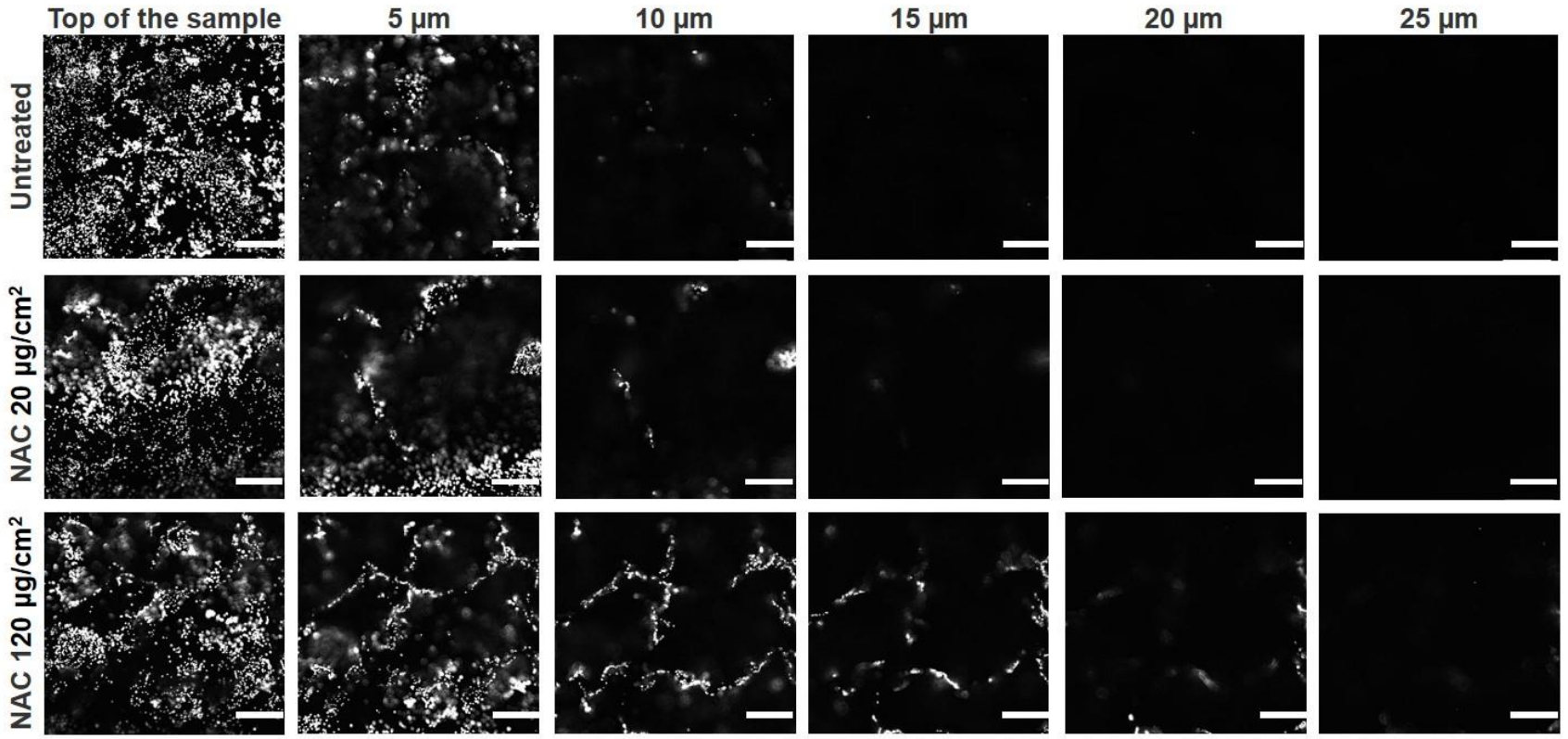

Figure 5.4: NAC treatment improves particle penetration into mucus. 2D CLSM images of 500 nm COOH-PS-Ps (white) at different depths of the mucus: 0 µm represents the top of the sample, 25 µm represents the bottom layer. Mucus was untreated (top row) or treated with 20 µg/cm^2 NAC (middle) and 120 µg/cm^2 NAC (bottom row), respectively. Particles and NAC were applied to the top of the sample. Scale bar 50 µm.

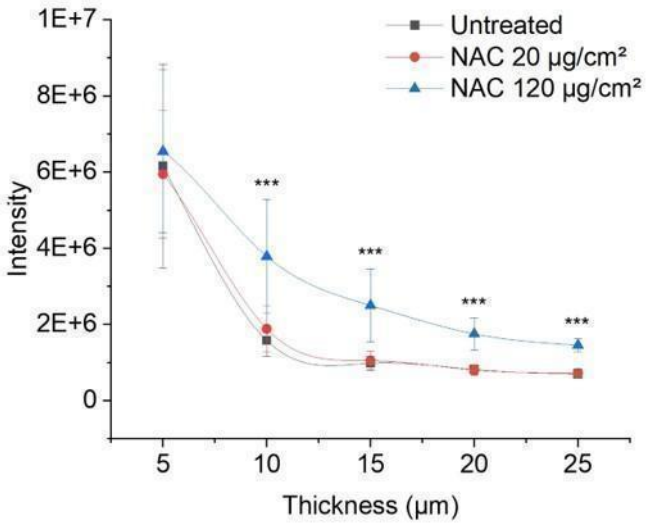

Figure 5.5: Quantitative analysis of 500 nm particle penetration after NAC treatment based on confocal imaging. Data shown are mean values ± SE for n = 9 sample areas from 3 independent experiments. Statistical significance was calculated with One Way ANOVA followed by the Bonferroni test and indicated by asterisks: ***, $p < 0.001$.

5.3.3. Time dependent formation of *in vitro* mucus

It has been reported that Calu-3 cells cultivated at air-interface conditions show a time-dependent mucus secretion [125]. In the frame of this study, the time-dependent secretion of mucus and build-up of a mucus layer was investigated. Considering the protective function of mucus, the thickness of a complete mucus layer equals the distance that delivery systems as well as potentially hazardous materials must travel to reach the underlying cells. Therefore, the thickness of the mucus layer was assessed by CLSM, after Calu-3 cells were cultivated at air-interface conditions for 5 days (Calu-3 5-d) and 21 days (Calu-3 21-d).

In order to avoid removal of loosely bound mucus mediated by washing steps, mucus was stained via application of labeled WGA to the basolateral compartment of the transwell filters. The membranes including the attached Calu-3 cells were separated from the transwell insert and placed on an Ibidi® imaging chamber for analysis (Figure 5.6 A). Morphological differences were used as a discrimination tool between the cells and the mucus layer (Figure 5.6 B). In contrast to previous studies, describing mucus as an even

layer [156], it was observed that the thickness of mucus was not uniform throughout the samples.

However, after 21 days, Calu-3 cells produced a confluent mucus layer (Supplementary information, Figure S5.5). Overall, the data indicated a significant increase of the mucus thickness over time (from 5 to 21 days). Calu-3 5d produced a mucus layer of 8.7 ± 4.5 µm, while Calu-3 21d produced a 2.8-fold thicker mucus layer of 24.1 ± 5.8 (Figure 5.6 C).

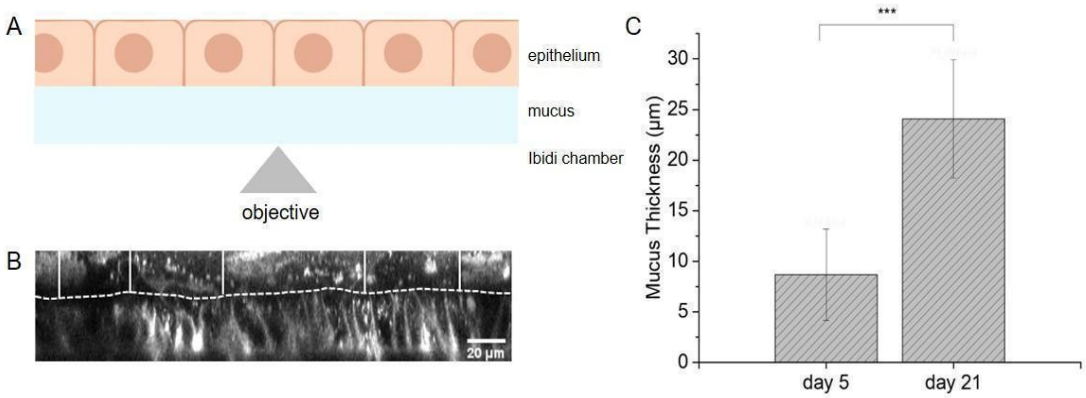

Figure 5.6: Thickness of *in vitro* mucus produced by Calu-3 cells increased with culturing time. A) Illustration of the applied CLSM imaging setup. B) Orthogonal view (xz) of mucus covering the epithelium reveals the morphological discrimination between the epithelium below the dashed line and mucus layer on top of the dashed line. Z-stacks of 2D images were analyzed using Image J to determine mucus thickness (distance between the top layer of mucus and the cell membrane). Mucus thickness was measured at five random spots (white lines) in each sample. Solid white lines represent mucus thickness at arbitrarily chosen locations. Note that the image in B) is rotated 180° as compared to A). C) Average thickness of *in vitro* mucus evaluated after cultivation of Calu-3 cells for 5 and 21 days. Data shown represent mean values ± SE for n = 45 measurements from 3 independent experiments. Statistical significance is calculated with One Way ANOVA followed by the Bonferroni test and indicated by asterisks: ***, $p < 0.001$.

In comparison, Sonntag et al., (2022) reported formation of an approximately 20 µm thick mucus layer by Calu-3 cells after 14 days, however no data was reported for longer cultivation times [123]. The mucus thickness determined in this study after 21 days correlated well with the thickness of human tracheal mucus (10 – 30 µm) corresponding to

the airway generation 0 [157,158]. For the subsequent assessment of the protective properties of mucus, Calu-3 cells were used after 5d and 21d of cultivation. For this assessment, a model exhibiting a confluent cell layer and exhibiting barrier properties, while completely lacking a mucus cover would have been the ideal negative control. After 5 days, the cell layer already was confluent (Supplementary information, Figure S5.6), whereas TEER values indicated incomplete barrier formation (Figure 5.1). However, as the cells were already covered by mucus after 5 days (Supplementary information, Figure S5.7), the 5d model was chosen to mimic the protective function of a thin mucus layer on top of confluent cells.

5.3.4. Protective role of *in vitro* mucus

To evaluate the protective function of mucus, Calu-3 cells were exposed to three types of model polystyrene nanoparticles. 50 nm and 100 nm NH_2-PS-NPs and 50 nm COOH-PS-NPs were applied at varying doses (25, 50 and 100 µg/cm^2). Polystyrene nanoparticles have been intensively used as model particles in the field of drug delivery [159], but also for nanotoxicity studies [160]. Due to the growing interest in the effects of nano- and microplastics and the potential formation of polystyrene particles due to plastic fragmentation, PS-NPs have also been used in terms of environmental/occupational exposure to these materials [161].

For the assessment of nanoparticle induced cytotoxicity, the LDH based membrane integrity assay was performed. For the assay, the nanoparticles were applied via nebulization to the apical compartment and the medium samples were taken from the basal compartment. Due to limited translocation of the particles across the transwell membranes, as shown by Dekali et al. (2014) [162], using an acellular translocation assay, significant (optical) interference of the particles with the assay readout can be neglected. Using this assay, cytotoxicity values of ≤ 20%, correlating with a low release of LDH, are considered non-toxic [163].

50 nm NH_2-PS-NPs applied at a dose of 25 µg/cm^2 induced no toxicity in Calu-3 5d and Calu-3 21d samples (Figure 5.7 A). At higher doses 50 and 100 µg/cm^2 50 nm NH_2-PS-NPs induced a dose-dependent cytotoxicity in both Calu-3 5d and 21d samples. 50 nm NH_2-PS-NPs induced in Calu-3 5d samples a significantly higher cytotoxicity than in Calu-3 21d.

100 nm NH_2-PS-NPs probed in Calu-3 5-d induced no cytotoxicity at a dose of 25 µg/cm^2 and a dose dependent cytotoxicity at doses of 50 and 100 µg/cm^2 (Figure 5.7 B). In samples with a thicker mucus layer Calu-3 21-d 100 nm NH_2-PS-NPs induced no toxicity for all applied concentrations. As in the literature described [164], the cytotoxicity induced by 50 nm NH_2-PS-NPs was observed to be higher than that of larger 100 nm NH_2-PS-NPs (Figure 5.7 A-B).

50 nm COOH-PS-NPs induced cytotoxicity only when applied at doses of 50 and 100 µg/cm^2 in Calu-3 5-d samples (Figure 5.7 C). As previously reported [165] the negatively charged 50 nm COOH-PS-NPs induced a lower cytotoxicity than positively charged 50 nm NH_2-PS-NPs (Figure 5.7 B-C).

The nanoparticle induced cytotoxicity was found to be dose dependent for all three nanoparticle types used and both models, Calu-3 cells cultured for 5 and 21 days (Figure 5.7 A-C). However, at the lowest dose used, 25 µg/cm^2, the nanoparticles did not induce cytotoxicity. These findings confirm previous results, reporting that the toxicity of nanoparticles increases with increasing concentration [166].

Furthermore, the nanoparticle induced cytotoxicity was more pronounced in case of the Calu-3 5- d samples as compared to the Calu-3 21-d samples (Figure 5.7 A-C).

These data indicated that Calu-3 5-d are more vulnerable to nanoparticle-induced cytotoxicity as compared to Calu-3 21-d.

Given the mucus thickness difference between Calu-3 5-d and 21-d, the lower nanoparticle-induced toxicity values observed in Calu-3 21-d are most likely attributed to the thick mucus layer and underline the protective function of mucus.

These results indicate that Calu-3 cells cultured at air-interface conditions for 21 days secrete a mucus layer of a thickness comparable to the human tracheal mucus that protects the underlying cells and can successfully be employed for the investigation of the impact of NAC on the protective role of mucus.

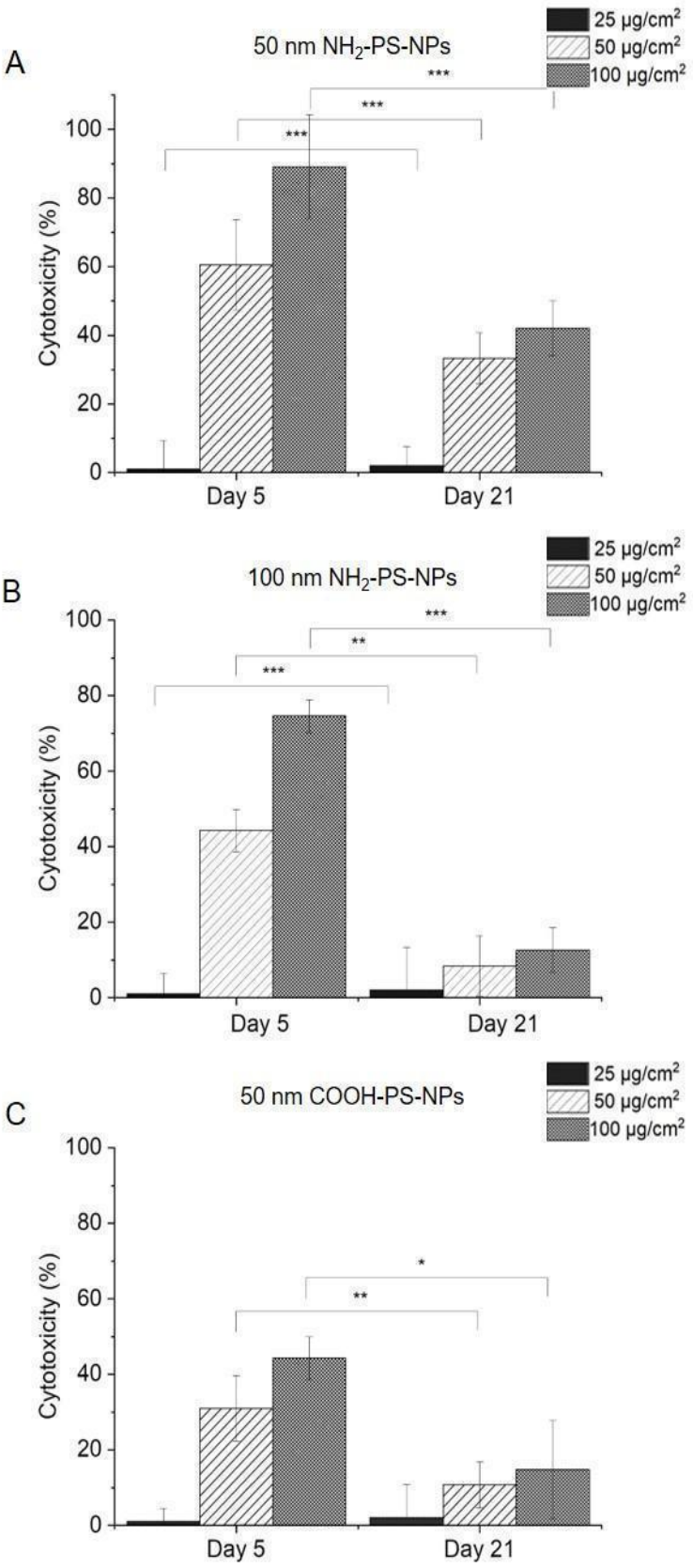
A
50 nm NH2-PS-NPs
25 µg/cm²
50 µg/cm²
100 µg/cm²
Cytotoxicity (%)
Day 5
Day 21
B
100 nm NH2-PS-NPs
C
50 nm COOH-PS-NPs

Figure 5.7: The protective function of mucus is determined by the thickness of the mucus layer. Samples were exposed to nebulized particles A) 50 nm NH_2-PS-NPs, B) 100 nm NH_2-PS-NPs and C) 50 nm COOH-PS-NPs at three different doses 25, 50, and 100 µg/cm^2. Data shown are mean values ± SE for n = 27 technical replicates from 3 independent experiments. Statistical significance is calculated with one-way ANOVA followed by the Bonferroni test and indicated by asterisks: *, $p < 0.05$; **, $p < 0.01$; ***, $p < 0.001$.

5.3.5. N-acetylcysteine modulation of mucus increases nanoparticle-induced cytotoxicity

A considerable concern about the increase of mucus permeability via NAC treatment is the vulnerability of the underlying epithelium toward inhalable xenobiotics. In this study, we address this question by probing the impact of NAC treatment on the protective role of mucus using nebulized model PS-NPs. Initial experiments were performed, in order to exclude that NAC itself induced cytotoxicity (Supplementary information, Figure S5.8). 50 nm NH_2-PS-NPs applied at a dose of 25 µg/cm^2 did not induce cytotoxicity, independent from any pretreatment with NAC. At higher doses (50 and 100 µg/cm^2) 50 nm NH_2-PS-NPs induced cytotoxicity in both NAC treated and untreated samples. Furthermore, the cytotoxic effect of the 50 nm NH_2-PS-NPs particles was more pronounced after NAC treatment (Figure 5.8 A). 100 nm NH_2-PS-NPs induced no toxicity in absence of NAC, independent on the applied dose. After NAC treatment, the 100 nm NH_2-PS-NPs induced toxicity, which was observed to increase with the applied dose (Figure 5.8 B). In comparison, 50 nm COOH-PS-NPs induced only slight effects, even when applied after NAC treatment at a dose of 100 µg/cm^2 (Figure 5.8 C).

Consistent with the existing literature, it was observed that exposure of cells to particles of smaller diameter and of positive charge caused a more pronounced cytotoxicity [167]. Most importantly, NAC-treatment increased the cytotoxicity induced by all particle types as compared to untreated samples (Figure 5.8 A-C). In particular, NAC treatment led to an increase in the cytotoxicity of 50 nm and 100 nm NH_2-PS-NPs (Figure 5.8 A, B).

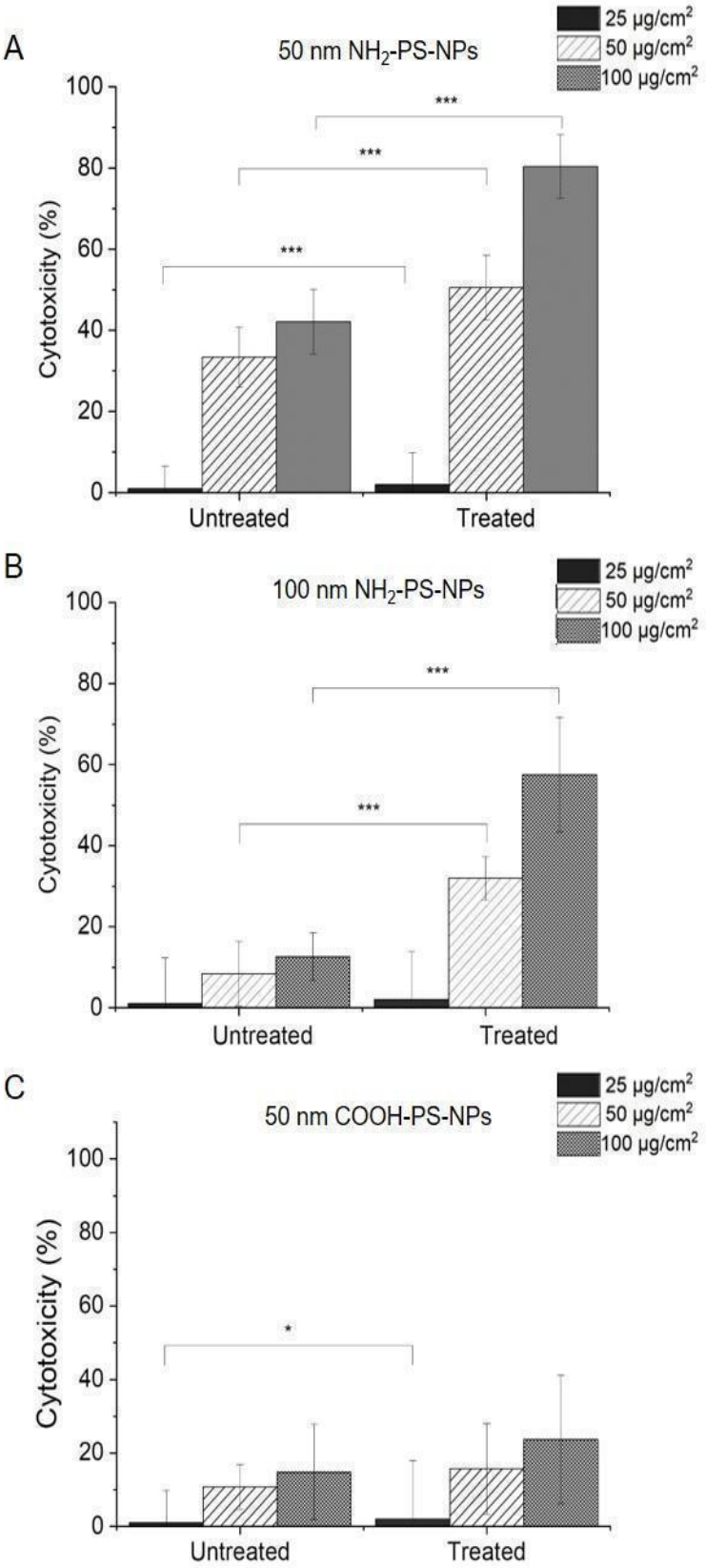
A
50 nm NH2-PS-NPs
25 µg/cm²
50 µg/cm²
100 µg/cm²
Cytotoxicity (%)
0
20
40
60
80
100
***
***
***
Untreated
Treated
B
100 nm NH2-PS-NPs
25 µg/cm²
50 µg/cm²
100 µg/cm²
Cytotoxicity (%)
0
20
40
60
80
100
***
***
Untreated
Treated
C
50 nm COOH-PS-NPs
25 µg/cm²
50 µg/cm²
100 µg/cm²
Cytotoxicity (%)
0
20
40
60
80
100
*
Untreated
Treated

Figure 5.8: Pretreatment with NAC decreases the protective function of mucus. Treated samples were exposed to nebulized NAC (120 µg/cm^2). Both treated and untreated samples were subsequently exposed to nebulized particles A) 50 nm NH_2-PS-NPs, B) 100 nm NH_2-PS-NPs and C) 50 nm COOH-PS-NPs at three different doses 25, 50, and 100 µg/cm^2. Data shown are mean values ± SE for n = 27 technical replicates from 3 independent experiments. Statistical significance is calculated with one-way ANOVA followed by the Bonferroni test and indicated by asterisks: *, $p < 0.05$; **, $p < 0.01$; ***, $p < 0.001$.

NAC is a well-known antioxidant and shows its antioxidant effect via various mechanisms. It plays a role as a cysteine and thereby glutathione precursor (a well-known direct antioxidant and a substrate of several antioxidant enzymes), acts as a direct antioxidant, and is assumed to be involved in thiol-disulfide interchange reactions, involved in restoration of thiol pools [152,168]. Having this in mind, NAC is expected to attenuate stressor induced oxidative stress due to its antioxidative properties. As polystyrene nanoparticle induced toxicity might be mediated by oxidative stress [169], NAC is expected to rather mitigate any nanoparticle induced toxicity. Given the nanoparticle penetration enhancing property of NAC, the increased cytotoxicity values observed after NAC treatment might rather be attributed to an elevated exposure of cells to an increased number of particles. Enhanced nanoparticle induced cytotoxicity observed for the NAC-treated samples suggests that NAC compromises the mucus barrier integrity and its protective function.

Therefore, the impact of NAC treatment on the penetration of nanoparticles was analyzed as described for the 500 nm particles. After 3 h, 100 nm NH_2-PS-NPs did not evenly distribute in the mucus. The fluorescence signals were predominately detected in the top layers. NAC treatment appeared to increase the presence of 100 nm NH_2-PS-NPs particles, even at deeper mucus layers (Supplementary Figure S5.9). In comparison, 50 nm COOH-PS-NPs, even without previous NAC treatment, seemed to distribute more evenly across the mucus and also to penetrate to deeper mucus layers. NAC treatment appeared to enhance the penetration of these particles into deeper mucus layers (Supplementary Figure S5.10).

The observed results are in good agreement with Takatsuka et al. (2006), addressing the impact of NAC treatment as a strategy to improve mucus penetration [170]. The authors

reported that treatment of rats with NAC led to an increased absorption of calcitonin, which was associated with mucosal and microvilli damage. However, it is to be noted that the mentioned study focuses on the intraintestinal application of NAC.

The use of mucus modulating agents like NAC to improve drug uptake by decreasing mucus barrier properties can be of advantage as it allows the application of simpler formulations. The improvement of mucus penetration in this scenario is achieved by the mucus modulating agent, applied prior to the use of the drug carrier. Such formulations can be realized by use of less complex and cheaper manufacturing processes [115], also resulting in lower costs for the development stage.

The data presented in this study emphasize that the application of mucus modulating strategies should be considered with caution, in particular if unintended exposure to particles is expected. In this context, a compromise should be made between the dose necessary to ensure the efficient delivery of the intended agent and the dose allowing for unintended penetration of environmental particles.

5.4. Conclusion

This study focuses on the impact of mucus modulation on the protective role of mucus taking into consideration the potential environmental/occupational exposure.

Differentiated Calu-3 cells as an *in vitro* mucus source have been characterized and a mucus modulation protocol involving the NAC nebulization that successfully enhanced NP transport through mucus has been developed. We demonstrated that Calu-3 cells provide a mucus layer of a thickness comparable to the human tracheal mucus, which protects the underlying cells and can successfully be employed for investigation of the protective role of mucus. We found that modulation of *in vitro* mucus via NAC significantly increased particle penetration and nanoparticle-induced cytotoxicity, indicating a reduced barrier capacity of modulated mucus.

Our results suggest that assessment of the impact of mucus modulation on the protective role of mucus is essential for a successful development of therapy protocols involving mucus modulation as a strategy for enhancing drug carrier penetration through mucus.

5.5. Supplementary information

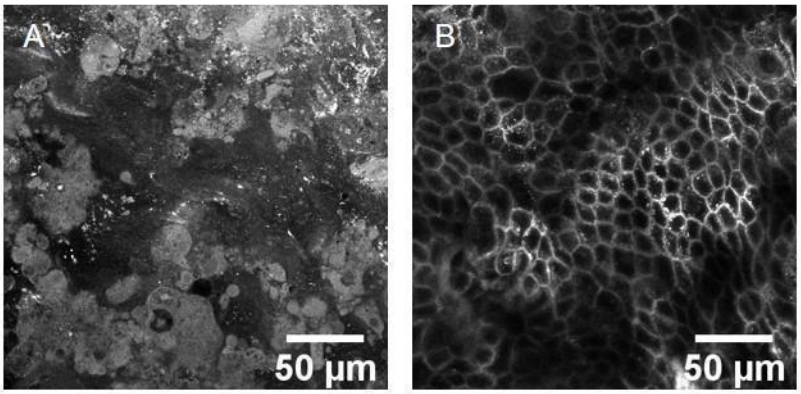

Supplementary Figure S5.1: Basolateral staining of Calu-3 mucus with WGA-Rhod allows the morphological discrimination between A) extracellular mucus covering B) the cell layer.

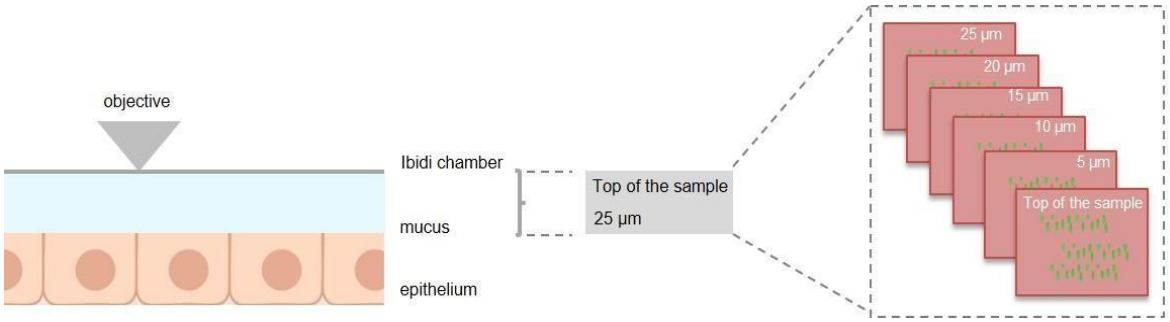

Supplementary Figure S5.2: Illustration that shows how imaging (using an inverted microscope) of particle penetration through the mucus layers was performed. Images were taken at different optical z-sections (every 5 µm) starting from the top of the mucus layer deeper to the underlying cell layer.

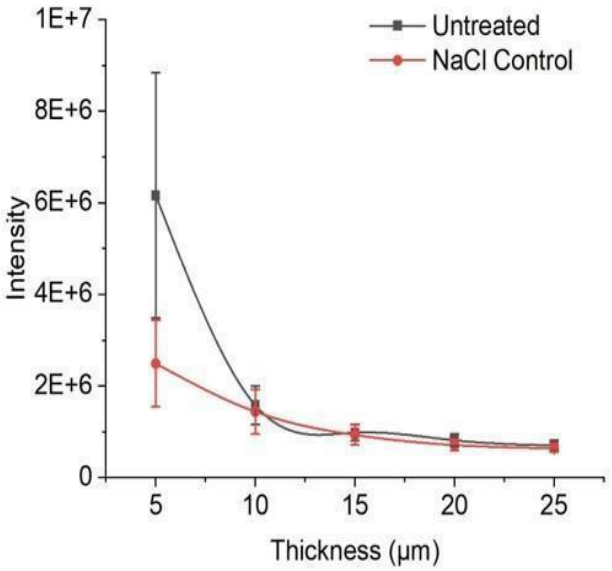

Supplementary Figure S5.3: Quantitative analysis of 500 nm particle penetration in untreated and 0.9% NaCl (used as a vehicle control for NAC) treated samples based on confocal imaging. Data shown are mean values ± SE for n=9 sample areas from 3 independent experiments.

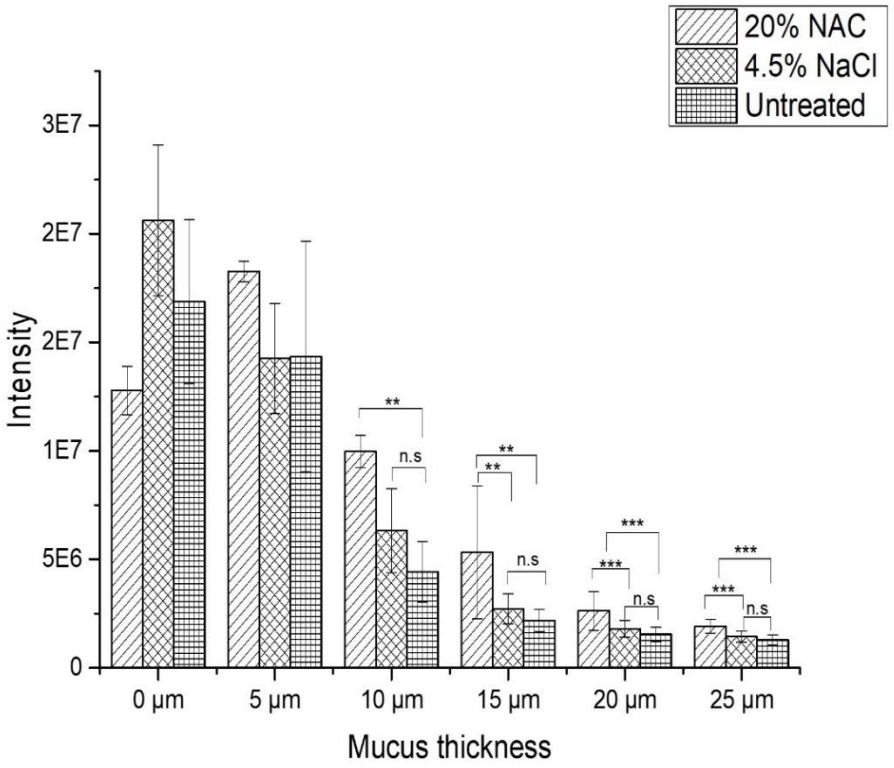

Supplementary Figure S5.4: Quantitative analysis of 500 nm particle penetration after treatment with 20% NAC and 4.5% NaCl based on confocal imaging. Data shown are mean values ± SE for n = 9 sample areas from 3 independent experiments. Statistical significance was calculated with One Way ANOVA followed by the Bonferroni test and indicated by asterisks: **, $p < 0.01$; ***, $p < 0.001$; n.s. non-significant.

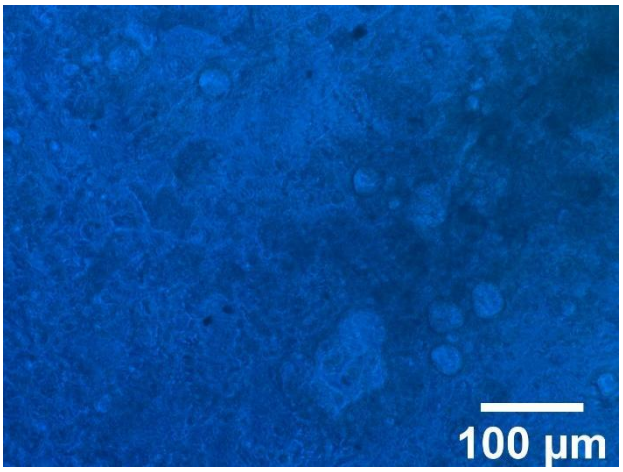

Supplementary Figure S5.5: Calu-3 cells form a confluent mucus layer. Light microscopy image of Calu-3 cells cultured for 21 days under air-interface conditions and stained with 1% Alcian blue.

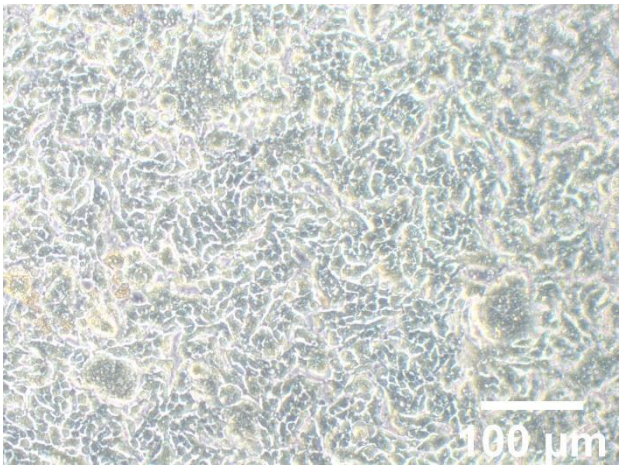

Supplementary Figure S5.6: Calu-3 cells form a confluent cell layer. Light microscopy image of Calu-3 cells cultured for 5 days under air-interface conditions.

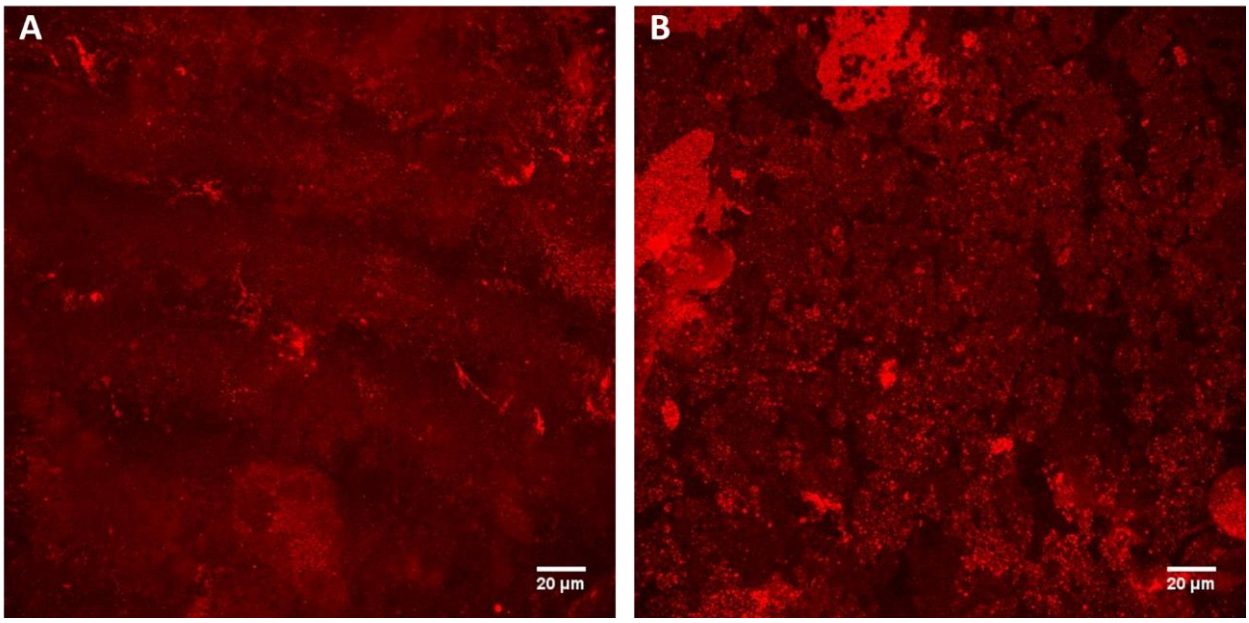

Supplementary Figure S5.7: Z-projections of Calu-3 mucus on A) day 21 and B) day 5, stained with WGA-Rhod. As the thickness of mucus was not uniform throughout the sample, providing areas with higher/lower mucus thickness, z-projections are shown (Image J). Images A and B are composite images that show a Maximum Intensity z-stacking.

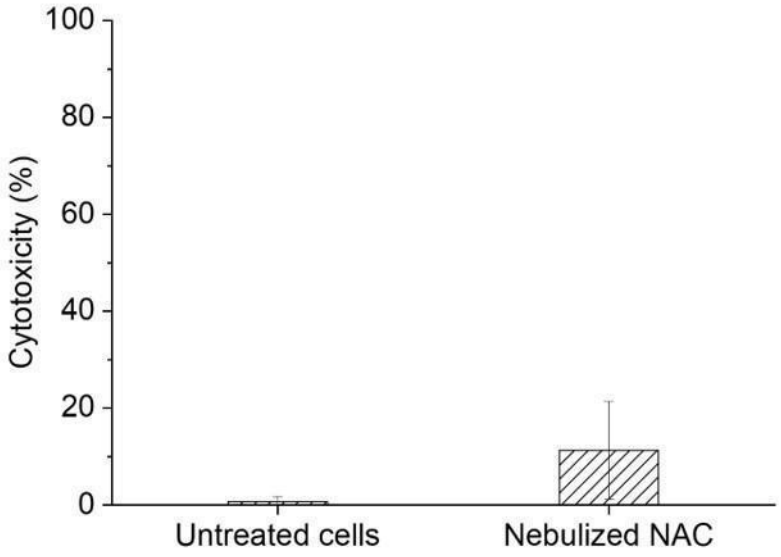

Supplementary Figure S5.8: NAC applied at a dose of 120 µg/cm^2 does not induce cytotoxicity (cytotoxicity < 20%). Prior to treatment, Calu-3 cells were cultured for 21 days under air-interface conditions.

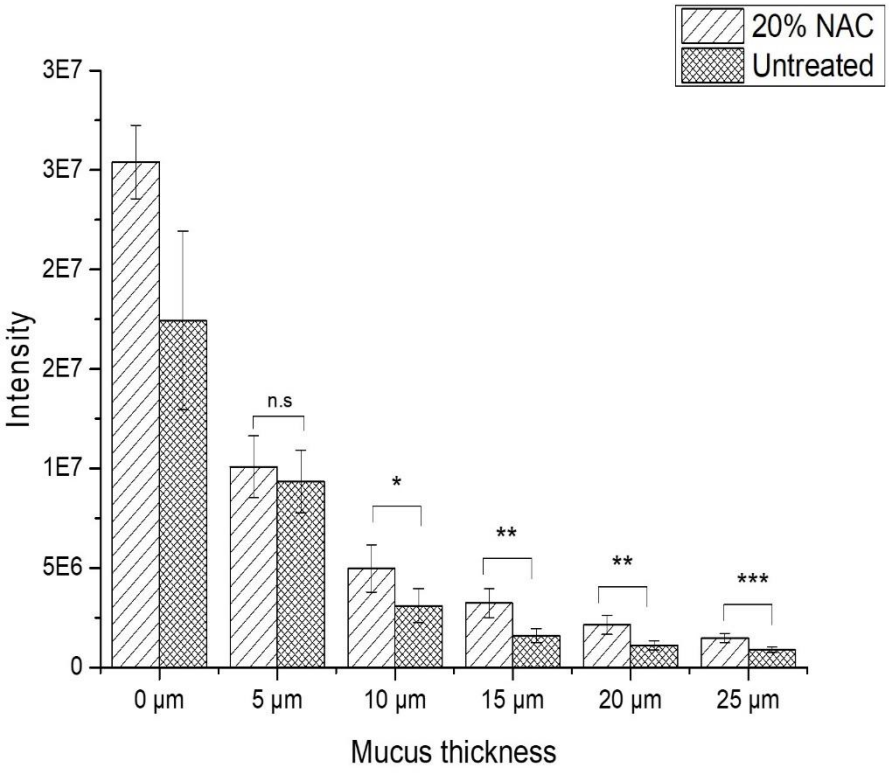

Supplementary Figure S5.9: Quantitative analysis of 100 nm particle penetration after treatment with 20% NAC based on confocal imaging. 100 nm NH_2-PS-NPs (see Table 5.1) were used. Data shown are mean values ± SE for n = 9 sample areas from 3 independent experiments. Statistical significance was calculated with One Way ANOVA followed by the Bonferroni test and indicated by asterisks: **, $p < 0.01$; ***, $p < 0.001$; n.s. non-significant.

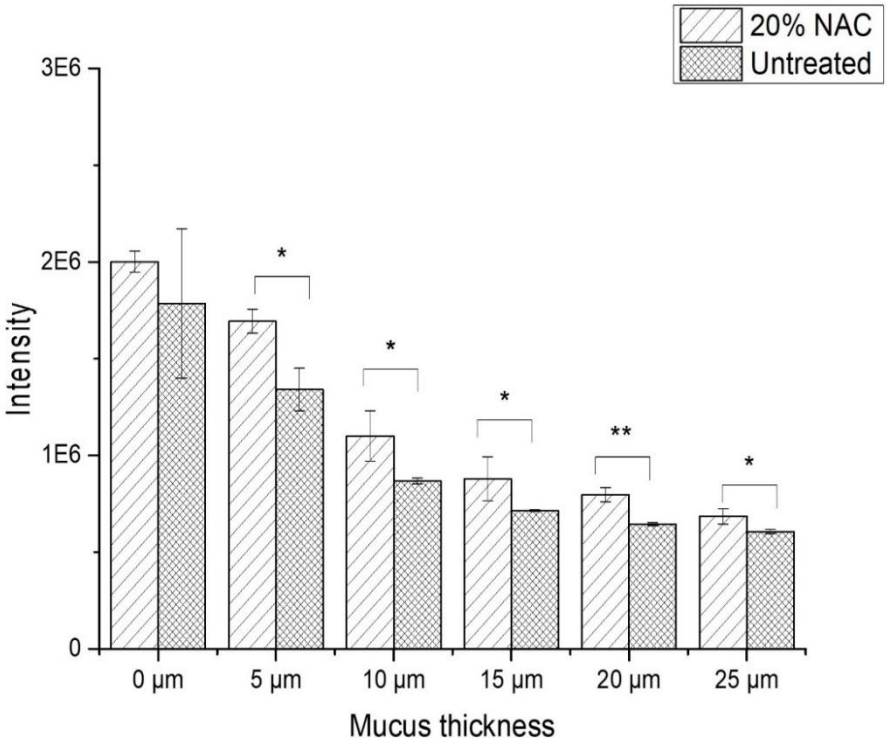

Supplementary Figure S5.10: Quantitative analysis of 50 nm COOH-PS-NPs penetration based on confocal imaging. Penetration was analyzed after treatment with 20% NAC and compared to untreated samples. Data shown are mean values ± SE for n = 6 sample areas from two independent experiments. Statistical significance was calculated with One Way ANOVA followed by the Bonferroni test and indicated by asterisks: *, $p < 0.05$; **, $p < 0.01$; n.s. non-significant. FluoSpheres (Invitrogen, Oregon, USA) were used for this analysis. The hydrodynamic diameter of the particles was 53 ± 9.5 nm. For DLS measurements, the particles were diluted in MilliQ water.

Supplementary Table S5.1: Osmolality of solutions used to treat Calu-3 mucus (day 21). The osmolality of these solutions was measured using the Osmomat 030 equipment (Gonotec GmbH, Bensheim, Germany). MQ- Milli Q.

Samples (% w/v)	Osmolality (osmol/kg)
Pure MQ water	0.000
NaCl 0.9% in MQ water	0.300
NaCl 4.5% in MQ water	1.447
20% NAC in 0.9% NaCl	1.459

6. Conclusion and outlook

The presented work investigated the structure of mucus, focused on the characterization of *in vitro* and *ex vivo* mucus models, and assessed the influence of mucus modulation as a mucus overcoming strategy on the barrier properties of mucus.

- This work aimed at the elucidation of the structure of native hydrated mucus. To the best of our knowledge, we could show for the first time that, in contrast to previous electron microscopy studies reporting a porous structure of mucus, in its hydrated state, mucus shows a rather non-porous compact structure. This was demonstrated using ESEM and high-resolution STED microscopy. *In situ* sublimation revealed that dehydration is responsible for the observed porous structure of mucus in electron microscopy. STED microscopy elucidated the nano-scale patterns of MUC5B as a major gel-forming mucin responsible for the gel properties of mucus. The CLSM data showed the heterogenous and composite structure of mucus. This work expands the knowledge about the structure of mucus and introduces STED microscopy as a tool for mucus nanoparticle research.

  Calu-3 *in vitro* mucus was characterized and compared to ETT *ex vivo* mucus. Features like mucin organization, concentration, rheology, mucus barrier, and metabolomic profile were assessed. The CLSM investigation of the structural organization of mucins showed that *in vitro* mucus is a less disturbed system than *ex vivo* mucus. *In vitro* mucus showed lower mucin concentration than *ex vivo* mucus. Macrorheology data demonstrated that *in vitro* mucus exhibits viscoelastic hydrogel properties with lower storage and loss moduli values than *ex vivo* mucus. Both mucus models showed similar barrier properties. Non-targeted metabolomic profiling of *in vitro* and *ex vivo* mucus showed that both mucus models differ from each other with significantly lower signal of the features (metabolites) for *in vitro* mucus, in particular for mucin and lipid content. The validation data provided in this work will help in the interpretation of experimental readouts obtained using Calu-3 *in vitro* mucus.

  Calu-3 *in vitro* mucus was used for the assessment of the impact of mucus modulation on the barrier function of mucus. Cultured under air-interface

conditions Calu-3 cells produced a physiologically relevant thick mucus layer, which was able to hinder the penetration of 500 nm COOH-PS-Ps particles. A mucus modulation protocol based on the aerosolized NAC, which allowed a significant enhancement of mucus penetration of 500 nm COOH-PS-Ps was developed. The protective function of mucus was probed by assessing the influence of 50 and 100 nm amine-modified and 50 nm carboxyl-modified polystyrene nanoparticles on the membrane integrity of Calu-3 cells. Intact Calu-3 *in vitro* mucus layer showed an effective protection for the underlying cells, which was reduced upon NAC treatment. We suggest that the assessment of the remaining mucus protection should be part of the development process for therapies involving modulation of the mucus layer.

- As a future perspective, the employment of dual color STED microscopy for the visualization of both gel-forming mucins MUC5AC and MUC5B would be of interest. This would provide valuable information regarding the intracellular distribution of these mucins and their morphology in the extracellular mucus, which is essential for understanding of the pathophysiology of mucin secretion related diseases. In addition, dual color STED microscopy could be employed for the simultaneous visualization of mucus and microparticles (composed of nanoparticles with a sub-diffraction limit size). The investigation of the disintegration of microparticles into nanoparticles in mucus and their cellular internalization would provide valuable information in the understanding of nanoparticle interactions with mucosal barriers.

  Calu-3 *in vitro* mucus is validated here by comparing it to *ex vivo* mucus, which is a commonly used mucus model, despite some reported shortcomings related to the collection procedure of this mucus model. Therefore, other mucus models which might encounter less alteration during the collection procedure like bronchoscopy samples or induced sputum should be taken into consideration for further investigation. Since the availability is the major problem regarding bronchoscopy and induced sputum samples, they might not be feasible for high-throughput experiments, however, they would provide valuable information regarding the human pulmonary mucus.

Inhalation therapy protocols comprising mucus modulation should involve an adjustment between the applied dose of mucus modulator and the protective function of mucus. In this context, the down titration of the NAC dose used in the mucus modulation protocol presented in this work would be of interest for the determination of the minimal required dose for a sufficient improvement of nanoparticle penetration. Furthermore, the investigation of the impact of mucus modulation on *in vitro* mucus models, that mimic mucus pathological conditions would be of interest in terms of translation of the data to the diseased mucus situations. Therefore, *e.g.*, an *in vitro* model using CFBE41o- cells complemented with CF sputum might be developed.

This thesis provides novel insights into the structure of native mucus, guides the application of the mucus models characterized here in the mucus nanoparticle interaction studies, and advances the knowledge about the safety aspect of the approach of mucus modulation.

7. References

[1] R. Bansil, B.S. Turner, Mucin structure, aggregation, physiological functions and biomedical applications, Curr. Opin. Colloid Interface Sci. 11 (2006) 164–170.

[2] M. Boegh, H.M. Nielsen, Mucus as a barrier to drug delivery - Understanding and mimicking the barrier properties, Basic Clin. Pharmacol. Toxicol. 116 (2015) 179–186.

[3] M.C. Rose, Respiratory Tract Mucin Genes and Mucin Glycoproteins in Health and Disease, Physiol. Rev. 86 (2006) 245–278.

[4] Z. Hong, B. Chasan, R. Bansil, B.S. Turner, K.R. Bhaskar, N.H. Afdhal, Atomic Force Microscopy Reveals Aggregation of Gastric Mucin at Low pH, Biomacromolecules. (2005) 3458–3466.

[5] J. Ma, B.K. Rubin, J.A. Voynow, Mucins, Mucus, and Goblet Cells, Chest. 154 (2018) 169–176.

[6] S.K. Lai, Y. Wang, D. Wirtz, J. Hanes, Micro- and macrorheology of mucus, Adv. Drug Deliv. Rev. 61 (2009) 86–100.

[7] G.A. Duncan, J. Jung, J. Hanes, J.S. Suk, The Mucus Barrier to Inhaled Gene Therapy, Mol. Ther. 24 (2016) 2043–2053.

[8] J. Kirch, A. Schneider, B. Abou, A. Hopf, U.F. Schaefer, M. Schneider, C. Schall, C. Wagner, C.-M. Lehr, Optical tweezers reveal relationship between microstructure and nanoparticle penetration of pulmonary mucus, Proc. Natl. Acad. Sci. 109 (2012) 18355–18360.

[9] J.S. Suk, S.K. Lai, Y.Y. Wang, L.M. Ensign, P.L. Zeitlin, M.P. Boyle, J. Hanes, The penetration of fresh undiluted sputum expectorated by cystic fibrosis patients by non-adhesive polymer nanoparticles, Biomaterials. 30 (2009) 2591–2597.

[10] S.K. Lai, Y.Y. Wang, J. Hanes, Mucus-penetrating nanoparticles for drug and gene delivery to mucosal tissues, Adv. Drug Deliv. Rev. 61 (2009) 158–171.

[11] B.S. Schuster, J.S. Suk, G.F. Woodworth, J. Hanes, Nanoparticle diffusion in respiratory mucus from humans without lung disease, Biomaterials. 34 (2013) 3439–3446.

[12] X. Murgia, P. Pawelzyk, U.F. Schaefer, C. Wagner, N. Willenbacher, C.M. Lehr, Size-Limited Penetration of Nanoparticles into Porcine Respiratory Mucus after Aerosol Deposition, Biomacromolecules. 17 (2016) 1536–1542.

[13] E. Meziu, M. Koch, J. Fleddermann, K. Schwarzkopf, M. Schneider, A. Kraegeloh, Visualization of the structure of native human pulmonary mucus, Int. J. Pharm. 597 (2021) 120238.

[14] J. Leal, H.D.C. Smyth, D. Ghosh, Physicochemical properties of mucus and their impact on transmucosal drug delivery, Int. J. Pharm. 532 (2017) 555–572.

[15] X. Murgia, B. Loretz, O. Hartwig, M. Hittinger, C.-M. Lehr, The role of mucus on drug transport and its potential to affect therapeutic outcomes, Adv. Drug Deliv. Rev. 124 (2018) 82–97.

[16] O. Lieleg, K. Ribbeck, Biological hydrogels as selective diffusion barriers, Trends Cell Biol. 21 (2011) 543–551.

[17] J. Kirch, M. Guenther, N. Doshi, U.F. Schaefer, M. Schneider, S. Mitragotri, C.M. Lehr, Mucociliary clearance of micro- and nanoparticles is independent of size, shape and charge-an ex vivo and in silico approach, J. Control. Release. 159 (2012) 128–134.

[18] E.P. Lillehoj, K. Kato, W. Lu, K.C. Kim, Cellular and Molecular Biology of Airway Mucins, Int. Rev. Cell Mol. Biol. 303 (2013) 139–202.

[19] H.D. Williams, V. Behrends, J.G. Bundy, B. Ryall, J.E.A. Zlosnik, Hypertonic saline therapy in cystic fibrosis: Do population shifts caused by the osmotic sensitivity of infecting bacteria explain the effectiveness of this treatment?, Front. Microbiol. 1 (2010) 1–5.

[20] B.K. Rubin, Mucus structure and properties in cystic fibrosis, Paediatr. Respir. Rev. 8 (2007) 4–7.

[21] M.O. Henke, G. John, M. Germann, H. Lindemann, B.K. Rubin, MUC5AC and MUC5B mucins increase in cystic fibrosis airway secretions during pulmonary exacerbation, Am. J. Respir. Crit. Care Med. 175 (2007) 816–821.

[22] J.A. Voynow, B.K.R. Mengr, Mucins, Mucus, and Sputum, Chest. 135 (2009) 505–512.

[23] J.Y. Lock, T.L. Carlson, R.L. Carrier, Mucus models to evaluate the diffusion of drugs and particles, Adv. Drug Deliv. Rev. 124 (2018) 34–49.

[24] M. Boegh, S.G. Baldursdottir, M.H. Nielsen, A. Müllertz, H.M. Nielsen, Development and Rheological Profiling of Biosimilar Mucus, Annu. Trans. Nord. Rheol. Soc. 21 (2013) 233–240.

[25] A.S. Critchfield, G. Yao, A. Jaishankar, R.S. Friedlander, O. Lieleg, P.S. Doyle, G. McKinley, M. House, K. Ribbeck, Cervical Mucus Properties Stratify Risk for Preterm Birth, PLoS One. 8 (2013) 2–8.

[26] X.M.R. Markovetz, D.B. Subramani, W.J. Kissner, C.B. Morrison, I.C. Garbarine, A. Ghio, K.A. Ramsey, H. Arora, P. Kumar, D.B. Nix, T. Kumagai, T.M. Krunkosky, D.C. Krause, G. Radicioni, N.E. Alexis, M. Kesimer, M. Tiemeyer, R.C. Boucher, C. Ehre, D.B. Hill, Endotracheal tube mucus as a source of airway mucus for rheological study, Am. J. Physiol. Lung Cell Mol. Physiol. 317 (2021) 498–509.

[27] A. Gross, A. Torge, U.F. Schaefer, M. Schneider, C.M. Lehr, C. Wagner, A foam model highlights the differences of the macro- and microrheology of respiratory horse mucus, J. Mech. Behav. Biomed. Mater. 71 (2017) 216–222.

[28] N. Lababidi, V. Sigal, A. Koenneke, K. Schwarzkopf, A. Manz, M. Schneider, Microfluidics as tool to prepare size-tunable PLGA nanoparticles with high curcumin encapsulation for efficient mucus penetration, Beilstein J. Nanotechnol. (2019) 2280–2293.

[29] B.K. Rubin, O. Ramirez, J.G. Zayas, B. Finegan, M. King, Collection and analysis of respiratory mucus from subjects without lung disease., Am. Rev. Respir. Dis. 141 (1990) 1040–3.

[30] X.M. C.M. Lehr, B. Loretz, O. Hartwig; M. Hittinger, The role of mucus on drug transport and its potential to affect therapeutic outcomes, Adv. Drug Deliv. Rev. 124 (2017) 82–97.

[31] B. Vukosavljevic, X. Murgia, K. Schwarzkopf, U.F. Schaefer, C. Lehr, M. Windbergs, Tracing molecular and structural changes upon mucolysis with N-acetyl cysteine in human airway mucus, Int. J. Pharm. 533 (2017) 373–376.

[32] N.N. Sanders, S.C. De Smedt, E. Van Rompaey, P. Simoens, F. De Baets, J. Demeester, Cystic fibrosis sputum: A barrier to the transport of nanospheres, Am. J. Respir. Crit. Care Med. 162 (2000) 1905–1911.

[33] A. Macierzanka, A.R. Mackie, L. Krupa, Permeability of the small intestinal mucus for physiologically relevant studies: Impact of mucus location and ex vivo treatment, Sci. Rep. 9 (2019) 1–12.

[34] A.G. Henderson, C. Ehre, B. Button, L.H. Abdullah, L.H. Cai, M.W. Leigh, G.C. DeMaria, H. Matsui, S.H. Donaldson, C.W. Davis, J.K. Sheehan, R.C. Boucher, M. Kesimer, Cystic fibrosis airway secretions exhibit mucin hyperconcentration and increased osmotic pressure, J. Clin. Invest. 124 (2014) 3047–3060.

[35] R. Hamed, J. Fiegel, Synthetic tracheal mucus with native rheological and surface tension properties, J. Biomed. Mater. Res. - Part A. 102 (2014) 1788–1798.

[36] J.S. Crater, R.L. Carrier, Barrier Properties of Gastrointestinal Mucus to Nanoparticle Transport, Macromol. Biosci. 10 (2010) 1473–1483.

[37] M. Boegh, S.G. Baldursdóttir, A. Müllertz, H.M. Nielsen, Property profiling of biosimilar mucus in a novel mucus-containing in vitro model for assessment of intestinal drug absorption, Eur. J. Pharm. Biopharm. 87 (2014) 227–235.

[38] B.C. Huck, O. Hartwig, A. Biehl, K. Schwarzkopf, C. Wagner, B. Loretz, X. Murgia, C.-M. Lehr, Macro- and Microrheological Properties of Mucus Surrogates in Comparison to Native Intestinal and Pulmonary Mucus, Biomacromolecules. 20 (2019) 3504–3512.

[39] S. Frisch, A. Boese, B. Huck, J.C. Horstmann, D.-K. Ho, K. Schwarzkopf, X. Murgia, B. Loretz, C. de Souza Carvalho-Wodarz, C.-M. Lehr, A pulmonary mucus surrogate for investigating antibiotic permeation and activity against Pseudomonas aeruginosa biofilms , J. Antimicrob. Chemother. 76 (2021) 1472–1479.

[40] M. Jory, K. Bellouma, C. Blanc, L. Casanellas, A. Petit, P. Reynaud, C. Vernisse, I. Vachier, A. Bourdin, G. Massiera, Mucus Microrheology Measured on Human Bronchial Epithelium Culture, Front. Phys. 7 (2019) 19.

[41] B. Button, L.-H. Cai, C. Ehre, M. Kesimer, D.B. Hill, J.K. Sheehan, R.C. Boucher, M. Rubinstein, A periciliary brush promotes the lung health by separating the mucus layer from airway epithelia., Science. 337 (2012) 937–941.

[42] F. Carlini, C. Picard, C. Garulli, D. Piquemal, P. Roubertoux, J. Chiaroni, P. Chanez, D. Gras, J. Di Cristofaro, Bronchial epithelial cells from asthmatic patients display less functional HLA-G isoform expression, Front. Immunol. 8 (2017) 6.

[43] S.M. Kreda, S.F. Okada, C.A. Van Heusden, W. O'neal, S. Gabriel, L. Abdullah, C.W. Davis, R.C. Boucher, E.R. Lazarowski, Coordinated release of nucleotides and mucin from human airway epithelial Calu-3 cells, J. Physiol. 584 (2007) 245–259.

[44] R. Ghanem, V. Laurent, P. Roquefort, T. Haute, S. Ramel, T. Le Gall, T. Aubry, T. Montier, Optimizations of in vitro mucus and cell culture models to better predict in vivo gene transfer in pathological lung respiratory airways: Cystic fibrosis as an example, Pharmaceutics. 13 (2021) 1–25.

[45] M.E. Kreft, U.D. Jerman, E. Lasič, N. Hevir-Kene, T.L. Rižner, L. Peternel, K. Kristan, The characterization of the human cell line Calu-3 under different culture conditions and its use as an optimized in vitro model to investigate bronchial epithelial function, Eur. J. Pharm. Sci. 69 (2015) 1–9.

[46] C. Haws, W.E. Finkbeiner, J.H. Widdicombe, J.J. Wine, J. Wine, CFTR in Calu-3 human airway cells : channel properties and role in cAMP-activated Cl- conductance, Am. J. Physiol. 266 (1994) L502–L512.

[47] B. Forbes, A. Shah, G.P. Martin, A.B. Lansley, The human bronchial epithelial cell line 16HBE14o- as a model system of the airways for studying drug transport, Int. J. Pharm. 257 (2003) 161–167.

[48] C. Ehrhardt, C. Kneuer, J. Fiegel, J. Hanes, U. Schaefer, K.J. Kim, C.M. Lehr, Influence of apical fluid volume on the development of functional intercellular junctions in the human epithelial cell line 16HBE14o-: Implications for the use of this cell line as an in vitro model for bronchial drug absorption studies, Cell Tissue Res. 308 (2002) 391–400.

[49] A. Henning, M. Schneider, M. Bur, F. Blank, P. Gehr, C.-M. Lehr, Embryonic Chicken Trachea as a New In Vitro Model for the Investigation of Mucociliary Particle Clearance in the Airways, AAPS PharmSciTech. 9 (2008) 521–527.

[50] P. V Turner, T. Brabb, C. Pekow, M.A. Vasbinder, Administration of Substances to Laboratory Animals : Routes of Administration and Factors to Consider, J. Am. Assoc. Lab.

Anim. Sci. 50 (2011) 600–613.

[51] N. Nafee, K. Forier, K. Braeckmans, M. Schneider, Mucus-penetrating solid lipid nanoparticles for the treatment of cystic fibrosis: Proof of concept, challenges and pitfalls, Eur. J. Pharm. Biopharm. 124 (2018) 125–137.

[52] J.S. Suk, N.J. Boylan, K. Trehan, B.C. Tang, C.S. Schneider, J.M.G. Lin, M.P. Boyle, P.L. Zeitlin, S.K. Lai, M.J. Cooper, J. Hanes, N-acetylcysteine enhances cystic fibrosis sputum penetration and airway gene transfer by highly compacted DNA nanoparticles, Mol. Ther. 19 (2011) 1981–1989.

[53] J. Ernst, M. Klinger-Strobel, K. Arnold, J. Thamm, A. Hartung, M.W. Pletz, O. Makarewicz, D. Fischer, Polyester-based particles to overcome the obstacles of mucus and biofilms in the lung for tobramycin application under static and dynamic fluidic conditions, Eur. J. Pharm. Biopharm. 131 (2018) 120–129.

[54] X. Murgia, H. Yasar, C. Carvalho-wodarz, B. Loretz, S. Gordon, K. Schwarzkopf, U. Schaefer, C. Lehr, European Journal of Pharmaceutics and Biopharmaceutics Modelling the bronchial barrier in pulmonary drug delivery : A human bronchial epithelial cell line supplemented with human tracheal mucus, Eur. J. Pharm. Biopharm. 118 (2017) 79–88.

[55] I. Pereira De Sousa, C. Steiner, M. Schmutzler, M.D. Wilcox, G.J. Veldhuis, J.P. Pearson, C.W. Huck, W. Salvenmoser, A. Bernkop-Schnürch, Mucus permeating carriers: formulation and characterization of highly densely charged nanoparticles, Eur. J. Pharm. Biopharm. 97 (2015) 273–279.

[56] N. Nafee, A. Husari, C.K. Maurer, C. Lu, C. De Rossi, A. Steinbach, R.W. Hartmann, C.M. Lehr, M. Schneider, Antibiotic-free nanotherapeutics: Ultra-small, mucus-penetrating solid lipid nanoparticles enhance the pulmonary delivery and anti-virulence efficacy of novel quorum sensing inhibitors, J. Control. Release. 192 (2014) 131–140.

[57] C. Müller, G. Perera, V. König, A. Bernkop-Schnürch, Development and in vivo evaluation of papain-functionalized nanoparticles, Eur. J. Pharm. Biopharm. 87 (2014) 125–131.

[58] H. Friedl, S. Dünnhaupt, F. Hintzen, C. Waldner, S. Parikh, J.P. Pearson, M.D. Wilcox, A. Bernkop-Schnürch, Development and evaluation of a novel mucus diffusion test system approved by self-nanoemulsifying drug delivery Systems, J. Pharm. Sci. 102 (2013) 4406–4413.

[59] A. Torge, S. Wagner, P.S. Chaves, E.G. Oliveira, S.S. Guterres, A.R. Pohlmann, A. Titz, M. Schneider, R.C.R. Beck, Ciprofloxacin-loaded lipid-core nanocapsules as mucus penetrating drug delivery system intended for the treatment of bacterial infections in cystic fibrosis, Int. J. Pharm. 527 (2017) 92–102.

[60] D.A. Norris, P.J. Sinko, Effect of Size, Surface Charge, and Hydrophobicity on the

Translocation of Polystyrene Microspheres Through Gastrointestinal Mucin, J. Appl. Polym. Sci. 63 (1997) 1481–1492.

[61] K. Khanvilkar, M.D. Donovan, D.R. Flanagan, Drug transfer through mucus, Adv. Drug Deliv. Rev. 48 (2001) 173–193.

[62] P.G. Bhat, D.R. Flanagan, M.D. Donovan, The limiting role of mucus in drug absorption: Drug permeation through mucus solution, Int. J. Pharm. 126 (1995) 179–187.

[63] P.G. Bhat, D.R. Flanagan, M.D. Donovan, The limiting role of mucus in drug absorption: Drug permeation through mucus solution, Int. J. Pharm. 126 (1995) 179–187.

[64] S. Dünnhaupt, J. Barthelmes, J. Hombach, D. Sakloetsakun, V. Arkhipova, A. Bernkop-Schnürch, Distribution of thiolated mucoadhesive nanoparticles on intestinal mucosa, Int. J. Pharm. 408 (2011) 191–199.

[65] N. Nafee, M. Schneider, Towards a versatile technique for tracking nanoparticle-mucus interaction: a step on the road, Nanoscale Imaging, Sensing, Actuation Biomed. Appl. XI. 8954 (2014) 89540J.

[66] S.S. Olmsted, J.L. Padgett, A.I. Yudin, K.J. Whaley, T.R. Moench, R.A. Cone, Diffusion of macromolecules and virus-like particles in human cervical mucus, Biophys. J. 81 (2001) 1930–1937.

[67] J. Grießinger, S. Dünnhaupt, B. Cattoz, P. Griffiths, S. Oh, S.B.I. Gómez, M. Wilcox, J. Pearson, M. Gumbleton, M. Abdulkarim, I. Pereira De Sousa, A. Bernkop-Schnürch, Methods to determine the interactions of micro- and nanoparticles with mucus, Eur. J. Pharm. Biopharm. 96 (2015) 464–476.

[68] R. Bansil, B.S. Turner, The biology of mucus : Composition , synthesis and organization, Adv. Drug Deliv. Rev. 124 (2018) 3–15.

[69] R.A. Cone, Barrier properties of mucus, Adv. Drug Deliv. Rev. 61 (2009) 75–85.

[70] A. Henning, S. Hein, M. Schneider, M. Bur, C.-M. Lehr, Pulmonary Drug Delivery: Medicines for Inhalation, Handb. Exp. Pharmacol. 197 (2010) 171–92.

[71] O. Lieleg, I. Vladescu, K. Ribbeck, Characterization of particle translocation through mucin hydrogels, Biophys. J. 98 (2010) 1782–1789.

[72] S.K. Lai, D.E. O'Hanlon, S. Harrold, S.T. Man, Y.-Y. Wang, R. Cone, J. Hanes, Rapid transport of large polymeric nanoparticles in fresh undiluted human mucus, Proc. Natl. Acad. Sci. 104 (2007) 1482–1487.

[73] B.S. Schuster, D.B. Allan, J.C. Kays, J. Hanes, R.L. Leheny, Photoactivatable fluorescent probes reveal heterogeneous nanoparticle permeation through biological gels at multiple scales, J. Control. Release. 260 (2017) 124–133.

[74] M. Dawson, D. Wirtz, J. Hanes, Enhanced Viscoelasticity of Human Cystic Fibrotic Sputum

Correlates with Increasing Microheterogeneity in Particle Transport, J. Biol. Chem. 278 (2003) 50393–50401.

[75] X. Yang, K. Forier, L. Steukers, S. van Vlierberghe, P. Dubruel, K. Braeckmans, S. Glorieux, H.J. Nauwynck, Immobilization of Pseudorabies Virus in Porcine Tracheal Respiratory Mucus Revealed by Single Particle Tracking, PLoS One. 7 (2012) e51054.

[76] C.R. Esther, M.S. Muhlebach, C. Ehre, D.B. Hill, M.C. Wolfgang, M. Kesimer, K.A. Ramsey, M.R. Markovetz, I.C. Garbarine, M. Gregory Forest, I. Seim, B. Zorn, C.B. Morrison, M.F. Delion, W.R. Thelin, D. Villalon, J.R. Sabater, L. Turkovic, S. Ranganathan, S.M. Stick, R.C. Boucher, Mucus accumulation in the lungs precedes structural changes and infection in children with cystic fibrosis, Sci. Transl. Med. 11 (2019) eaav3488.

[77] C. Efthymiou, M.A.K. Williams, K.M. Mcgrath, Revealing the structure of high-water content biopolymer networks : Diminishing freezing artefacts in cryo-SEM images, Food Hydrocoll. 73 (2017) 203–212.

[78] H. Ensikat, M. Weigend, Cryo-scanning electron microscopy of plant samples without metal coating , utilizing bulk conductivity, Microsc. Anal. 27 (2013) 7–10.

[79] M. Koch, M.K. Włodarczyk-Biegun, Faithful scanning electron microscopic (SEM) visualization of 3D printed alginate-based scaffolds, Bioprinting. 20 (2020) e00098.

[80] D.J. Stokes, F.E.I. Company, Environmental scanning electron microscopy for biology and polymer science, Microsc. Microanal. 26 (2012) 67–71.

[81] A.M. Donald, The use of environmental scanning electron microscopy for imaging wet and insulating materials, Nat. Mater. 2 (2003) 511–516.

[82] H. Peuschel, T. Ruckelshausen, C. Cavelius, A. Kraegeloh, Quantification of Internalized Silica Nanoparticles via STED Microscopy, Biomed Res. Int. 2015 (2015) 961208.

[83] R. Aston, K. Sewell, T. Klein, G. Lawrie, L. Grøndahl, Evaluation of the impact of freezing preparation techniques on the characterisation of alginate hydrogels by cryo-SEM, Eur. Polym. J. 82 (2016) 1–15.

[84] E.M. Ivan'kova, I.P. Dobrovolskaya, P. V. Popryadukhin, A. Kryukov, V.E. Yudin, P. Morganti, In-situ cryo-SEM investigation of porous structure formation of chitosan sponges, Polym. Test. 52 (2016) 41–45.

[85] Y. Hasegawa, J.L. Mark Welch, B.J. Rossetti, G.G. Borisy, Preservation of three-dimensional spatial structure in the gut microbiome, PLoS One. 11 (2017) e0188257.

[86] L.S. Ostedgaard, T.O. Moninger, J.D. McMenimen, N.M. Sawin, C.P. Parker, I.M. Thornell, L.S. Powers, N.D. Gansemer, D.C. Bouzek, D.P. Cook, D.K. Meyerholz, M.H. Abou Alaiwa, D.A. Stoltz, M.J. Welsh, Gel-forming mucins form distinct morphologic structures in airways, Proc. Natl. Acad. Sci. U. S. A. 114 (2017) 6842–6847.

[87] W.J. Janssen, A.L. Stefanski, B.S. Bochner, C.M. Evans, Control of lung defence by mucins and macrophages : ancient defence mechanisms with modern functions, Eur. Respir. J. 48 (2016) 1201–1214.

[88] W.M. Saltzman, M.L. Radomsky, K.J. Whaley, R.A. Cone, Antibody diffusion in human cervical mucus, Biophys. J. 66 (1994) 508–515.

[89] B.H. Bajka, N.M. Rigby, K.L. Cross, A. Macierzanka, A.R. Mackie, Biointerfaces The influence of small intestinal mucus structure on particle transport ex vivo, Colloids Surfaces B Biointerfaces. 135 (2015) 73–80.

[90] J.D. Smart, The basics and underlying mechanisms of mucoadhesion, Adv. Drug Deliv. Rev. 57 (2005) 1556–1568.

[91] J. Ma, B.K. Rubin, J.A. Voynow, Mucins , Mucus , and Goblet Cells, Chest. 154 (2018) 169–176.

[92] A. Macierzanka, A.R. Mackie, B.H. Bajka, N.M. Rigby, F. Nau, D. Dupont, Transport of particles in intestinal mucus under simulated infant and adult physiological conditions: Impact of mucus structure and extracellular DNA, PLoS One. 9 (2014) 1–11.

[93] D. Song, D. Cahn, G.A. Duncan, Mucin Biopolymers and Their Barrier Function at Airway Surfaces, Langmuir. 36 (2020) 12773–12783.

[94] Y. Cu, W.M. Saltzman, Controlled surface modification with poly(ethylene)glycol enhances diffusion of PLGA nanoparticles in human cervical Mucus, Mol. Pharm. 6 (2009) 173–181.

[95] Z. Izadifar, A. Sontheimer-Phelps, B.A. Lubamba, H. Bai, C. Fadel, A. Stejskalova, A. Ozkan, Q. Dasgupta, A. Bein, A. Junaid, A. Gulati, G. Mahajan, S. Kim, N.T. LoGrande, A. Naziripour, D.E. Ingber, Modeling mucus physiology and pathophysiology in human organs-on-chips, Adv. Drug Deliv. Rev. 191 (2022) 114542.

[96] C. Gamazo, N. Martin-Arbella, A. Brotons, A.I. Camacho, J.M. Irache, Mimicking microbial strategies for the design of mucus-permeating nanoparticles for oral immunization, Eur. J. Pharm. Biopharm. 96 (2015) 454–463.

[97] K.A. Foster, M.L. Avery, M. Yazdanian, K.L. Audus, Characterization of the Calu-3 cell line as a tool to screen pulmonary drug delivery, Int. J. Pharm. 208 (2000) 1–11.

[98] E. Meziu, K. Shehu, M. Koch, M. Schneider, A. Kraegeloh, Impact of mucus modulation by N-acetylcysteine on nanoparticle toxicity, Int. J. Pharm. X. 6 (2023) 100212.

[99] M. Kilcoyne, J.Q. Gerlach, M.P. Farrell, V.P. Bhavanandan, L. Joshi, Periodic acid-Schiff's reagent assay for carbohydrates in a microtiter plate format, Anal. Biochem. 416 (2011) 18–26.

[100] H.I. Labouta, T. Kraus, L.K. El-Khordagui, M. Schneider, Combined multiphoton imaging-pixel analysis for semiquantitation of skin penetration of gold nanoparticles, Int. J. Pharm.

413 (2011) 279–282.

[101] S. Hemmer, L. Wagmann, M.R. Meyer, Altered metabolic pathways elucidated via untargeted in vivo toxicometabolomics in rat urine and plasma samples collected after controlled application of a human equivalent amphetamine dose, Arch. Toxicol. 95 (2021) 3223–3234.

[102] S.K. Manier, L. Wagmann, V. Flockerzi, M.R. Meyer, Toxicometabolomics of the new psychoactive substances α-PBP and α-PEP studied in HepaRG cell incubates by means of untargeted metabolomics revealed unexpected amino acid adducts, Arch. Toxicol. 94 (2020) 2047–2059.

[103] J.R. Landis, G.G. Koch, The Measurement of Observer Agreement for Categorical Data, Biometrics. 33 (1977) 159–174.

[104] G. Ruiz-Pulido, D.I. Medina, An overview of gastrointestinal mucus rheology under different pH conditions and introduction to pH-dependent rheological interactions with PLGA and chitosan nanoparticles, Eur. J. Pharm. Biopharm. 159 (2021) 123–136.

[105] E.S. Vasquez, J. Bowser, C. Swiderski, K.B. Walters, S. Kundu, Rheological characterization of mammalian lung mucus, RSC Adv. 4 (2014) 34780–34783.

[106] M. Boegh, S.G. Baldursdóttir, A. Müllertz, H.M. Nielsen, Property profiling of biosimilar mucus in a novel mucus-containing in vitro model for assessment of intestinal drug absorption, Eur. J. Pharm. Biopharm. 87 (2014) 227–235.

[107] L.D. Roberts, A.L. Souza, R.E. Gerszten, C.B. Clish, Targeted metabolomics, Curr. Protoc. Mol. Biol. 30.2 (2012) 1–24.

[108] J.E. Wolak, C.R. Esther, T.M. O'Connell, Metabolomic analysis of bronchoalveolar lavage fluid from cystic fibrosis patients, Biomarkers. 14 (2009) 55–60.

[109] T. Zhu, S. Li, J. Wang, C. Liu, L. Gao, Y. Zeng, R. Mao, B. Cui, H. Ji, Z. Chen, Induced sputum metabolomic profiles and oxidative stress are associated with chronic obstructive pulmonary disease (COPD) severity: potential use for predictive, preventive, and personalized medicine, EPMA J. 11 (2020) 645–659.

[110] M.C. McKelvey, R. Brown, S. Ryan, M.A. Mall, S. Weldon, C.C. Taggart, Proteases, mucus, and mucosal immunity in chronic lung disease, Int. J. Mol. Sci. 22 (2021) 5018.

[111] A. Steckel, G. Schlosser, An organic chemist's guide to electrospray mass spectrometric structure elucidation, Molecules. 24 (2019) 1–11.

[112] B. Huck, A. Hidalgo, F. Waldow, D. Schwudke, K.I. Gaede, C. Feldmann, P. Carius, C. Autilio, J. Pérez-gil, K. Schwarzkopf, X. Murgia, B. Loretz, C. Lehr, Systematic Analysis of Composition , Interfacial Performance and Effects of Pulmonary Surfactant Preparations on Cellular Uptake and Cytotoxicity of Aerosolized Nanomaterials, Small Sci. 10 (2021) 19436.

[113] Y.-L. Cheng, C.-Y. Lee, Y.-L. Huang, C.A. Buckner, R.M. Lafrenie, J.A. Dénommée, J.M. Caswell, D.A. Want, G.G. Gan, Y.C. Leong, P.C. Bee, E. Chin, A.K.H. Teh, S. Picco, L. Villegas, F. Tonelli, M. Merlo, J. Rigau, D. Diaz, M. Masuelli, S. Korrapati, P. Kurra, S. Puttugunta, S. Picco, L. Villegas, F. Tonelli, M. Merlo, J. Rigau, D. Diaz, M. Masuelli, M. Tascilar, F.A. de Jong, J. Verweij, R.H.J. Mathijssen, In Vitro Assessment of Chronic Nanoparticle Effects on Respiratory Cells, Nanomater. - Toxic. Risk Assess. Prep. 11 (2016) 69–91.

[114] P.I. Chater, M.D. Wilcox, J.P. Pearson, Efficacy and safety concerns over the use of mucus modulating agents for drug delivery using nanoscale systems, Adv. Drug Deliv. Rev. 124 (2018) 184–192.

[115] C.T. Nordgård, K.I. Draget, Co association of mucus modulating agents and nanoparticles for mucosal drug delivery, Adv. Drug Deliv. Rev. 124 (2018) 175–183.

[116] J.S. Suk, S.K. Lai, N.J. Boylan, M.R. Dawson, M.P. Boyle, J. Hanes, Rapid transport of muco-inert nanoparticles in cystic fibrosis sputum treated with *N* -acetyl cysteine, Nanomedicine. 6 (2011) 365–375.

[117] T.L. Carlson, J.Y. Lock, R.L. Carrier, Engineering the Mucus Barrier, Annu. Rev. Biomed. Eng. 20 (2018) 197–220.

[118] A.D. Vethaak, J. Legler, Microplastics and human health., Science. 371 (2021) 672–674.

[119] T. Wu, M. Täubel, R. Holopainen, A.K. Viitanen, S. Vainiotalo, T. Tuomi, J. Keskinen, A. Hyvärinen, K. Hämeri, S.E. Saari, B.E. Boor, Infant and Adult Inhalation Exposure to Resuspended Biological Particulate Matter, Environ. Sci. Technol. 52 (2018) 237–247.

[120] W. Xia, Y. Wang, S. Chen, J. Huang, B. Wang, G.J. Zhang, Y. Zhang, X. Liu, J. Ma, P. Gong, Y. Jiang, M. Wu, J. Xue, L. Wei, T. Zhang, Double Trouble of Air Pollution by Anthropogenic Dust, Environ. Sci. Technol. 56 (2022) 761–769.

[121] A. Jachak, S.K. Lai, K. Hida, J.S. Suk, N. Markovic, S. Biswal, P.N. Breysse, J. Hanes, Transport of metal oxide nanoparticles and single-walled carbon nanotubes in human mucus, Nanotoxicology. 6 (2012) 614–622.

[122] Y.Y. Wang, S.K. Lai, C. So, C. Schneider, R. Cone, J. Hanes, Mucoadhesive nanoparticles may disrupt the protective human mucus barrier by altering its microstructure, PLoS One. 6 (2011) 1–7.

[123] T. Sonntag, M. Rapp, P. Didier, L. Lebeau, F. Pons, A. Casset, Mucus-producing epithelial models for investigating the activity of gene delivery systems in the lung, Int. J. Pharm. 614 (2022) 121423.

[124] J. Fogh, J.M. Fogh, T. Orfeo, One hundred and twenty-seven cultured human tumor cell lines producing tumors in nude mice, J. Natl. Cancer Inst. 59 (1977) 221–226.

[125] M. Haghi, D. Traini, P. Young, In vitro cell integrated impactor deposition methodology for

the study of aerodynamically relevant size fractions from commercial pressurised metered dose inhalers, Pharm. Res. 31 (2014) 1779–1787.

[126] J. Juntke, X. Murgia, N. Günday Türeli, A.E. Türeli, C.R. Thorn, M. Schneider, N. Schneider-Daum, C. de Souza Carvalho-Wodarz, C.M. Lehr, Testing of aerosolized ciprofloxacin nanocarriers on cystic fibrosis airway cells infected with P. aeruginosa biofilms, Drug Deliv. Transl. Res. 11 (2021) 1752–1765.

[127] Y. Ding, P. Weindl, A.G. Lenz, P. Mayer, T. Krebs, O. Schmid, Quartz crystal microbalances (QCM) are suitable for real-time dosimetry in nanotoxicological studies using VITROCELL®Cloud cell exposure systems, Part. Fibre Toxicol. 17 (2020) 44.

[128] T.C. Carvalho, J.I. Peters, R.O. Williams, Influence of particle size on regional lung deposition – What evidence is there ?, Int. J. Pharm. 406 (2011) 1–10.

[129] H.-Y. Tseng, H.-L. Lin, H.-S. Chiang, In Vitro Evaluation of Aerosol Delivery by Hand-Held Mesh Nebulizers in an Adult Spontaneous Breathing Lung Model., J. Aerosol Med. Pulm. Drug Deliv. 35 (2022) 83–90.

[130] B. Rothen-Rutishauser, M. Gibb, R. He, A. Petri-Fink, C.M. Sayes, Human lung cell models to study aerosol delivery – considerations for model design and development, Eur. J. Pharm. Sci. 180 (2023) 106337.

[131] D. Song, E. Iverson, L. Kaler, A. Boboltz, M.A. Scull, G.A. Duncan, MUC5B mobilizes and MUC5AC spatially aligns mucociliary transport on human airway epithelium, Sci. Adv. 8 (2022) eabq5049.

[132] J.T. Berger, J.A. Voynow, K.W. Peters, M.C. Rose, Respiratory carcinoma cell lines MUC genes and glycoconjugates, Am. J. Respir. Cell Mol. Biol. 20 (1999) 500–510.

[133] A.G. Henderson, C. Ehre, B. Button, L.H. Abdullah, L.H. Cai, M.W. Leigh, G.C. DeMaria, H. Matsui, S.H. Donaldson, C.W. Davis, J.K. Sheehan, R.C. Boucher, M. Kesimer, Cystic fibrosis airway secretions exhibit mucin hyperconcentration and increased osmotic pressure, J. Clin. Invest. 124 (2014) 3047–3060.

[134] D.B. Hill, R.F. Long, W.J. Kissner, E. Atieh, I.C. Garbarine, M.R. Markovetz, N.C. Fontana, M. Christy, M. Habibpour, R. Tarran, M. Gregory Forest, R.C. Boucher, B. Button, Pathological mucus and impaired mucus clearance in cystic fibrosis patients result from increased concentration, not altered pH, Eur. Respir. J. 52 (2018) 1801297.

[135] M.D. Richard C. Boucher, Muco-Obstructive Lung Diseases, N. Engl. J. Med. 380 (2019) 1941–1953.

[136] S. Mura, H. Hillaireau, J. Nicolas, B. Le Droumaguet, C. Gueutin, N. Tsapis, E. Fattal, Influence of surface charge on the potential toxicity of PLGA nanoparticles towards Calu-3 cells, Int .J. Nanomedicine. 6 (2011) 2591–2605.

[137] C.I. Grainger, L.L. Greenwell, D.J. Lockley, G.P. Martin, B. Forbes, Culture of Calu-3 cells at the air interface provides a representative model of the airway epithelial barrier, Pharm. Res. 23 (2006) 1482–1490.

[138] A. Stentebjerg-Andersen, I.V. Notlevsen, B. Brodin, C.U. Nielsen, Calu-3 cells grown under AIC and LCC conditions: Implications for dipeptide uptake and transepithelial transport of substances, Eur. J. Pharm. Biopharm. 78 (2011) 19–26.

[139] H. Wan, H.L. Winton, C. Soeller, G.A. Stewart, P.J. Thompson, D.C. Gruenert, M.B. Cannell, D.R. Garrod, C. Robinson, Tight junction properties of the immortalized human bronchial epithelial cell lines Calu-3 anmd 16HBE14o-, Eur. Respir. J. 15 (2000) 1058–1068.

[140] B.I. Florea, M.L. Cassara, H.E. Junginger, G. Borchard, Drug transport and metabolism characteristics of the human airway epithelial cell line Calu-3, J. Control. Release. 87 (2003) 131–138.

[141] A. Osinka, M. Poprzeczko, M.M. Zielinska, H. Fabczak, E. Joachimiak, D. Wloga, Ciliary Proteins: Filling the Gaps. Recent Advances in Deciphering the Protein Composition of Motile Ciliary Complexes, Cells. 8 (2019) 730.

[142] L.G. Tilney, P.S. Connelly, G.M. Guild, Microvilli appear to represent the first step in actin bundle formation in Drosophila bristles, J. Cell Sci. 117 (2004) 3531–3538.

[143] R. Gupta, G. Radicioni, S. Abdelwahab, H. Dang, J. Carpenter, M. Chua, P.A. Mieczkowski, J.T. Sheridan, S.H. Randell, M. Kesimer, Intercellular communication between airway epithelial cells is mediated by exosome-like vesicles, Am. J. Respir. Cell Mol. Biol. 60 (2019) 209–220.

[144] D.F. Lee, M.I. Lethem, A.B. Lansley, European Journal of Pharmaceutics and Biopharmaceutics A comparison of three mucus-secreting airway cell lines (Calu-3 , SPOC1 and UNCN3T) for use as biopharmaceutical models of the nose and lung, Eur. J. Pharm. Biopharm. 167 (2021) 159–174.

[145] N. Lodes, K. Seidensticker, A. Perniss, S. Nietzer, H. Oberwinkler, T. May, T. Walles, H. Hebestreit, S. Hackenberg, M. Steinke, Investigation on ciliary functionality of different airway epithelial cell lines in three-dimensional cell culture, Tissue Eng. - Part A. 26 (2020) 432–440.

[146] S.M. Kreda, S.F. Okada, C.A. Van Heusden, W. O'Neal, S. Gabriel, L. Abdullah, C.W. Davis, R.C. Boucher, E.R. Lazarowski, Coordinated release of nucleotides and mucin from human airway epithelial Calu-3 cells, J. Physiol. 584 (2007) 245–259.

[147] C. Meindl, S. Stranzinger, N. Dzidic, S. Salar-Behzadi, S. Mohr, A. Zimmer, E. Fröhlich, Permeation of Therapeutic Drugs in Different Formulations across the Airway Epithelium In Vitro., PLoS One. 10 (2015) 1–19.

[148] X.M. Bustamante-Marin, L.E. Ostrowski, Cilia and mucociliary clearance, Cold Spring Harb Perspect Biol. 9 (2017) a028241.

[149] R.E. Frye, M. Berk, The therapeutic use of N-acetylcysteine (NAC) in medicine, 2018.

[150] P. Calverley, P. Rogliani, A. Papi, Safety of N-Acetylcysteine at High Doses in Chronic Respiratory Diseases: A Review., Drug Saf. 44 (2021) 273–290.

[151] A.M. Sadowska, N-Acetylcysteine mucolysis in the management of chronic obstructive pulmonary disease, Ther. Adv. Respir. Dis. 6 (2012) 127–135.

[152] C. Ehre, Z.L. Rushton, B. Wang, L.N. Hothem, C.B. Morrison, N.C. Fontana, M.R. Markovetz, M.F. Delion, T. Kato, D. Villalon, W.R. Thelin, C.R. Esther, D.B. Hill, B.R. Grubb, A. Livraghi-Butrico, S.H. Donaldson, R.C. Boucher, An improved inhaled mucolytic to treat airway muco-obstructive diseases, Am. J. Respir. Crit. Care Med. 199 (2019) 171–180.

[153] N. Lababidi, E. Ofosu Kissi, W.A.M. Elgaher, V. Sigal, J. Haupenthal, B.C. Schwarz, A.K.H. Hirsch, T. Rades, M. Schneider, Spray-drying of inhalable, multifunctional formulations for the treatment of biofilms formed in cystic fibrosis, J. Control. Release. 314 (2019) 62–71.

[154] K. Peng, Y. Gao, P. Angsantikul, A. LaBarbiera, M. Goetz, A.M. Curreri, D. Rodrigues, E.E.L. Tanner, S. Mitragotri, Modulation of Gastrointestinal Mucus Properties with Ionic Liquids for Drug Delivery, Adv. Healthc. Mater. 10 (2021) e2002192.

[155] C.B. Morrison, M.R. Markovetz, C. Ehre, Mucus, mucins, and cystic fibrosis, Pediatr. Pulmonol. 54 (2019) S84–S96.

[156] J. Fiegel, C. Ehrhardt, U.F. Schaefer, C. Lehr, J. Hanes, Large Porous Particle Impingement on Lung Epithelial Cell Monolayers — Toward Improved Particle Characterization in the Lung, Pharm. Res. 20 (2003) 788–796.

[157] J.S. Patton, Mechanisms of macromolecule absorption by the lungs, Adv. Drug Deliv. Rev. 19 (1996) 3–36.

[158] J.J. Wine, The genesis of cystic fibrosis lung disease., J. Clin. Invest. 103 (1999) 309–312.

[159] T. Wang, L. Wang, X. Li, X. Hu, Y. Han, Y. Luo, Z. Wang, Q. Li, A. Aldalbahi, L. Wang, S. Song, C. Fan, Y. Zhao, M. Wang, N. Chen, Size-Dependent Regulation of Intracellular Trafficking of Polystyrene Nanoparticle-Based Drug-Delivery Systems, ACS Appl. Mater. Interfaces. 9 (2017) 18619–18625.

[160] A.P. Walczak, E. Kramer, P.J.M. Hendriksen, P. Tromp, J.P.F.G. Helsper, M. van der Zande, I.M.C.M. Rietjens, H. Bouwmeester, Translocation of differently sized and charged polystyrene nanoparticles in in vitro intestinal cell models of increasing complexity, Nanotoxicology. 9 (2015) 453–461.

[161] K. Kik, B. Bukowska, P. Sicińska, Polystyrene nanoparticles: Sources, occurrence in the environment, distribution in tissues, accumulation and toxicity to various organisms,

Environ. Pollut. 262 (2020) 114297.

[162] S. Dekali, C. Gamez, T. Kortulewski, K. Blazy, P. Rat, G. Lacroix, Assessment of an in vitro model of pulmonary barrier to study the translocation of nanoparticles, Toxicol. Reports. 1 (2014) 157–171.

[163] J. López-García, M. Lehocký, P. Humpolíček, P. Sáha, HaCaT Keratinocytes Response on Antimicrobial Atelocollagen Substrates: Extent of Cytotoxicity, Cell Viability and Proliferation, J. Funct. Biomater. 5 (2014) 43–57.

[164] X. Li, B. Kang, Y. Eom, J. Zhong, H.K. Lee, H.M. Kim, J.S. Song, Comparison of cytotoxicity effects induced by four different types of nanoparticles in human corneal and conjunctival epithelial cells., Sci. Rep. 12 (2022) 155.

[165] J. Dausend, A. Musyanovych, M. Dass, P. Walther, Schrezenmeier, K. H., Landfester, V. and Mailänder, Uptake Mechanism of Oppositely Charged Fluorescent Nanoparticles in HeLa Cells., Macromol. Biosci. 8 (2008) 1135–1143.

[166] W. Najahi-Missaoui, R.D. Arnold, B.S. Cummings, Safe nanoparticles: Are we there yet?, Int. J. Mol. Sci. 22 (2021) 385.

[167] E. Fröhlich, The role of surface charge in cellular uptake and cytotoxicity of medical nanoparticles, Int. J. Nanomedicine. 7 (2012) 5577–5591.

[168] G. Aldini, A. Altomare, G. Baron, G. Vistoli, M. Carini, L. Borsani, F. Sergio, N-Acetylcysteine as an antioxidant and disulphide breaking agent: the reasons why, Free Radic. Res. 52 (2018) 751–762.

[169] E. Cells, Y. Fu, M. Fan, L. Xu, H. Wang, Q. Hu, Y. Jin, Amino-Functionalized Polystyrene Nano-Plastics Induce Mitochondria Damage in Human Umbilical Vein Endothelial Cells, Toxics. 5 (2022) 215.

[170] S. Takatsuka, T. Morita, A. Koguchi, Y. Horikiri, H. Yamahara, H. Yoshino, Synergistic absorption enhancement of salmon calcitonin and reversible mucosal injury by applying a mucolytic agent and a non-ionic surfactant, Int. J. Pharm. 316 (2006) 124–130.

IV. Curriculum vitae

V. Scientific output

Publications

E. Meziu, A. Kraegeloh, M. Schneider.; *Mukus und Mukusmodelle: eine Übersicht. Pharmakon, Volume 10, Number 1, January 2022, pp. 53-58(6)*

E. Meziu, M. Koch, J. Fleddermann, K. Schwarzkopf, M. Schneider, A. Kraegeloh.; *Visualization of the structure of native human pulmonary mucus*. *Int. J. Pharm. 597 (2021) 120238.*

E. Meziu, K. Shehu, M. Koch, M. Schneider, A. Kraegeloh.; *Impact of mucus modulation by N-acetylcysteine on nanoparticle toxicity*. *Int. J. Pharm: X 6 (2023) 100212.*

Poster presentations

Visualization of mucus under native conditions
E. Meziu, J. Fleddermann, A. Kraegeloh, M. Schneider.;
DPhG Annual Meeting 2017. Saarbrücken, Germany. 2017.

Investigation of human pulmonary mucus using high resolution microscopy
E. Meziu, J. Fleddermann, A. Kraegeloh, M. Schneider.;
Nanosafety 2017. Saarbrücken, Germany. 2017.

A microscopy study of human tracheal mucus
E. Meziu, M. Koch, J. Fleddermann, K. Schwarzkopf, M. Schneider, A. Kraegeloh.;
Biobarriers 2018. Saarbrücken, Germany. 2018.

Microscopy Analysis of Human Mucus
E. Meziu, M. Koch, J. Fleddermann, K. Schwarzkopf, A. Kraegeloh. M. Schneider.;
Doktorandentag 2018. Saarbrücken, Germany. 2018.

Stimulated emission depletion microscopy reveals structural details of fresh human respiratory mucus
E. Meziu, M. Koch, J. Fleddermann, M. Schneider, A. Kraegeloh.;

International Symposium of the Collaborative Research Center SFB 765. Berlin, Germany. 2019

In vitro mucus for probing mucus nanoparticle interactions

E. Meziu, K. Shehu, M. Schneider, A. Kraegeloh.;

Nanosafety 2020. Online. 2020.

Barrier properties of *in vitro* mucus

E. Meziu, A. Kraegeloh, M. Schneider.;

DPhG Annual Meeting 2021. Online. 2021.

Extraction of diffusion coefficient and anomalous exponent from the MSD, log-log versus (non)linear fitting

T. John, P. Galenschowski, **E. Meziu** and C. Wagner.;

Annual European Rheology Conference 2021. Online. 2021

VI. Acknowledgments

This work would not have been possible without the support of so many people, who I would like to acknowledge at this part of my work.

Firstly, I want to express my deep gratitude to my supervisors, Prof. Dr. Marc Schneider and Priv. Doz. Dr. Annette Kraegeloh.

I want to thank Prof. Dr. Marc Schneider for giving me the opportunity to write this thesis in his group, which has been a great learning experience. Thank you, Marc, for your trust, your scientific guidance, and your support to finalize this work. I am especially grateful for your very friendly and approachable attitude as a supervisor.

I want to thank Priv. Doz. Dr. Annette Kraegeloh for granting me the chance to work at the Leibniz Institute of New Materials, which I have really enjoyed. Thank you, Annette, for your scientific guidance, for improving my scientific expertise, and for always being available to help. I truly appreciate the pleasant working atmosphere you created.

I want to thank Prof. Dr. Alexandra K. Kiemer for her contribution in the thesis supervision process and for accepting to take the role of the second examiner of my dissertation. Here I would like to attach my acknowledgements for the whole thesis committee.

Furthermore, I would like to thank Dr. Jana Fleddermann for her support regarding versatile laboratory techniques and for her scientific input in this thesis. I want to express my gratitude to Dr. Marcus Koch for the cooperation regarding the electron microscopy experiments. Dear Marcus, with your scientific guidance and your expertise, you have had an invaluable impact on this project.

Additionally, I want to thank Prof. Dr. Markus R. Meyer for making possible the cooperation regarding the metabolomic analysis of mucus. I am thankful to Dr. Sascha K. Manier and Dr. Selina Hemmer for performing the experiments. In particular, I want to thank Sascha for his scientific input, his high availability to help, and his support regarding the writing of these results.

I want to thank PD. Dr. Konrad Schwarzkopf for providing mucus samples and Simone Blaß for the realization of the mucus model illustration.

I want to thank Kristela Shehu for the great work she performed during her master thesis. Dear Kristela, I am very thankful for the good cooperation and for the friendship that developed beyond this work.

I am grateful to Silke Kiefer, Isabelle Conrad, Peter Meiers, and Marijas Jurisic for their help and kind support. I want to thank Hilal Ergül for her contribution to this work during her Erasmus internship. Additionally, I want to thank Dr. Thomas John, for his support, and for the valuable scientific discussions regarding mucus. I want to thank Dr. Salma Abdel-Hafez and Dr. Carmen Schmitz for their input and support during the process of writing. Thank you also to the DDEL and BION group of HIPS for the scientific discussions and time together during the PhD seminars.

I want to thank my colleagues from the Nano Cell Interactions from INM, and from the Schneider group, for the great time we had together. You made this challenging journey enjoyable. Thanks especially to Carmen, Isabella, Jana, Linda, Christiane, Salma, Nesma, Tamara, Nashrawan, Agnes, Tom, Johannes, Karola, Aljoscha, Marcel, Alexandra, Baseer, and Thorben.

I want to thank my parents for their continuous support and encouragement. Dear Mom, thank you also for taking care of Hanna, while I was writing. I want to thank my husband for his invaluable support, his patience, and his continuous motivation. Dear Urim, I am thankful to have you by my side. My dear daughter Hanna, I am grateful for the joy and happiness you have brought into our lives.